

INVESTIGATION OF AN UNUSUALLY SHALLOW EARTHQUAKE SEQUENCE IN MOGUL, NV FROM A DISCRIMINATION PERSPECTIVE

Ileana M. Tibuleac, et al.

**Nevada Seismological Laboratory
University of Nevada, Reno
1664 N. Virginia St., MS 174
Reno, NV 89557**

31 August 2014

Final Report

APPROVED FOR PUBLIC RELEASE; DISTRIBUTION IS UNLIMITED.



**AIR FORCE RESEARCH LABORATORY
Space Vehicles Directorate
3550 Aberdeen Ave SE
AIR FORCE MATERIEL COMMAND
KIRTLAND AIR FORCE BASE, NM 87117-5776**

DTIC COPY

NOTICE AND SIGNATURE PAGE

Using Government drawings, specifications, or other data included in this document for any purpose other than Government procurement does not in any way obligate the U.S. Government. The fact that the Government formulated or supplied the drawings, specifications, or other data does not license the holder or any other person or corporation; or convey any rights or permission to manufacture, use, or sell any patented invention that may relate to them.

This report was cleared for public release by the 377 ABW Public Affairs Office and is available to the general public, including foreign nationals. Copies may be obtained from the Defense Technical Information Center (DTIC) (<http://www.dtic.mil>).

AFRL-RV-PS-TR-2014-0185 HAS BEEN REVIEWED AND IS APPROVED FOR PUBLICATION IN ACCORDANCE WITH ASSIGNED DISTRIBUTION STATEMENT.

//SIGNED//

Robert Raistrick
Project Manager, AFRL/RVBYE

//SIGNED//

Glenn M. Vaughan, Colonel, USAF
Chief, Battlespace Environment Division

This report is published in the interest of scientific and technical information exchange, and its publication does not constitute the Government's approval or disapproval of its ideas or findings.

REPORT DOCUMENTATION PAGE				Form Approved OMB No. 0704-0188	
Public reporting burden for this collection of information is estimated to average 1 hour per response, including the time for reviewing instructions, searching existing data sources, gathering and maintaining the data needed, and completing and reviewing this collection of information. Send comments regarding this burden estimate or any other aspect of this collection of information, including suggestions for reducing this burden to Department of Defense, Washington Headquarters Services, Directorate for Information Operations and Reports (0704-0188), 1215 Jefferson Davis Highway, Suite 1204, Arlington, VA 22202-4302. Respondents should be aware that notwithstanding any other provision of law, no person shall be subject to any penalty for failing to comply with a collection of information if it does not display a currently valid OMB control number. PLEASE DO NOT RETURN YOUR FORM TO THE ABOVE ADDRESS.					
1. REPORT DATE (DD-MM-YYYY) 31-08-2014		2. REPORT TYPE Final Report		3. DATES COVERED (From - To) 01 Mar 2011 – 31 Aug 2014	
4. TITLE AND SUBTITLE Investigation of an Unusually Shallow Earthquake Sequence in Mogul, NV from a Discrimination Perspective				5a. CONTRACT NUMBER FA9453-11-1-0236	
				5b. GRANT NUMBER	
				5c. PROGRAM ELEMENT NUMBER 62601F	
6. AUTHOR(S) Ileana M. Tibuleac, David von Seggern, Glenn Biasi, and John G. Anderson				5d. PROJECT NUMBER 1010	
				5e. TASK NUMBER PPM00009387	
				5f. WORK UNIT NUMBER EF004156	
7. PERFORMING ORGANIZATION NAME(S) AND ADDRESS(ES) Nevada Seismological Laboratory University of Nevada, Reno 1664 N. Virginia St., MS 174 Reno, NV 89557				8. PERFORMING ORGANIZATION REPORT NUMBER	
9. SPONSORING / MONITORING AGENCY NAME(S) AND ADDRESS(ES) Air Force Research Laboratory Space Vehicles Directorate 3550 Aberdeen Avenue SE Kirtland AFB, NM 87117-5776				10. SPONSOR/MONITOR'S ACRONYM(S) AFRL/RVBYE	
				11. SPONSOR/MONITOR'S REPORT NUMBER(S) AFRL-RV-PS-TR-2014-0185	
12. DISTRIBUTION / AVAILABILITY STATEMENT Approved for public release; distribution is unlimited. (377ABW-2014-1022 dtd 13 Jan 2015)					
13. SUPPLEMENTARY NOTES					
14. ABSTRACT The primary objective of this study was a detailed investigation of an unusually shallow earthquake sequence that occurred in 2008 in Mogul, west of Reno, Nevada. The main shock (MS) of this sequence occurred at 2.8 km below the surface and satisfied criteria for GT1 qualification. The source properties of the Mogul earthquakes with $M_L \geq 3$ in the Mogul sequence were investigated. Moment magnitude and stress drop were estimated using: 1) A spectral method, which resulted in an estimate of the MS stress drop of 8.2 MPa (82 bars), with a corner frequency of 0.8s; 2) An Empirical Green's Function method using the whole wave train at epicentral distances < 10 km, which estimated a main shock stress drop of 17.5 MPa. The source area of the Mogul earthquake was estimated to be ~ 2 km along strike and 1.5 km along dip, with the greatest energy release in the depth range of 2.0-3.2 km, with more energy released above the hypocenter (2.7 km) than below; 3) Using Lg coda spectral ratios, estimates of the apparent stress for the MS were 1.2 MPa, for a moment of $4.07 \cdot 10^{16}$ Nm, with interquartile range (iqr) of 0.84 MPa. The MS stress drop was estimated at 5.6 MPa, with iqr of 4.1 MPa. The MS corner frequency was 0.72 s, with iqr 0.2 s. Unlike for the main shock, the local and moment magnitude values for the smaller earthquakes with $M_L > 3.0$ were within 0.2 magnitude units (m.u) when estimated from Lg coda. Investigations of the P/Sg and the P/Lg discriminant at seven local and regional stations in the western Great Basin showed that the Mogul earthquakes were discriminated from commercial and nuclear explosions even for small magnitude ($M_L < 2$) events. The best earthquake – explosion separation was observed for Pg/Lg (Pg/Sg) ratios at 6-8 Hz, and for Lg spectral ratios taken in the 1 to 2 and 6 to 8 Hz frequency bands, similar to previous observations in Nevada. Based on differences between M_s and m_b , four very shallow Mogul earthquakes and seven crustal earthquakes within 100 km of the Mogul MS epicenter, with $m_b(\text{NEIC}) > 3$ m.u. and $M_s(\text{VMAX}) > 3.1$ m.u., were screened as earthquakes, when using criteria for teleseismic and regional events. Uncharacteristic peak accelerations of the Mogul sequence were observed at stations in a small area (less than 10 km radius) around the MS epicenter, however, in this particular case, the P/S and M_s - m_b discrimination algorithms correctly classified these events as earthquakes.					
15. SUBJECT TERMS Shallow earthquake, discrimination					
16. SECURITY CLASSIFICATION OF:			17. LIMITATION OF ABSTRACT Unlimited	18. NUMBER OF PAGES 130	19a. NAME OF RESPONSIBLE PERSON Robert Raistrick
a. REPORT Unclassified	b. ABSTRACT Unclassified	c. THIS PAGE Unclassified			19b. TELEPHONE NUMBER (include area code)

This page is intentionally left blank.

Table of Contents

1. Summary	1
2. Introduction	2
3. Technical Approach.....	2
4. Results and Discussion	2
4.1. Task 1	2
4.1.1. Double-Difference Location and GT Classification of the 2008 Mogul, Nevada Very Shallow Earthquake Sequence	3
4.1.2. Seismic Velocity in the Source Area	19
4.2. Task 2	21
4.2.1. Stress Drop and Radiated Energy of the Main Shock and Principal Fore and Aftershocks	21
4.2.2. Investigation of Source Scaling of the Mogul Sequence	38
4.2.2.1. Probing the 2008 Mogul, Nevada, Earthquake Using Empirical Green's Functions	38
4.2.2.2. Measurements of Coda Envelopes to Estimate Moment Magnitude and Seismic Stress Drop	59
4.3 Task 3	77
4.3.1. Spectral Ratio Discrimination	78
4.3.2. Application of the Ms-mb Discriminant to a Set of Very Shallow Earthquakes in Western Nevada.....	101
References	112
List of Symbols, Abbreviations, and Acronyms	118

List of Figures

1	Stations used in locating the Mogul earthquakes sequence.	11
2	Mogul sequence location results shown in map view.	12
3	Mogul sequence location results shown in a cross-section along azimuth 53° east of north.	13
4	Hypocenter shift histograms for the NSL catalog hypocenters relative to the HYPODD ones (case “cc” for HYPODD in Figure 2).	14
5	Mean shift for the NSL catalog epicenters relative to the HYPODD ones (case “cc” for HYPODD in Figure 2).	15
6	Map of the Mogul main-shock epicenters estimated using velocity models shown in Table 1.	16
7	P arrivals at the four closest stations to the main shock epicenter.	17
8	Tests for the best hypocenter with respect to the P-wave arrival times at the closest four stations (HONJ, MOGE, MOGL, MOGW).	18
9	Maximum recorded peak vector acceleration versus the oblique distance from the preferred HYPODD hypocenter for the Mogul main shock.	19
10	P- and S-wave travel times versus distance and depth.	20
11	a) Kappa AH view showing the Mogul main shock east component accelerometer record at station HONJ b) North component accelerogram from station MOGL for the main shock.	27 28
12	Shear-wave spectra for station MOGL, HNE channel for good signal-to-noise cases.	29
13	Residual spectra relative to Brune model.....	30
14	Station RFNV north channel residuals to a Brune-k model source spectrum.	30
15	Example spectral residuals for ten stations near the Mogul swarm.	31
16	Map of stations and larger events of the Mogul sequence.	32
17	Particle motions for three near-field stations recording the Mogul main shock.	33
18	After adjusting soil sites downward by a constant factor of 2.35, M_w event average and rock M_w estimates agree well.	34
19	Corner frequency estimates are plotted for averaged soil and rock component averages.	35
20	Brune stress drop (MPa) for rock site horizontal components (blue) are plotted versus M_w developed from all strong-motion stations.	36
21	Final estimates for stress drop versus M_w for the Mogul M3+ event set.	36
22	Cross sections of Mogul, Nevada source area.	51
23	Location of EGFs for initial inversion for the fault dislocation model.	52

24	Quality of fit of the strong motion records at station HONJ, as a function of the number of eigenvalues kept from the singular-value decomposition of the matrix G	53
25	Comparison of source functions for two EGFs, EGF 7 and EGF 21, in the 10 EGF inversion sequence.	54
26	Match between observed seismograms and the attempt to recreate them using the sum of empirical Green's functions.	55
27	Slip time functions for the three EGFs that contribute most strongly to reproduce the Mogul earthquake seismograms.....	58
28	Moment rate for the seven EGFs used to reproduce the seismograms in Figure 25.	59
29	Permanent and temporary stations recording the Mogul sequence.	63
30	Stations (green triangles) used in this study.	64
31	Earthquake No 3 (Table 6) waveforms and coda envelopes at station M11A.	65
32	Synthetic envelopes (red) were fit to the observed main shock coda envelopes (blue), and Lg coda amplitudes were estimated for each event in each frequency band.....	66
33	Maps of the coda shape parameter GAMMA estimated at each station for each center frequency.	66
34	Maps of the interquartile range (a measure of statistical dispersion, being equal to the difference between the 75th upper and 25th lower quartiles) of the coda shape parameter GAMMA estimated at each station for each center frequency..	67
35	Maps of the coda shape parameter BETA estimated at each station for each center frequency.	67
36	Maps of the interquartile range (a measure of statistical dispersion, being equal to the difference between the upper and lower quartiles) of the coda shape parameter BETA, estimated at each station for each center frequency.	68
37	The spectral ratio fits for the events in Table 6, in the case with MS 0.72 Hz and small earthquake frequencies are unconstrained.	69
38	The sum of the absolute errors of the fits in Figure 37 as a function of percentage variance of the corner frequency from the values in Table 8.	70
39	The ten-base logarithm of the apparent stress (MPa) as a function of ten-base of the seismic moment in Table 6..	71
40	The ten-base logarithm of the stress drop (MPa) as a function of the ten-base logarithm of the seismic moment in Table 6.	72
41	Corner frequency as a function of the seismic moment for the Mogul sequence (yellow dot, the MS and black dots, the smaller earthquakes) superposed on Figure 3 in the study by Yoo and Mayeda, 2013.	73
42	M_L as a function of M_w for events used in this study.	74

43	Example of bandpass-filtered seismograms, with a Butterworth, zero-phase, eight pole filter, from four events used in this study.	84
44	Locations of events recorded at Basin and Range seismic stations.	85
45	$\log_{10} P_g/S_g$ and S spectral ratios for events recorded at Basin and Range seismic stations at distances less than 200 km, as a function of $\log_{10}(A_{Pg})$	86
46	Base-ten logarithm of P_g/L_g ratios for events recorded at Basin and Range seismic stations at distances greater than 100 km.	90
47	$M_L - \log_{10}(A_{Pg})$ as a function of a $\log_{10}(\Delta) + b$ at each station.....	93
48	A comparison of the base-ten logarithm of the P/L_g ratios for events recorded at ELK, as a function of $\log_{10}(A_{Pg})$ and m_{Pg}	94
49	Comparison of the base-ten logarithm of the spectral ratios estimated in the case when the attenuation coefficient Q was variable (inset a) for the propagation region and the same Q was applied (inset b)..	95
50	A: Displacement (nm) waveforms of the 2005/09/16, 15:09:42 earthquake, ML 4.2 (black) filtered between 7 s and 25 s, with a Butterworth, 6 pole, zero phase filter recorded at three stations: CMB (epicentral distance 130 km, azimuth 213 deg), WVOR (epicentral distance 386 km, azimuth 11.58 deg) and BMO (epicentral distance 674 km, azimuth 15 deg). Superposed are the (red) waveforms obtained after applying PMF on the raw data, which have been used for $M_s(VMAX)$ estimation. B. Same as Inset A for an earthquake that occurred on 2011/11/27 06:33:02, of magnitude ML 4.1 (IDC); C. Same as Inset A for an earthquake on 2008/10/27, 11:33:20, ML 4.2.	107
51	Examples of Butterworth-filtered seismograms for four earthquakes recorded at WVOR (Table 1).	108
52	Discrimination results for maximum-likelihood m_b (IDC) and ISC-estimated M_s using the decision line estimated by Selby et al., (2012).	109
53	Discrimination results for m_b and $M_s(VMAX)$ using the decision line estimated by Bonner et al., (2006).	110
54	Examples of $M_s(VMAX)$ estimation for the earthquakes in Figure 50 and for the Mogul Main shock.	111

List of Tables

1	Main shock depth from available sources.	9
2	Seismic velocity model parameters.	10
3	Source parameters for the Mogul sequence: moment magnitude (M_w), local magnitude (M_L), corner frequency (f_c) and stress drop developed using only the log-averaged rock component averages.	37
4	Model of the Mogul mainshock used in this study.	49
5	Seismic stations used in this study. More information on these stations is available in Anderson et al. (2009)	50
6	Focal mechanism and moment tensor of the largest ($M_L > 3.0$) Mogul earthquakes. The relation between seismic moment, M_0 and moment magnitude M_w is $\log M_0 = 1.5 M_w + 16.05$, where the seismic moment is in units of dyne-cm. Gray colors are used to mark sources of moment tensor solutions. M_w UNR was estimated by Biasi et al, 2012.	75
7	Used frequency bands and median coda window for each band. “*” refers to frequency bands only available at stations within 20 km from the main shock.	76
8	Earthquake parameters for the smaller earthquakes in the Mogul sequence. f_c is the corner frequency.	77
9	List of earthquakes, and commercial and nuclear explosions used in this study.	96
10	Regression parameters of m_{pg} and M_L (UNR). The table shows parameters in the equation $M_L - \log_{10}(A_{pg}) = a \log_{10}(\Delta) + b$, the station correction as the median of the difference $M_L - m_{pg}$, where $m_{pg} = \log_{10}(A_{pg}) + a \log_{10}(\Delta) + b$ and the value of the correlation coefficient of M_L and m_{pg}	100
11	Earthquakes used in this section. Highlighted rows are Mogul earthquakes.	105
12	The magnitude values used in Figures 52 and 53.	106

This page is intentionally left blank.

1. SUMMARY

We report on investigations of the effectiveness of discrimination algorithms when applied to an unusually shallow (1-4 km deep) earthquake sequence in Mogul, west of Reno, NV. Double-difference event relocations confirmed that the $M_L \geq 3$ events of the Mogul sequence were shallower than five km, with the main shock (MS) at ~ 2.8 km below the surface. This sequence satisfies criteria for GT1 qualification.

Stress drop was estimated using three methods:

1) A spectral method, which estimated the main shock stress drop 8 MPa and a corner frequency of 0.8s. Stress drop and moment did not correlate with hypocentral depth. The moment magnitude of the relocated main shock, after corrections for source zone shear wave velocity and depth, had similar values with regional estimates which used 20 s and longer period surface waves. When using this method, soil site event-averaged seismic moments were a factor of 2.35 greater than the rock sites. After correction, event averaged magnitudes were developed. Basin-induced surface waves may contribute to low frequency energy that affect spectral fitting;

2) Using full-waveform Empirical Green's Functions, a complex space-time distribution of slip on the source was revealed, including interacting patches of slip at different locations, and repeated rupture of one part of the fault near the hypocenter. The entire duration of slip on the fault was about 0.9 s. The empirical Green's functions that contributed nearly all of the seismic moment were within 0.6 km of the main shock hypocenter. The full fault dimension was under 2 km in length and 1.5 km in depth, which was only a part of the fault area that was active in the foreshock sequence. For this source dimension, a stress drop of 17.5 MPa was estimated, which is about 25% of the expected lithostatic stress at the hypocentral depth.

3) Using Lg coda ratios, estimates of the apparent stress for the MS were 1.2 MPa, for a moment of 4.07×10^{16} Nm, with a interquartile range (*iqr*) of 0.84 MPa. The stress drop in MPa was estimated for the main shock at 5.6 MPa, with an *iqr* of 4.1 MPa. The stress drop values are consistent with the direct phase spectral analysis and with stress drops estimated using the same methods in northern Nevada by other authors, however, are smaller than the values estimated using EGF analysis. The MS corner frequency was 0.72 s, with an *iqr* 0.2 s. Unlike for the main shock, the local and moment magnitude values for the smaller earthquakes with $M_L > 3.0$ were within 0.2 m.u..

Investigations of the P/Sg and the P/Lg discriminant at seven local and regional stations in the western Great Basin showed that the Mogul earthquakes were discriminated from commercial and nuclear explosions even for small magnitude ($M_L < 2$) events. The best earthquake – explosion separation was observed for Pg/Lg (Pg/Sg) ratios at 6-8 Hz, and for Lg spectral ratios taken in the 1 to 2 and 6 to 8 Hz frequency bands, similar to previous observations in Nevada.

Based on differences between M_s and m_b , four very shallow Mogul earthquakes and seven crustal earthquakes within 100 km of the Mogul MS epicenter, with $m_b(\text{NEIC}) > 3$ m.u. and $M_s(\text{VMAX}) > 3.1$ m.u., were screened as earthquakes, when using criteria for teleseismic and regional events.

Uncharacteristic attenuation and peak accelerations of the Mogul sequence were observed at stations in a small area (less than 10 km radius) around the MS epicenter, however, in this particular case, the P/S and Ms-mb discrimination algorithms correctly classified these events as earthquakes.

2. INTRODUCTION

The primary objective of this study is a detailed investigation of an unusually shallow earthquake sequence that occurred in 2008 in Mogul, west of Reno, Nevada. This sequence consisted of over 1938 earthquakes with M_L 1.0 or greater, 909 earthquakes with $M_L \geq 1.5$; 295 earthquakes with $M_L \geq 2.0$; 83 earthquakes with $M_L \geq 2.5$; 38 earthquakes with $M_L \geq 3.0$ and four events with $M_L \geq 4.0$. These earthquakes were concentrated in depth between 1 and 4 km and ranging in magnitude up to M_w 5.0 (the “main shock” named MS). Preliminary analyses of the main shock have revealed uncharacteristically high amplitude near-field ground motions and uncharacteristically rapid attenuation with distance, which could affect magnitude estimates and discrimination metrics. For our investigations we use a unique broadband and strong-motion recording database, with four stations within two km from the epicenter of the main shock.

3. TECHNICAL APPROACH

We have organized our study in four tasks, as follows:

Task 1.

Build a database, including well-located earthquakes and explosions and acquire all available public domain information on very shallow event discrimination analysis. The database will be used, as appropriate unless similar studies have already been performed, in Tasks 2, 3 and 4.

Task 2.

1. Analyze the stress drop and radiated energy of the main shock and principal fore- and aftershocks;
2. Investigate the source scaling of the Mogul sequence.

Task 3.

Investigate the effect of source depth on P and S spectra and spectral ratios, signal complexity, and m_b - M_s discrimination;

Task 4.

Attempt to understand the origin and nature of the exceptional near-source attenuation and its effect on magnitude estimates and energy content-related discriminant performance.

4. RESULTS AND DISCUSSION

4.1 Task 1. Within Task 1, a database was built and we performed earthquake relocation, local magnitude M_L estimation, and the best velocity model in and around the source area was estimated. In

summary, the estimated GT accuracy for the main shock is GT1, with a depth of approximately 2.8 km below the surface. All depth estimates were referenced to the mean elevation of the seismic stations used, which was 1.6 km above sea-level. In the source area shear-wave velocity was estimated as 2.87 km/s and the P-wave velocity was 5.13 km/s. These results are discussed in detail below.

A well-located shallow earthquake and explosion database has been built, also including available public domain information on very shallow event discrimination analysis. The database includes: 1) The Mogul earthquakes sequence, with a total of 1938 events. Of these events, only 26 earthquakes ($M_L > 1.0$), of which five with $M_L > 1.5$, are located from 5 to 6 km depth. Regional and teleseismic records of the largest Mogul events from Incorporated Research Institutions for Seismology (IRIS) and the Air Force Research Laboratory are in the database. A sorted mining explosion database (more than 50 events with $M_L > 1.5$) in the Reno-Carson City, NV, area is available. The explosions occurred within 100 km of the Mogul main shock. Records of nuclear explosion waveforms at LLNL stations are in the database. The waveforms from events belonging to the 1993 Rock Valley sequence (depth < 3 km) and the available IRIS and NN data (including Southern Great Basin Seismic Network records), for the largest event M_w 3.7 (m_b 4.3) in this sequence are also added to the database. High quality waveforms from crustal earthquakes ($M_L \geq 2.4$) that occurred in the project area, recorded at the Nevada Seismic Network and at IRIS stations from 1984 to 2011, an earthquake sequence that occurred south of Reno (main shock M_L 3.0, 12 km deep, on 11/28/2010, 09:47:38) and events (depth 2-17 km) from the 2011 Hawthorne earthquake sequence (main shock M_L 4.6, 15 km depth, on 04/16/2011, 17:45:37) are also archived. Sorted records of the Crandall Canyon mine collapse (0.6 km depth, M_L 3.9) and of USGS-located events ($M_L > 2.5$) within 100 km of the mine are available for further analysis. A collection of crustal earthquakes ($M_L > 2.5$), composed of events that occurred within 20 km of regional stations in Nevada, which can provide reversed path information is sorted and prepared for analysis.

4.1.1. Double-Difference Location and GT Classification of the 2008 Mogul, Nevada Very Shallow Earthquake Sequence

INTRODUCTION

A long sequence of earthquakes occurred west of Reno, Nevada under a community called Mogul during 2008 (Anderson et al., 2009; Tibuleac et al., 2011). This sequence began with a swarm-like series in early 2008 and was punctuated by an M_w 5.0 earthquake on April 26, 2008. (06:40:10 UTC and 10:40:10 PM April 25 local time). The main shock was followed by a fairly typical aftershock sequence through the remainder of 2008. The sequence consisted of over 2000 earthquakes with $M_L \geq 1.0$, concentrated in depths between 1 and 4 km and ranging in magnitude up to M_w 5.0 (main shock). The swarm-like activity prior to the main shock provided time to instrument the epicentral area with temporary broadband and strong-motion stations, in advance of the largest events. These stations complemented the Nevada and California permanent seismic monitoring stations and the high-quality broadband stations of the Earthscope Transportable Array network deployed in Nevada during 2008.

The primary objective of this study was a detailed investigation of this sequence of earthquakes in terms of location and ground truth (GT) classification. Compared to earthquakes at typical depths, these shallow earthquakes have uncharacteristically high-amplitude, near-field ground motions and uncharacteristically rapid attenuation with distance from the main shock (Anderson et al., 2009). For our investigations, we used a unique broadband and strong-motion recording database, from stations as close as 1 km from the epicenter of the main shock and most of the smaller events. These sensors

recorded waveforms that we have organized into a database including near-field and seismic-network recordings of all the $ML \geq 1.0$ earthquakes of the sequence located by the Nevada Seismological Laboratory (NSL). We have relocated the Mogul earthquakes with HYPODD, incorporating P and S cross-correlations. Location shifts as large as several hundred meters were observed when compared to the original catalog hypocenters. The main shock has been relocated at 2.8 km below the surface using HYPODD. 94% of the sequence was relocated above 4 km depth, relative to the surface, with HYPODD. Only a few other sequences occurring above the 5 km deep upper limit of the “seismogenic zone” have been observed in the western United States: in California (Fletcher et al., 1987; Frankel et al., 1986, Prejean and Ellsworth, 2001) and in Nevada. Adequate source parameter analysis was possible when the earthquake hypocenter location and the velocity model in the source area were well resolved. Efforts have been made to estimate the best velocity model in the area.

Ground truth (GT) events have errors on location, depth, and origin time controlled by exactly known locations as with chemical and nuclear explosions, with mine collapses, with rockfalls, and with many other phenomena. Only a limited number of events satisfy these requirements and few are large enough to be recorded at regional distances or teleseismic distances. We use the “GTn” classification of Bondar et al. (2001) which indicates that the true epicenter lies within “n” km of the estimated epicenter at a high confidence level. GT0 or GT1 events are usually nuclear explosions (Bondar et al., 2004). The ground-truth classification of the Mogul main shock was made with the help of results from independent InSAR and geodetic analyses, with error analysis of the HYPODD results, and with fitting ground-motion amplitudes of near stations. As discussed by Bondar and McLaughlin (2009), the concept of ground-truth (GT) events was important for event discrimination. The absolute accuracy of the event locations is always in doubt and cannot be simply inferred from the error ellipsoid (Evernden, 1969). Ground truth is usually provided by means independent of seismic observations, such as satellite imagery, InSAR or GPS modeling, known mining blast locations, surface rupture lineations, and other uncommon means.

DATA

The database for the Mogul sequence of earthquakes was assembled from recordings at temporary and permanent stations. Figure 1 shows the set of stations closest to the Mogul sequence; more distant stations control the locations less and are not shown here. In all, arrivals from 153 stations were used for the location of the events in the sequence. These stations comprise narrow-band analog sites, broadband digital sites, and accelerometer sites. The database includes 2013 earthquakes with $ML \geq 1.0$, most with near-field recordings. Regional and teleseismic recordings of the largest Mogul events were collected from the Incorporated Research Institutions for Seismology (IRIS) and the Air Force Research Laboratory (AFRL). The database was assembled in a CSS3.0 set of tables. Both original and relocated hypocenters were retained, and the original NSL magnitude was kept for the relocated hypocenters. Although the hypocenters often changed hundreds of meters from the original to relocated coordinates, we believe that a recomputation of magnitude based on the relocated coordinates would provide no significant gain in accuracy.

METHOD

Relocation of Hypocenters

The early events in this sequence were located at abnormally shallow depths by the routine NSL analysis. The depth of the main shock event from various available sources, including NSL, is shown in Table 1. Accurate estimation of the depth of the main shock and the rest of the events in the sequence is important in itself, but especially necessary for derivative studies such as source mechanism, slip characterization, stress drop, and geological relations. It is well known that following routine hypocenter location with various relocation methods will improve both the absolute and the relative locations of events in a sequence (Menke and Schaff, 2004). For event relocation we used HYPODD (Waldhauser and Ellsworth, 2000) in an effort to reduce the errors of hypocenter estimation for the main shock and for all the events of the Mogul sequence. No catalog arrival-time picks were changed in the relocation work. We performed extensive time-domain cross-correlations on P and S waves to improve the relocations using a computer code that directly accesses the CSS3.0 database. Cross-correlations results that showed less than a 0.7 normalized cross-correlation coefficient were discarded. Both negative and positive correlations above this threshold were accepted because our previous work shows that polarity is occasionally flipped between events due to rotation of the focal mechanism. A total of 233,357 cross-correlation times were retained. A catalog-arrival phase file was created from the CSS3.0 tables, and the HYPODD pre-processing program PH2DT was used to create the file of differential catalog times. Both P and S phases were used. A total of 457,572 differential times were formed.

The number of parameters available to change in HYPODD runs is large, and the results changed depending on parameter values. It was determined quickly that the entire sequence should simply be relocated as a single cluster rather than breaking it into several clusters. Parameters were initially set according to experience with previous datasets in HYPODD and then adjusted somewhat for the Mogul sequence.

Adequate source parameter analysis is possible when the earthquake hypocenter locations and the velocity model in the source area are well resolved. The seismic velocity model in the hypocentral area is an important variable affecting the seismic moment and the earthquake mechanism as well as affecting the event locations themselves. Thus we sought an improved seismic velocity model to use for event relocation. Table 2 shows the velocity models tried in this investigation. The "pickema2" Earth model is the standard location model for the NSL seismic catalog, with comparably high velocity near the surface, 5.85 km/s. We sought a model which would represent the shallow structure better. Two other models were used, one (named KS) developed from western Nevada location work (Ken Smith, personal communication) and a model developed by Tibuleac (named IT, using ambient seismic noise to estimate shallow shear velocity). The P/S velocity ratio was set to 1.73 (Poisson solid) in all location work reported here. We caution that improved one-dimensional models cannot remove bias due to model error. Such bias is particularly acute if the deviations of the model from the actual structure trend in one general direction. Note that the Mogul area of Figure 1 is at the Sierra Nevada front where a definite change in velocities is expected.

Ground-Truth Classification

No surface rupture was observed for the Mogul main shock, but InSAR and GPS (discussed below) are able to be applied to constrain the fault plane. We also use the decay of acceleration amplitudes from very close stations to constrain the true hypocenter. In the case of the Mogul main shock, the ground-truth constraints themselves cannot be established to an accuracy of near zero, and some uncertainty remains.

RESULTS

Relocation of Hypocenters

All the models in Table 2 were tried in HYPODD, but the KS model was preferred because the mean error of hypocentral parameters was lower than when using other seismic models and resulted in the fewest events being discarded in the HYPODD run (75 of the original 2013). The results using the IT and KS models are very similar, and either is preferable to the “pickema2” model results. Figure 2 shows 4 sets of location results. The first (“cat” in upper left) is the original NSL catalog epicenters, using the “pickema2” model of Table 2. The second (“ct” -- upper right) is the HYPODD result using only double-difference catalog times. The third (“cc” -- lower right) is when cross-correlation data are added to the input catalog data and the final iteration heavily weights these cross-correlation data. The last (“equal” - lower left) shows the HYPODD epicenters when the “ct” and “cc” data are equally weighted in the final iteration. We prefer the “cc” results in which 1,938 of the 2,013 original catalog events were relocated, amounting to roughly 97% of the original events. These lost events were mostly concentrated in the day of 5/2/2008. Possible causes could be a timing error or a systematic violation of location protocol by one or more analysts on this day. We have not tried to correct this problem as the loss of this small fraction of events will have minimal effect on results obtained from the relocated event set.

The fault plane is fairly clearly delineated by HYPODD results and trends at approximately 143° east of north. There is a strong indication of a separate slip area to the northeast of the main fault. The cluster indicating this developed after the main shock. We point out now that the new HYPODD epicenter locations were all approximately one km east of the original catalog location, and we will discuss this later in relation to GT.

Results for computed event depths are shown in cross-sectional form in Figure 3, with the same arrangement of plots as in Figure 2. All depth estimates are referenced to the mean elevation of the seismic stations used, which is approximately 1.6 km above sea-level. The cross-section is aligned left-to-right from southwest to northeast along the azimuth of 53° east of north. Hypocenters were projected perpendicularly to this cross-section. The HYPODD results definitely improve the location of the main fault plane and also constrict the range of depth over which the sequence occurred. The cluster to the northeast of the main fault, as seen in the epicenter plots of Figure 2 is clearly shown in the Figure 3 cross-sections, but there is not sufficient clarity to determine if these events occurred on a parallel or conjugate fault.

Figure 4 shows the coordinate changes between the original catalog hypocenters and the relocated hypocenters. There was an eastward shift of HYPODD coordinates, but not a clear north or south shift. The depth shift is difficult to interpret because a large number of the NSL catalog locations were at anomalously shallow depths of 0-1 km, with many having been constrained to the surface. HYPODD both generally pushed these downwards and also generally pulled up the deeper catalog locations, as

shown in Figure 3. The depth of the main shock of the Mogul sequence is an important parameter which was best estimated using the "KS" or "IT" model, which have reasonable upper crustal layers, with P velocities in the upper layer in the 3.0-3.5 km/s range, gradually increasing to 6.0 km/s at 4-6 km depth.

The main shock was relocated at a considerable lateral distance from the NSL catalog location (nearly 1 km), as shown in Figure 2. This change in location was significantly more than the typical changes for the other events in the sequence. We suspected that this result may have some connection to the greater amount of data used for the main-shock location relative to that for others. There is, in fact, a fairly well-defined magnitude-dependent trend in the shift of the epicenters between catalog and HYPODD results as seen in Figure 5. Here, we binned the location changes for dx (east-west) and dy (north-south) by steps of 0.5 in ML between 1 and 5. The fact that the dx changes are clearly dependent on magnitude points to errors in the assumed model which trend east-west, in accordance with known geology. Such errors accumulate for more distant reporting stations, and the larger events have a greater proportion of distant stations. We investigate the accuracy of the main-shock location further in our presentation of GT results.

GT Classification

Key to the depth control were the closest four stations to the main shock: MOGE, MOGL, MOGW, and HONJ (Figure 6). No data was available at MOGC. It is important to note that the four nearest stations were very close to the mean datum of 1.6 km stated above (MOGE = 1.45 km, MOGL = 1.47 km, MOGW = 1.58 km, and HONJ = 1.56 km). The HYPODD epicenters with 3 different velocity models were all approximately one km east of the original catalog location. The superior accuracy of these epicenters compared to that of the NSL catalog can be justified by an examination of the actual traces recorded at the four closest stations, as shown in Figure 7. Arrival times from these four stations imposed strong constraints on the true location. These picks and the station locations cannot allow an epicenter as far to the west as that in the NSL catalog.

Note that the P phase arrived first at station MOGE. Next, the P phase arrived nearly simultaneously at MOGL, MOGW, and HONJ. The P travel times were 0.6-0.7 s, thus indicating a very shallow depth. The S-waves were difficult to pick due to their emergent nature, and reliable S-P times could not be estimated. However, they were likely in the range of 0.7 to 0.9 seconds.

A grid search was conducted over a volume for the hypocenter and origin time which resulted in the lowest rms residual for the P observations. This volume extended 3 km laterally in each direction from the HYPODD KS epicenter (with an increment of 0.5 km), and 1 km vertically up and down from the HYPODD KS hypocenter (with an increment of 1.0 km). As the hypocenter was moved through each grid point in the volume, the origin time was varied to produce the best fit of predicted times to the four P-wave arrival times. The prediction was made using a simple homogeneous P-velocity model of 4.6 km/s. This velocity was estimated by repeating the entire modeling computation for a range of velocities and looking for the best fit to the arrival times. The area surrounding the main-shock location was mostly granite, and 4.6 km/s was low for, but not outside of, the range of granite observations. Figure 8 shows the results for three assumed depths, with the HYPODD depth of 2.76 km being the middle plot. These plots are contours of the gridded results, showing how the rms varied as the epicenter is moved to each of the three depths. Note that the minimum was not at the (0,0) location which is the HYPODD KS result

and that the minimum region was smeared in a northeast-striking direction. These grid results confirm the HYPODD results which push the epicenter eastward from the NSL catalog one. On the basis of the inter-event precision of HYPODD calculations, we estimated that all the relocated Mogul earthquakes were GT1 or less. The hypocenter depth was less certain. However, every location result (Table 1), including the moment-tensor inversion results, were important corroborating evidence of an anomalously shallow depth for the main shock. Regardless, depth accuracy was not considered in assigning the GT1 classification.

DISCUSSION AND CONCLUSIONS

The depth of the main shock of the Mogul sequence is an important parameter, with implication for nuclear monitoring and for hazard assessment. Our preferred depth is 2.76 km below the surface for the main-shock hypocenter. All the HYPODD results indicated that the Mogul main shock was indeed anomalously shallow for an Mw 5.0 earthquake. This depth was similar to that of the hundreds of smaller earthquakes in the Mogul sequence. The fault-slip model of Anderson et al. (in press) shows that the fault plane is confined to a vertical distance of less than 1 km from the hypocenter; thus the hypocenter depth can be no greater than 3.8 km.

The fine precision of the hypocenters from HYPODD, however, applies to relative positioning only. The absolute accuracy is affected by the seismic velocity model. However, using three different models, one of which (pickema2) is greatly different than the other two for shallow depths, affects the hypocenter parameters by only one to two hundred meters (Figure 6). Given the control of the main shock by the four closest stations, we believe no reasonable model change could move the hypocenter by more than 1 km, probably much less, in any of the three spatial dimensions. Thus, an estimate of GT accuracy for the main shock is GT1, with a depth of approximately 2.8 km below the surface. The GT1 status of all the rest of the sequence follows if that of the main shock is accepted. Smaller events are well recorded and have reading errors no larger than for the main shock. Further, the HYPODD algorithm strongly culls poorly timed arrivals.

An independent seismic assessment of the accuracy of the HYPODD hypocenter for the main shock is weakly provided by the measured acceleration data, taken from Supplemental Table S2A of Anderson et al. (2009). Using the distance r from the hypocenter (oblique distance) and the vector acceleration maximum, the data for stations within 10 km was shown in Figure 9. A decay relation of acceleration = kr^{-2} , where r is the oblique distance to the hypocenter, has been fit in the log-log domain to the data to determine the constant k , and this function is plotted. Moving the hypocenter much more than a kilometer horizontally would lead to a much less acceptable fit, and it could not support the original catalog location shown in Figure 6.

More independent checks of the HYPODD location result come from the GPS work of Blewitt et al. (2008) and the InSAR work of Bell et al. (2012). Blewitt et al. reported that co-seismic displacements for the GPS stations MOGL and RENO were oriented toward one another. MOGL and RENO are shown on the map of Figure 6. This relative motion was best explained by right-lateral strike-slip on a vertical fault. From InSAR data, the Bell et al. preferred model for the rupture plane was 3.3 km in length and 1-5 km in width. Width is in the vertical direction because of an assumed vertical fault plane and not well defined because of limited sensitivity of the InSAR data. The top of their preferred rupture was placed at 2 km beneath the surface, in fair agreement with our results. Figure 6 shows that the InSAR fault location was estimated as very near MOGL, with an approximately southeast strike. The strike was very

nearly in agreement with the pattern of aftershocks in Figure 2; however, the fault location would lie roughly 0.5 km southwest perpendicularly from the location indicated by the HYPODD results. This result was somewhat surprising. The P-arrival times, with MOGE arriving first, indicated that the fault was near the MOGE location, certainly not as far as MOGL. On the other hand, the agreement between the GPS and InSAR data in regard to surface displacements requires the fault to lie very close to MOGL and to the southwest side in order to get converging displacements between MOGL and RENO. It is unlikely that the seismic velocity was heterogeneous enough to allow greatly biased travel times to the four seismic stations of Figure 7. However, they are all placed to the west of the HYPODD epicenters and thus do not have good east-west control; this lack of control is reflected by the smearing in the grids of Figure 8 along roughly an azimuth of 30°. This may be simply a case where epicenter accuracy is strongly diminished by non-uniformity of the true earth structure when a flat-layered model is used to locate seismic events.

Table 1 Main shock depth from available sources.

Source	Origin time	Lat (deg)	Lon (deg)	Depth (km)	Earth model
NEIS PDE	2008/04/26 06:40:10.61	39.520	-119.930	1.40	model unknown
NSL original catalog	2008/04/26, 06:40:10.6	39.5247	-119.9180	3.08	pickema2
Berkeley	2008/04/26, 06:40:14.0	39.4687	-120.0587	3.5	model unknown
Herrmann	2008/04/26, 06:40:10.0	39.520	-119.930	1.0	Herrmann
NSL HYPODD	2008/04/26, 06:40:10.6	39.5238	-119.9186	2.63	pickema2
NSL HYPODD	2008/04/26, 06:40:10.59	39.5244	-119.9175	2.76	KS
NSL HYPODD	2008/04/26, 06:40:10.6	39.5244	-119.9172	2.76	IT
IRIS	2008/04/26 06, 06:40:12.6	39.45	-119.95	5	model unknown

Table 2 Seismic velocity model parameters.

KS		pickema2		Herrmann		IT	
Top of the layer (km)	P velocity (km/s)	Top of the layer (km)	P velocity (km/s)	Top of the layer (km)	P velocity (km/s)	Top of the layer (km)	P velocity (km/s)
0.0	3.5	0.0	5.9	0.0	3.4	0.0	2.9
1.0	4.5	7.0	6.0	1.9	5.5	1.0	3.8
2.0	5.5	22.1	6.7	8.0	6.3	2.0	5.8
4.0	6.0	28.1	7.9	21.0	6.4	4.0	6.4
7.0	6.4			40.0	7.9	6.0	6.9
12.0	6.6					8.0	7.2
18.0	6.8					18.0	7.8
						30.0	8.0

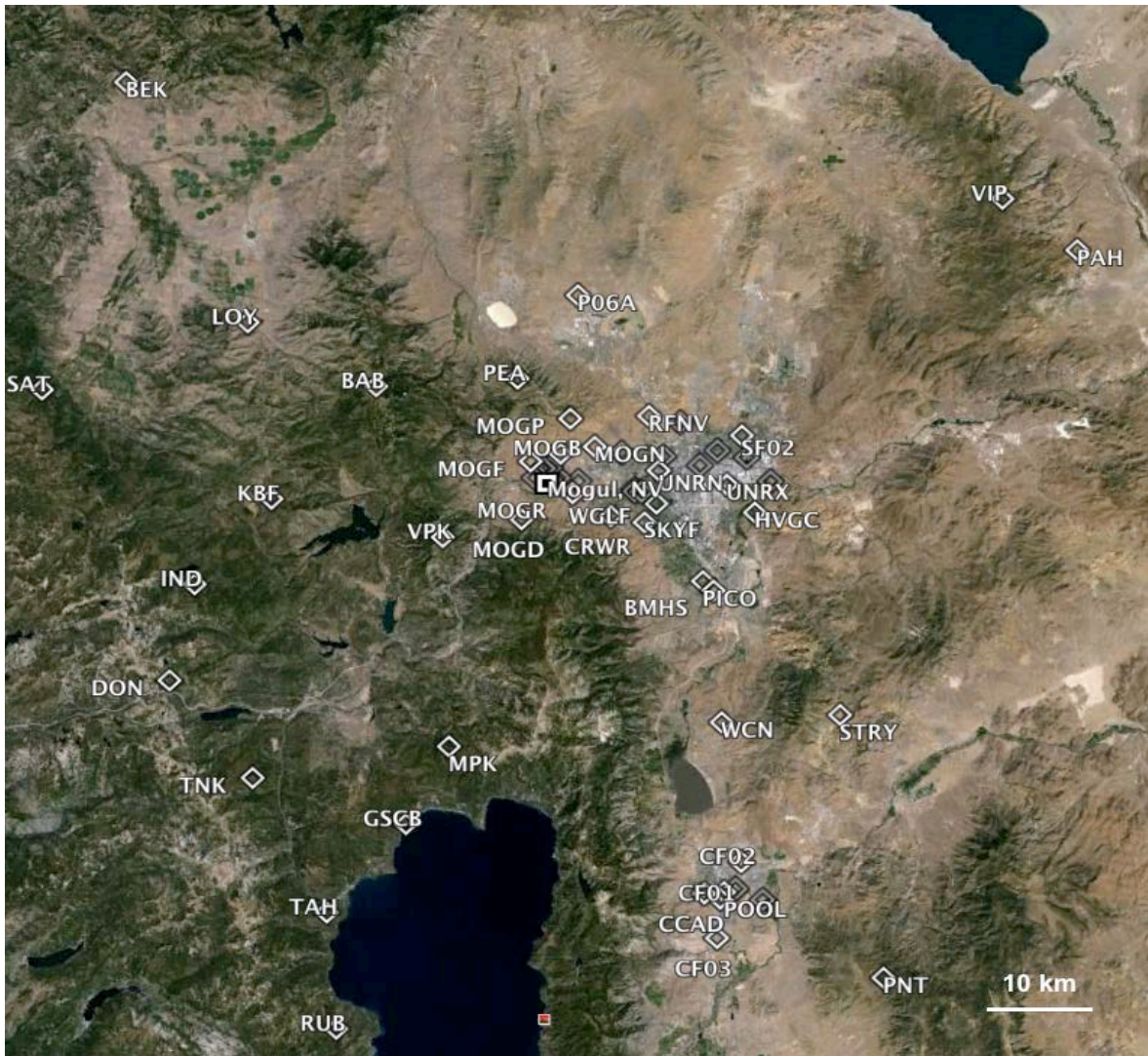


Figure 1. Stations used in locating the Mogul earthquakes sequence. *Only the closest stations are shown because they have heavier weight in refining the hypocenters. Some station labels have not been included where stations are tightly clustered. The site of the Mogul earthquakes is identified as “Mogul, NV” near the center of the figure. Reno itself is roughly 10 km east of Mogul.*

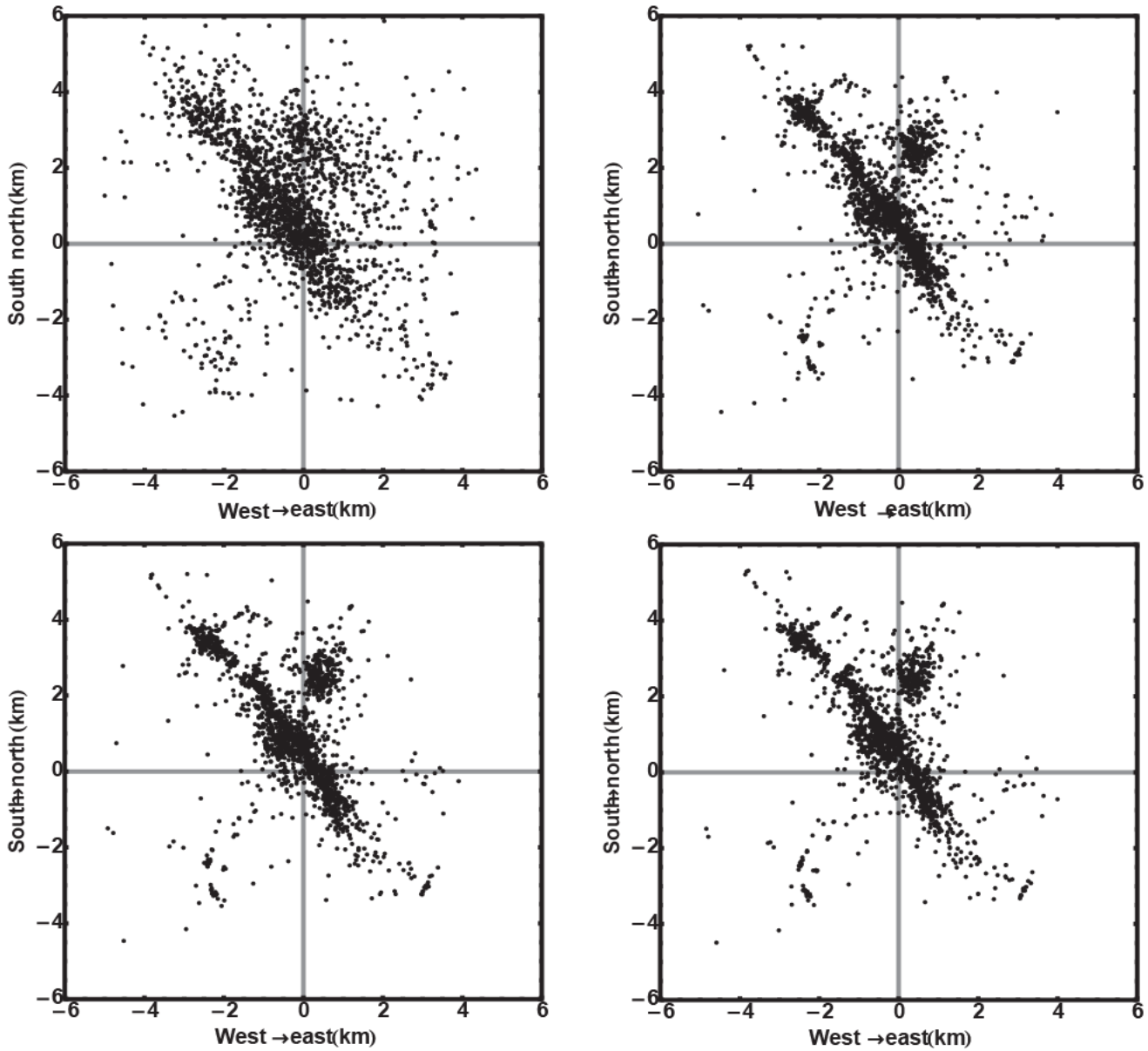


Figure 2. Mogul sequence location results shown in map view. The horizontal axis shows east-west distance in km relative to the main shock location and the vertical axis shows north-south distance (km) relative to the main shock location. Clockwise from upper left the figures show the cases named: “cat”, “ct”, “cc”, and “equal”. See text for the meaning of labels. The main shock location is shown with a large white dot. The (0,0) point is arbitrarily placed at the NEIS location (119.93W, 39.52N).

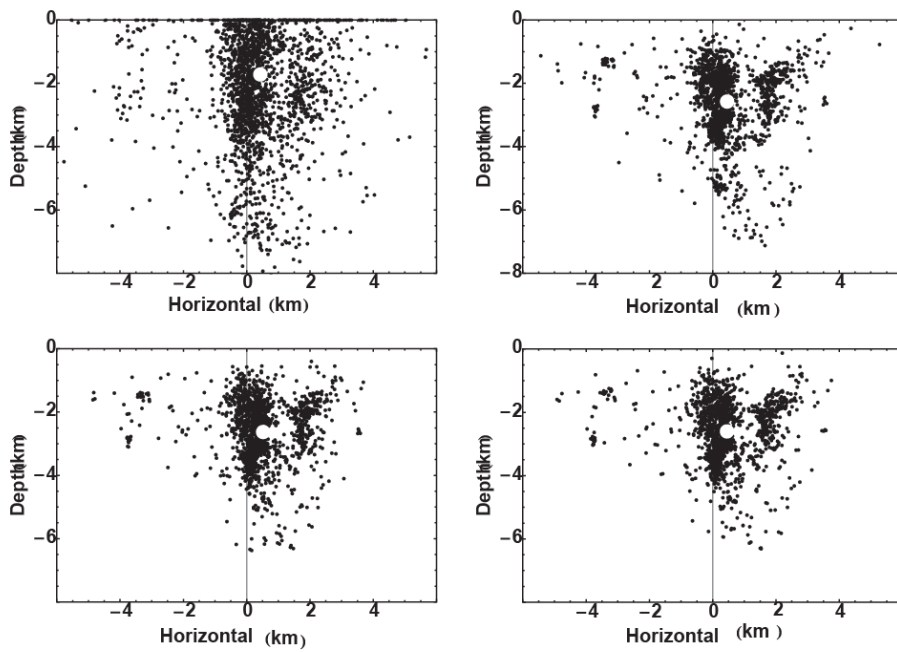


Figure 3. Mogul sequence location results shown in a cross-section along azimuth 53° east of north. *Clockwise from upper left are the cases “cat”, “ct”, “cc”, and “equal”. See text for the meaning of labels. The main shock location is shown with a large white dot.*

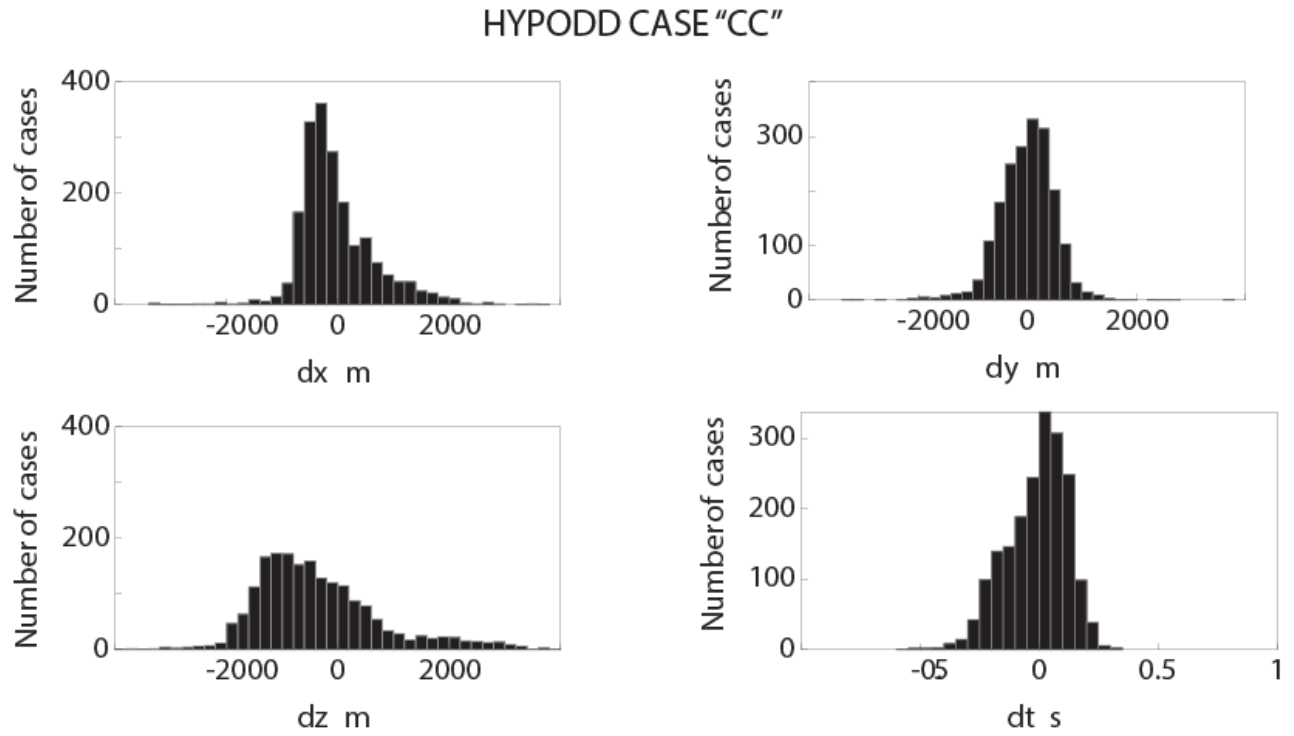


Figure 4. Hypocenter shift histograms for the NSL catalog hypocenters relative to the HYPODD ones (case "cc" for HYPODD in Figure 2). Shifts are, for example, $dx = x_{\text{catalog}} - x_{\text{HYPODD}}$.

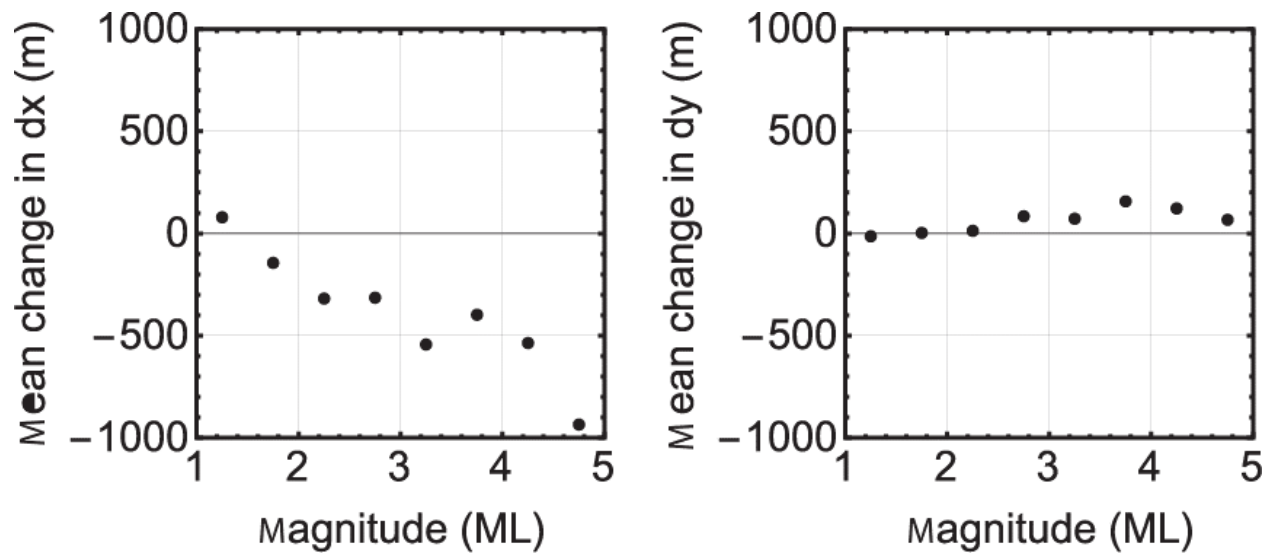


Figure 5. Mean shift for the NSL catalog epicenters relative to the HYPODD ones (case “cc” for HYPODD in Figure 2). Shifts are, for example, $dx = x_{\text{catalog}} - x_{\text{HYPODD}}$. The means are taken in 0.5 bins of ML for $1.0 \leq ML < 5.0$. Note that only the main shock with $ML = 4.7$ contributes to the mean in the last bin of $4.5 \leq ML < 5.0$.

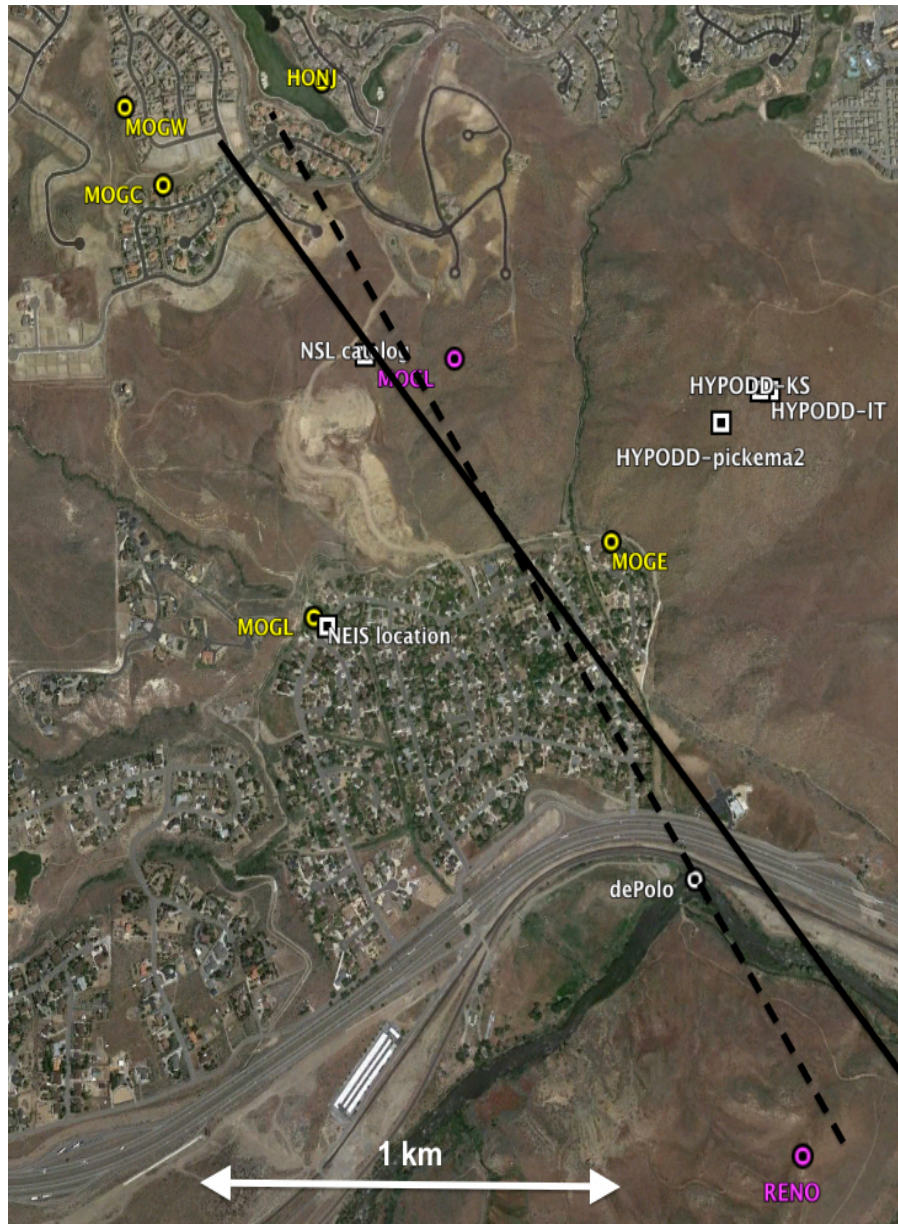


Figure 6. Map of the Mogul main-shock epicenters estimated using velocity models shown in Table 1. The 5 nearest stations are MOGE, MOGL, MOGW, HONJ, and MOGC are shown with yellow circles. MOGC did not record the main shock. Two geodetic stations RENO and MOGL (coincidentally named the same as the seismic station) are shown with magenta circles. The three HYPODD locations with three different velocity models are shown with white squares. The oblique solid black line, with a strike of 318° , is the rough position of the fault trace projected to the surface from InSAR data (Bell et al., 2012) -- note that geodetic stations MOGL and RENO, having opposite displacements, straddle this line. An alternate dashed black line with a strike of 326° , is proposed as consistent with the Figure 2 aftershock zone, the geodetic observations, and the constraint of faulting observed by dePolo (pers. comm., 2014).

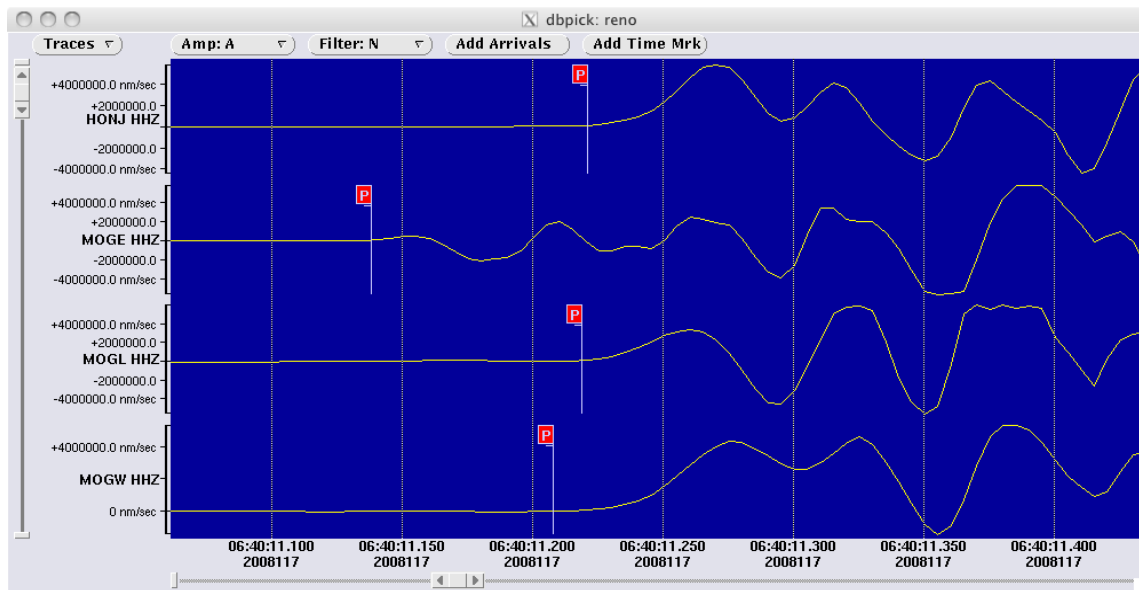


Figure 7. P arrivals at the four closest stations (HONJ, MOGE, MOGL, MOGW) to the main shock epicenter.

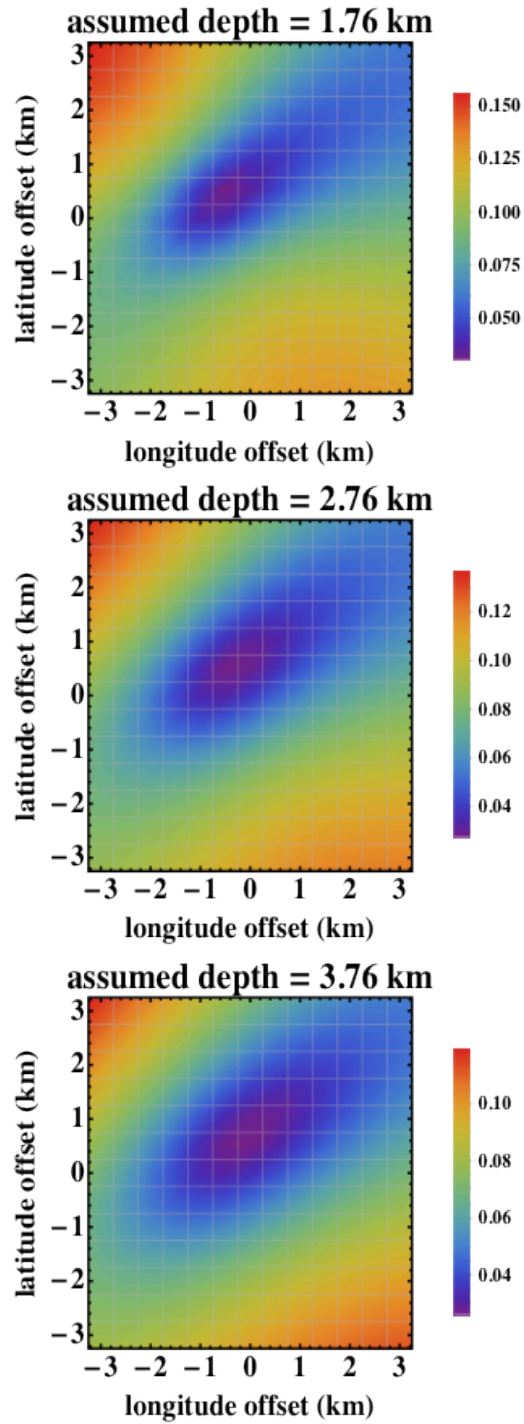


Figure 8. Tests for the best hypocenter with respect to the P-wave arrival times at the closest four stations (HONJ, MOGE, MOGL, MOGW). The (0,0) point at depth = 2.76 km is the preferred HYPODD epicenter. The scale represents the rms of the difference between predicted and actual times.

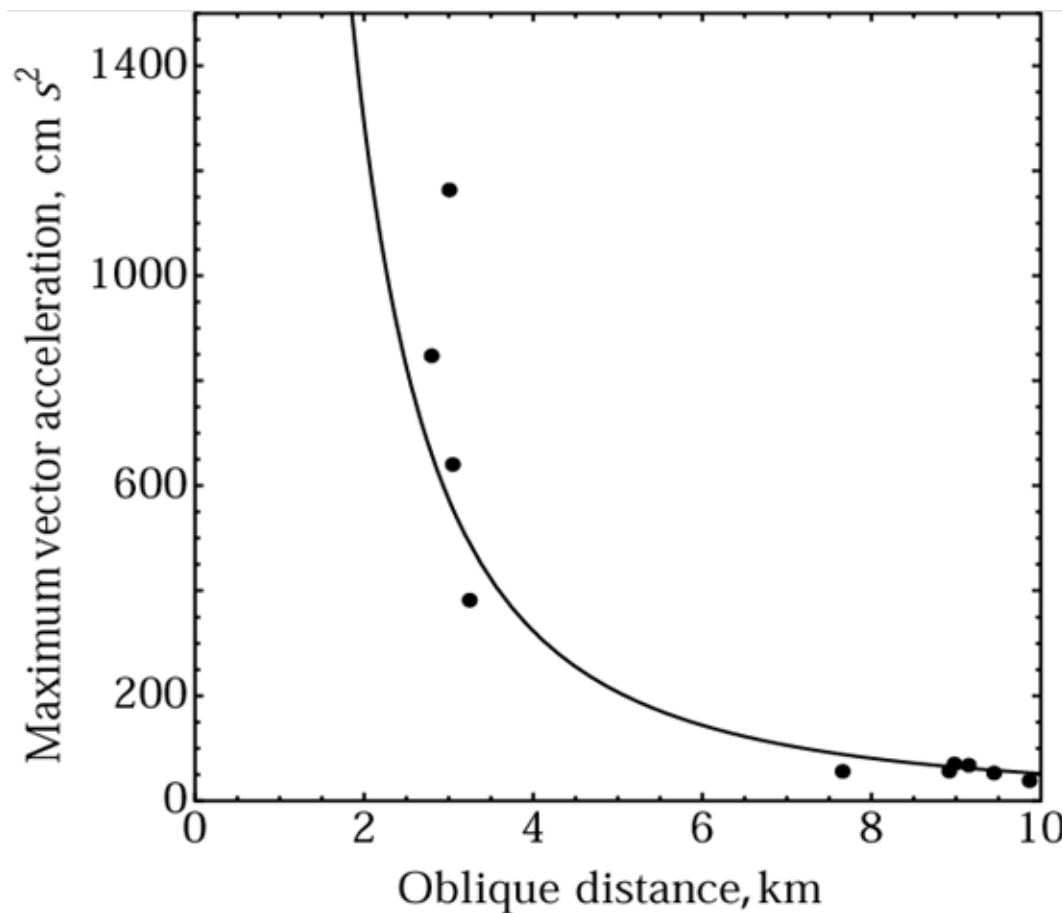


Figure 9. Maximum recorded peak vector acceleration versus the oblique distance from the preferred HYPODD hypocenter for the Mogul main shock. The line represents a decay according to kr^{-2} where the constant k is a least-squares fit to the data points.

4.1.2. Seismic Velocity in the Source Area

by Glenn Biasi and John G. Anderson

The seismic moment depends on the cube of the shear-wave velocity, so this parameter was especially important for moment and magnitude scaling evaluations. Using the strong-motion station SKYF, located along the Mogul fault strike, epicentral distance r and elapsed time t_s (S-arrival time minus origin time) were computed using HYPODD relocated events. A linear fit, $t_s = 0.348 r + 0.38$ (s), and a shear-wave velocity of 2.87 km/s were estimated by least-squares (Figure 11, left upper plot). Residuals to the linear fit, (Figure 11, lower left plot), showed no systematic dependence of depth. A source-region P -wave velocity of 5.13 km/s (P elapsed time $t_p = 0.195r + 0.008$) (Figure 2, right upper plot) was estimated using the same method. This direct estimate of V_p was similar, within errors, to that of the Herrmann velocity model (Table 2), and was slower than the KS and NOISE models. The source-region shear-wave velocity estimated with this method was used to develop estimates of seismic moment, M_o for the $M_L \geq 3.0$ Mogul earthquakes.

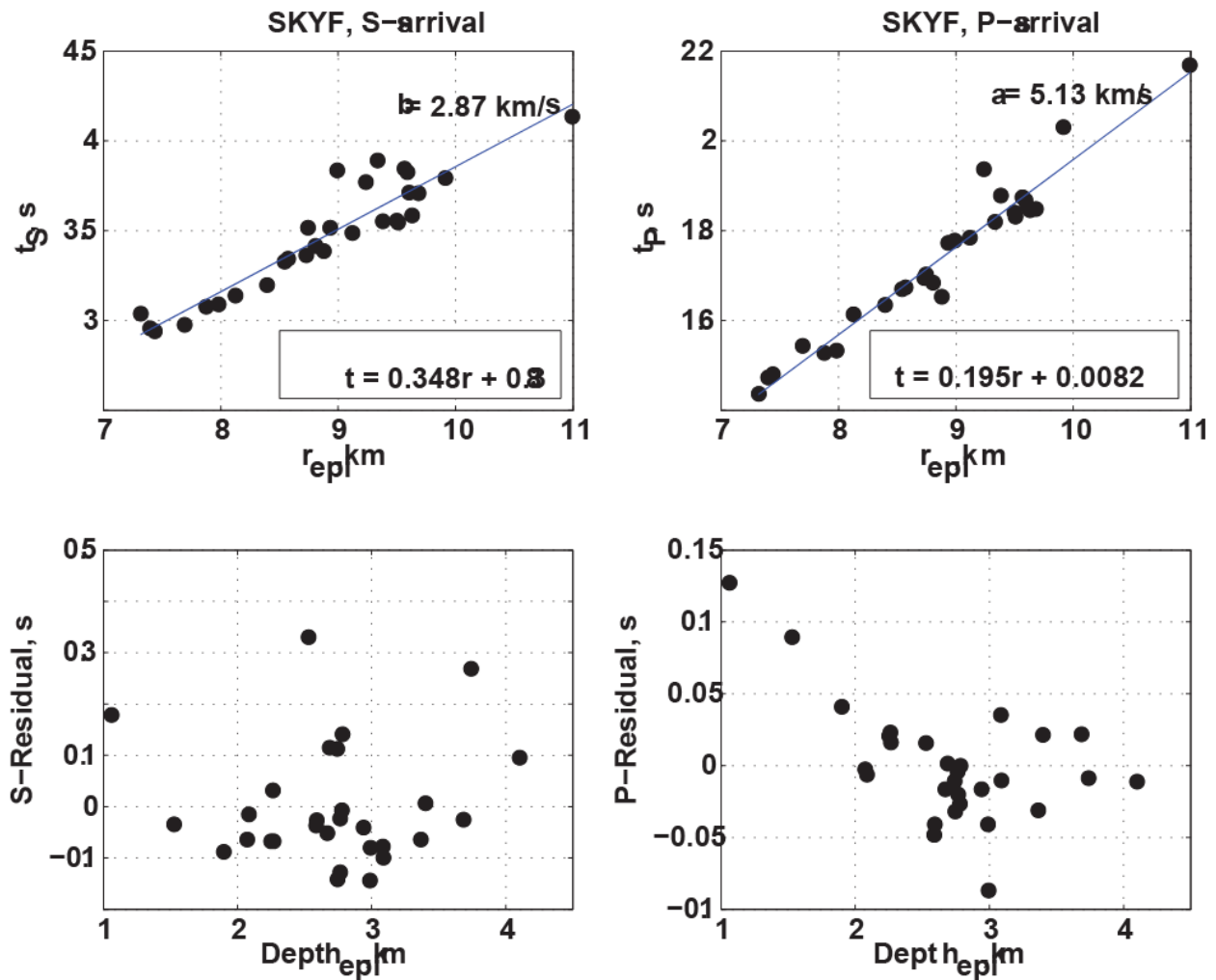


Figure 10. P- and S-wave travel times versus distance and depth. (Top-left) Shear-wave transit times (observed arrival time – origin time) t_s plotted versus epicentral distance (km) provide a direct estimate of the shear-wave velocity of the source area. (Bottom-left) S-time residuals show no systematic variation with hypocentral depth indicating that the source area velocity gradient is small. (Top-right) A source area P-wave velocity of 5.13 km/sec is estimated from differences in P-wave transit times to station SKYF. (Bottom-right) Residuals to the linear fit plotted versus depth show no systematic trend for sources below two km depth, however suggest lower velocities at shallower depths for the three shallowest events.

4.2 Task 2.

Objectives:

1. Analyze the stress drop and radiated energy of the main shock and principal fore- and aftershocks;
2. Investigate the source scaling of the Mogul sequence.

4.2.1. Stress Drop and Radiated Energy of the Main Shock and Principal Fore and Aftershocks

INTRODUCTION

The 2-4 km hypocentral depths of earthquakes of the Mogul sequence raise the question of whether other source parameters including stress drop and corner frequency are also anomalous. Low stress drops might be predicted if stress drop scales with fault-normal stresses due to lithostatic pressure. The more typical minimum seismogenic depth of 5 km is commonly interpreted as the depth at which lithostatic stresses begin to be sufficient to support processes of stress accumulation and release associated with earthquakes. For the same reasons, shallow earthquakes might be anomalous in terms of the energy that they radiate as compared to events at greater depths. Estimation of source parameters for moderate earthquakes of the Mogul sequence thus addresses whether these earthquakes appear normal or anomalous when considered from a discrimination point of view. In addition, accurate estimates of seismic moment and frequency content from near-field recordings can be used to calibrate source estimates developed using regional methods. Thus source parameter estimates for Mogul sequence earthquakes are important both to understand the phenomenology of shallow earthquakes and to ensure that methods exist to detect them and discriminate them from other types of ground motions.

Estimates of M_w , M_o , corner frequency, and stress drop were developed for earthquakes of the Mogul sequence having an initial local magnitude $M_L \geq 3.0$. At about M_L 3.0 earthquakes are large enough that with near-field recordings, earthquake parameters including corner frequency, stress drop, and moment can often be resolved. Parameter resolution normally improves with increasing magnitude, but the number of events to study decreases; the cutoff of $M_L \geq 3.0$ balances the goal of a large sample size with the desire to focus on useable spectral parametric estimates.

METHOD

For purposes of estimating the seismic moment, analysis focused on strong-motion recording stations at epicentral distances less than 25 km. This subset was selected for a few reasons. First, because these stations did not clip for any of the events in the sequence. This removed the question of non-linear response of broadband sensors near their limits. Also, limiting stations to short epicentral distances decreases the role of seismic attenuation such that it can be modeled by a simple linear function of frequency and the geometric decay rate of body waves can be modeled as a simple $1/r$ function. Finally, broadband recording station coverage was too little and too far away to provide well resolved spectral parametric estimates.

Estimates of seismic moment, stress drop, and corner frequency were developed in a three-step process. The process proved to be more complicated than was envisioned in the proposal because of strong involvement of surface waves shortly following the direct S arrival and unavoidably in the S-wave analysis window.

RESULTS

1. Fitting for Spectral Parameters

Spectral fitting parameters including moment, corner frequency, and kappa were estimated from recorded time series using program kappaAH. A modified version of the Matlab code kappaAH (Biasi and Anderson, 2007) was used to develop these estimates. kappaAH fits individual spectra one at a time, writing to custom flat-file tables that extend the input database. KappaAH is designed to deal with events of moderate size where the corner frequency and the effects of attenuation interact to obscure the actual corner frequency (Anderson, 1986, 1991; Anderson and Humphreys, 1991). For data recorded at the surface this interaction can be expected for earthquakes in the range $3 < M < 5$.

Kappa-Attenuated Brune Source Model ("Brune-k")

Kappa was originally defined as an observational parameter describing the high-frequency slope of large earthquake accelerograms (Anderson and Hough, 1984). No assumptions were made about the shape of the source spectrum itself, and it could only be applied to earthquakes with low-enough corner frequencies to argue that the corner frequency did not matter. Distance dependence in the kappa estimate was attributed to attenuation (Q) effects. Kappa was subsequently added to the Brune (1970) spectral model shape in order to provide a more complete model of seismic spectrum $M(f,r)$:

$$M(f,r) = \left(\frac{\Phi M_0}{4\pi\rho\beta^3 r} \right) \left(\frac{(2\pi f)^\gamma}{1 + \left(\frac{f}{f_0} \right)^2} \right) \exp(-\pi\kappa f) \quad (1)$$

In this equation M_0 is the seismic moment, f_0 is the corner frequency, and *kappa* (κ) scales the slope of spectral decay with frequency. Constant Φ is the average radiation pattern (0.85), β is the shear wave velocity at the source, r is the hypocentral distance (cm), and ρ is the rock density at the source (2.60 gm/cm³), and f is frequency in Hz. Shear velocity β was estimated at 2.87 km/s directly from time-distance data of the Mogul swarm. The data type determines variable *gamma*, with $\gamma = 0, 1$, or 2 for displacement, velocity, or acceleration spectra, respectively. The observed S-wave spectrum $A(f)$ will have, in addition to $M(f,r)$, contributions from the source-station path, $P(f,r)$, and the site beneath the station, $S(f)$:

$$A(f) = M(f,r)P(f,r)S(f) \quad (2)$$

$S(f)$ is distinguished from path effects by affecting all recordings in an approximately equal manner, while $P(f,r)$ can vary from one event to the next depending on back azimuth and distance. More sophisticated models for $A(f)$ might be proposed.

Corner frequency f_0 is an observational parameter related to the area of rupture and the time the rupture takes to cover it. In Equation 1 f_0 causes a downward curvature. As the corner frequency increases separate curvatures caused by f_0 and $\exp(-\pi\kappa f)$ merge and the simple, slope-only model for κ fails. To estimate spectral parameters from smaller earthquakes, Anderson and Humphrey (1991, abbreviated "AH-91") proposed that κ be identified with the residual slope of an acceleration spectrum after removing a Brune-model source spectrum (the left two terms in Equation 1). When the earthquake source spectrum follows this shape, the AH-91 κ definition is equivalent to the simple slope definition of Anderson and Hough (1984). This is the spectral model implemented in *kappaAH*.

We solve for M_0' and κ by least-squares fitting the observed spectrum to a version of Equation (1) at frequencies f_i :

$$\ln[M(f_i, r)] = \ln(M_0) + \ln A_0 - \pi\kappa f_i + \ln \left(\frac{(2\pi f_i)^{\gamma}}{\left(1 + \left(\frac{f_i}{f_0}\right)^2\right)} \right) \quad (3)$$

This equation would be difficult to solve directly, but becomes linear in M_0 and κ if f_0 is known or assumed. A solution is found by trying a range of corner frequencies, solving for M_0 and κ for each trial f_0 , then choosing the corner frequency that gives the best fit to the observed spectrum. In this formula, A_0 represents the several elements in the first square brackets of Equation 1, and γ is set according to the data type. The squared error of the fit,

$$E^2(f_0) = \frac{1}{NF} \sum_{i=1}^{NF} [\ln(A(f_i)) - \ln(M(f_i))]^2 \quad (4)$$

is used to evaluate fits, where $A(f)$ is the S-wave spectrum estimated from the seismic time series and NF is the number of frequency bins in the spectrum. Only minima of E^2 inside the frequency range (i.e., not end values) are candidate solutions.

2. KappaAH and Spectral Fitting

As a first step we applied *kappaAH* directly to the observed seismic data. *KappaAH* first extracts a 10-second window from each time series from 1 second before the S arrival to 9 seconds after, and another window of the same length ending before the P arrival. Next, it estimates the corresponding spectra, and fits the spectrum using a kappa-attenuated Brune (“Brune-k”) spectral model. *KappaAH* assumes corner frequencies in a range thought sure to include the actual value, and solves for misfit and Brune-k model parameters for each. This leads to a joint solution for *kappa* and corner frequency together, and ensures at least a level of compatibility among spectral parametric estimates. Compatibility among parameters has to be ensured by other means when using strategies such as constraining the moment separately. Visual documentation files are developed for every spectral fit (Figure 11).

It can occur that no corner frequency leads to a convincing minimum misfit to the Brune spectral shape. The spectral model itself and attenuation expressed in *kappa* both cause a rapid decrease in spectral amplitude with increasing frequency. Many of the Mogul $M_L \geq 3.0$ event spectral fits either converged to a minimum misfit at unphysically high corner frequencies or did not converge at all. Non-convergence is common where event-station distances are greater than ~30 km and for any station where site effects are complicated relative to the linear roll-off assumed in the kappa attenuation approximation. For event-station separations of less than 10 km and events of this size, failure to converge is a symptom that either site effects are systematic and strong, or that more fundamental issues are affecting the estimates. Horizontal component estimates for three of the four near-field stations operating on the day of the Mogul main shock (maximum hypocentral distance 4.0 km) gave estimates of stress drop in excess of a kilobar (two examples in Figure 11), and the fourth station averaged a possible, but improbably high 280 bars.

P-wave spectra were not pursued for the near-source Mogul earthquakes because of the exceptionally short S-P times of most events. For the main shock (Figure 11, top panels), the S-wave began arriving before the P-wave was complete. As may be seen from the waveforms, the P-wave is also emergent, suggesting that the rupture began relatively slowly. With distance the P-wave does separate from S, but attenuation and scattering lead to low amplitude P arrivals with non-descript shapes.

3. Removal of Site Effects

In light of the unphysical estimates for stress drop and corner frequency developed by applying *kappaAH* directly, alternate approaches were explored to obtain moment and corner frequencies likely to represent the Mogul $M_L \geq 3.0$ events. As a first step, we removed the systematic frequency dependent deviations from the Brune-k model spectrum. If the kappa-attenuated Brune spectral shape is appropriate, then the systematic part of a frequency-dependent residual after fitting to that shape will include the site effect $S(f)$ and any consistent component of the path term. Since source-station distance differences are small, the distance dependence of $P(f, r)$ reduces to a simple frequency dependence. Thus in removing the frequency-dependent residual, properly both contribute, but we can model it as though it is a simple site effect.

We estimate site effects for each site and channel by calculating a model Brune-k spectrum using fitting parameters from step 1, and compiling residuals (Figure 12). The log-averaged residual to the model spectrum is then the average frequency dependent site effect (Figure 13).

A test for the appropriateness of the Brune-k spectrum is that at low frequencies, the ratio of the model and data should approach 1.0 because the site effect at low frequencies averages over larger volumes and becomes insensitive to particulars of the site. For strong-motion stations in the Reno area the observed ratio is close to 1.0. For near-field stations however (especially MOGL, MOGW, and HONJ), strong departures from the model spectrum were observed (Figures 12, 13). In particular, spectral roll-off at low frequencies steeper than f^2 is observed. Using the example in Figure 12, two interpretations could be considered. One would be that the lowest frequency spectral levels are correct, and that energy above the lowest frequency (above the red dashed line) is in excess of the Brune-k model. This would amount to a strong, broad-band amplification from 1 to at least 10 Hz. Alternately, a strongly absorbing site effect could be present to remove energy below 1 Hz. At more distant stations this discrepancy at low frequencies was not observed. For example, station RFNV (Figure 14), is about 10 km epicentral distance from the Mogul sequence, and on moderately stiff volcanic rock. As may be observed, station RFNV has a relatively moderate frequency dependent site effect. In other studies of the Reno basin (Pancha et al., 2007), RFNV has been used as a local rock reference.

While most stations in the Mogul area showed a spectral excess exemplified in Figure 13 stations at a distance of 10 km and greater did not. Figure 14 shows residuals for station RFNV at an epicentral distance of 10 km; the spectral excess is gone. Other examples are shown in Figure 15. A map of affected and unaffected stations (Figure 16) shows that the spectral excess is not observed beyond the immediate Mogul area.

Through helpful interactions with the MRR community, it was determined that the first interpretation of Figure 12, of having a broad-band spectral excess, is preferred. The steep spectral fall-off in nearest stations occurs because spectra systematically include an additional high-frequency surface wave phase. Surface wave motion is shown in Figure 17. Prominent elliptical particle motions are observed at three of the four stations nearest to the mainshock using data from one second before P to 5 seconds after. A representative S-P time for these events is 0.4 to 0.6 s. There is no way to exclude this Rg phase from the S-wave spectra because of the small source-station distances. The excess surface wave energy makes S-wave spectra from the nearest stations inappropriate for estimation of M_0 and M_w .

4. Estimation of Moment and Stress Drop

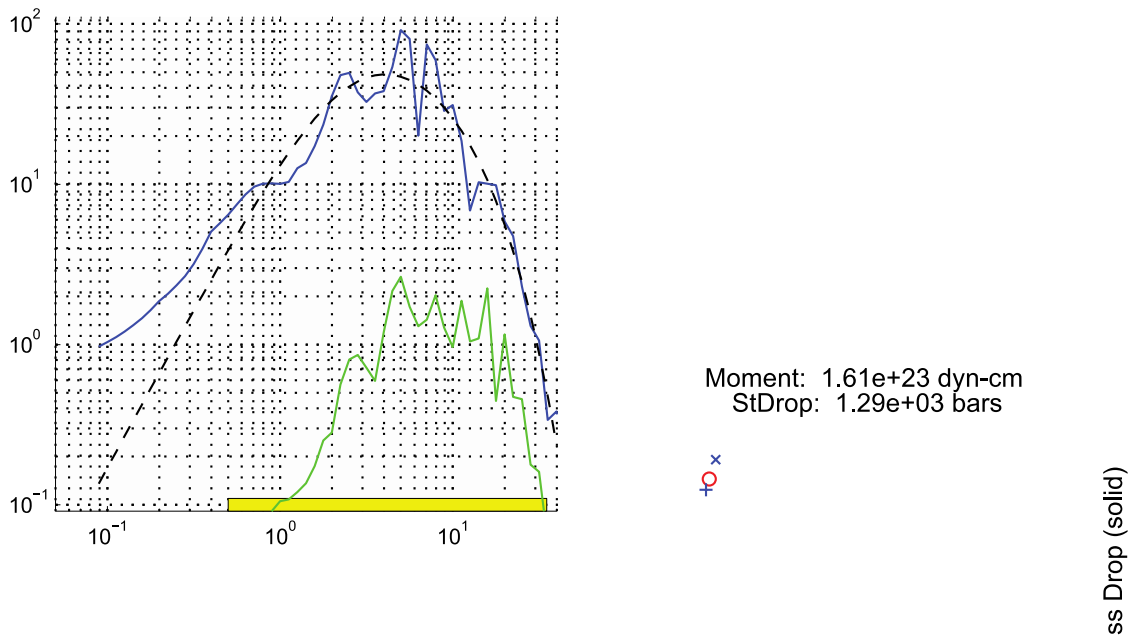
As noted above, stations away from the source were observed to not have the over-steepened low-frequency roll-off, apparently because the surface wave is strongly attenuated. In step three, strong-motion stations from 5-22 km hypocentral distance were gathered for the purpose of averaging moment and corner frequency for each event. The stations in this distance range that recorded the $MI \geq 3.0$ events on scale are comprised mainly of Reno-area urban strong-motion accelerometers. Weak-motion stations (esp. PEA) were often clipped by M3 events, and could not be used reliably. Confirming findings from previous studies stations RFNV and SWTP at ~10 and 20 km distance, respectively, were found to be rock-like, with moderate frequency-dependent site effects and negligible low-frequency amplifications. Other Reno basin strong-motion sites had expected f^2 low-frequency roll-offs, but systematically larger moments consistent with site amplification in the $0.5 \leq f \leq 35$ Hz spectral fitting band. In principle low-frequency moments should converge to a common moment, but spectral bandwidth was insufficient and signals too small at low frequencies to demonstrate this.

The log-averaged moment from rock sites RFNV and SWTP were used to estimate an average correction for the soil sites. On average soil sites event-averaged seismic moments were a factor of 2.35 greater

than the rock sites. This difference was used to reduce M_0 estimates from parameter estimates from soil sites. After correction, event averaged magnitudes were developed. The averaging process over all stations is not the same as simply using the rock station moment estimates. On average we do assume that the rock sites are unbiased, but on an event-by-event basis, it is possible that the seismic radiation pattern or other event-specific effects could affect the rock station average. The larger station cohort is more sensitive to DC shifts in magnitude than any two individual stations. The results (Figure 18) show that the magnitudes from all stations do not differ on average from moment magnitudes from the rock stations alone. M_w was estimated from moment using $M_w = (2/3)(\log_{10}(M_0) - 9.1)$, with M_0 in Newton-meters. Since there was an average difference of a factor of 2.35 in seismic moment estimates between the soil and rock sites, a systematic effect on corner-frequency and stress drop estimates could be expected. Figure 19 illustrates this difference. Though not verified, we suspect that basin-induced surface waves may contribute low frequency energy that affects spectral fitting. As a result, final estimates in Table 3 for corner frequency and stress drop were developed using only the log-averaged rock component averages. Figure 20 shows stress drop estimates of the Mogul $M_L \geq 3$ event set as a function of M_w . Rock component estimates (blue) are log-averaged to reduce the tendency of a single high value to strongly distort the average (red stars). Stress drops range from 0.36 to 13.2 MPa, with the main shock stress drop of 8.18 MPa or about 82 bars. This estimate is somewhat high relative to average crustal events, but still in what would be considered a normal range.

(a)

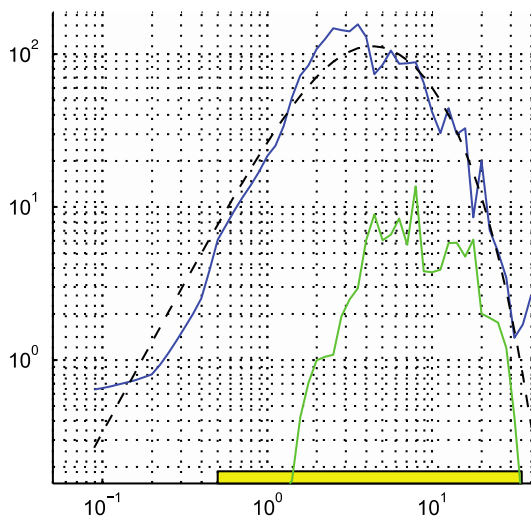
Mogul -- HONJ HNE Origin time: 4/26/08 (117) 06:40:10
---Lat 39.5244; Lon -119.9175; z=2.76 km; baz: 122.74 deg; hdist: 2.818



SNR: Signal to noise ratio; baz: back azimuth,
degrees; hdist: hypocentral distance, km.

Figure 11. a) KappaAH view showing the Mogul main shock east component accelerometer record at station HONJ. The upper frame shows the input time series and the pre-event window used for noise analysis. The Mogul main shock was preceded by a M_L 3.2 event by about 11 seconds. This put energy in the main shock noise window, which elevated the noise spectrum (green line, middle left), and decreased the signal-to-noise ratio (lower left). The Brune spectral model fit is shown as a dashed line in the middle-left plot. The spectral fit is taken over the frequency range shown by the yellow under-bar, here from 0.5 to 35 Hz. The peak energy is between 4.5 and 8 Hz. Across the range of trial corner frequencies (center right plot), some minimum misfit in a squared error sense (red star, middle-right) is found, and 75, 90, and 95% confidence points are also indicated. In this case the minimum misfit point is extremely well located. Stress drop in bars is indicated as a function of frequency in the lower right panel along with the seismic moment estimate. The stress drop, 1287 bars, is a symptom of a spectral problem causing the apparent corner frequency to be too high. Parametric results are tabulated in the lower text fields, as are the fitting parameters and constants such as density, seismic velocity, and the conversion constants from M_o to M_w .

(b) Mogul -- MOGL HNN Fitid No: 12607, Origin time: 4/26/08 (117) 06:40:10
 --- Lat 39.5244, Lon -119.9175 z=2.76 km, baz: 67.11 deg, hdist: 2.818 km



s; hdist: hypocentral distance, km.; evid:
 event identifier

Figure 11b: North component accelerogram from station MOGL for the main shock. *The spectral peak is between 2 and 4 Hz, noticeably lower than at HONJ. The peak north component acceleration exceeded 0.9 g.*

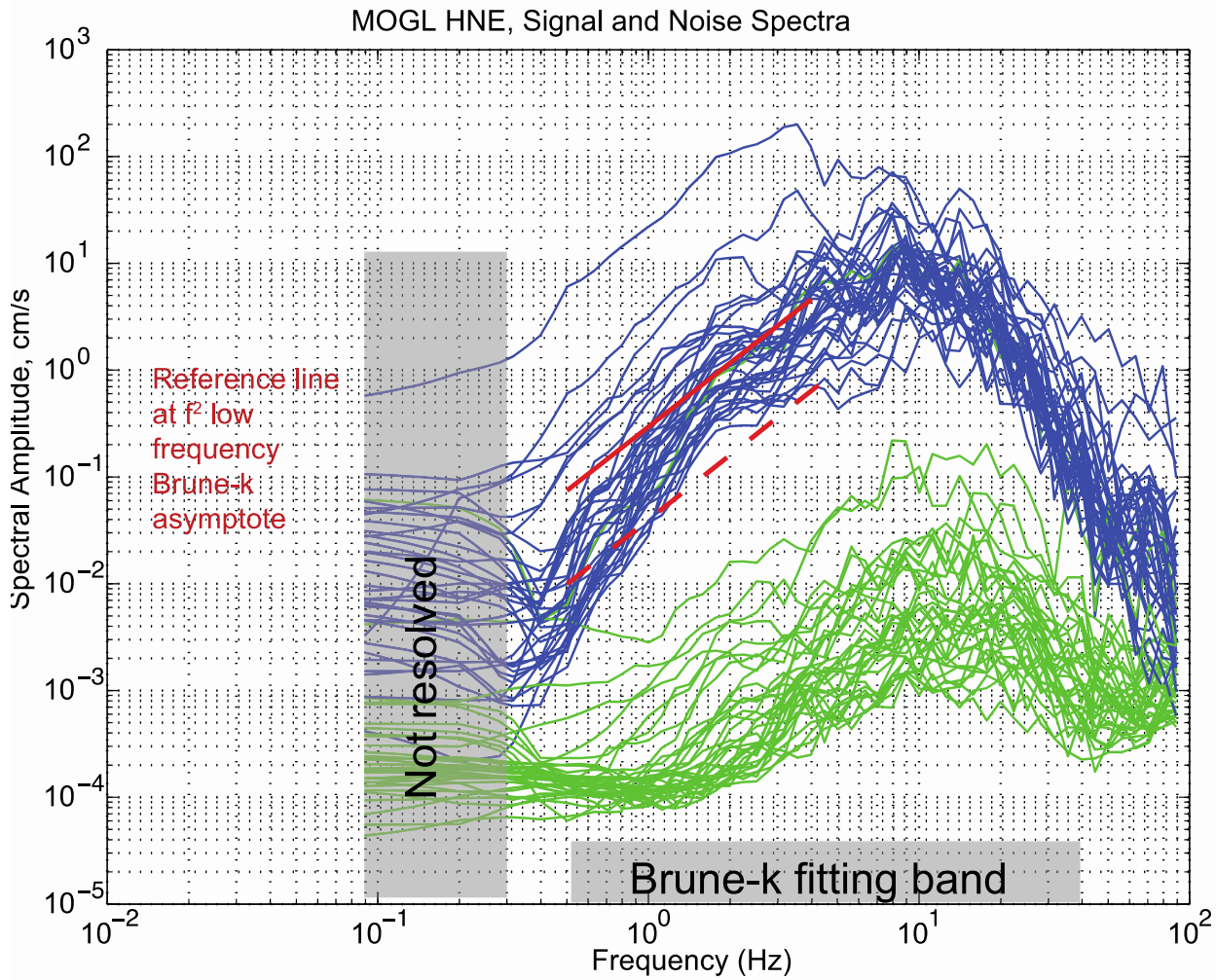


Figure 12. Shear-wave spectra for station MOGL, HNE channel for good signal-to-noise cases. Observed spectra are shown with blue lines, and pre-P noise in green lines. Reference lines show the expected f^2 low frequency slope of Brune-k model. Distance between the f^2 lines is representative of the excess amplitude if measured up from the dashed line, or missing low frequency amplitude if measured down from the solid line.

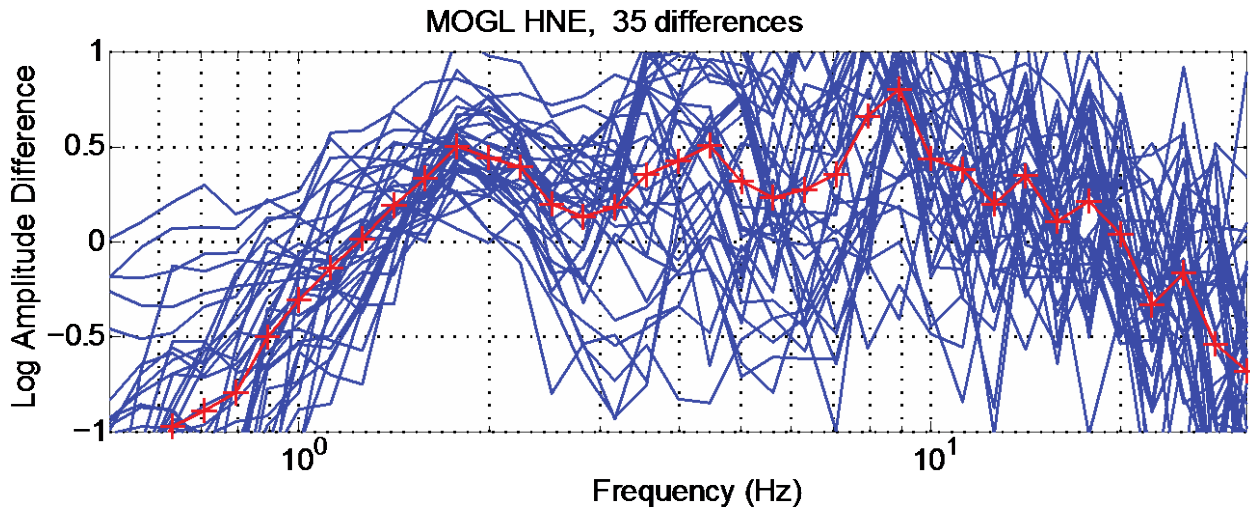


Figure 13. Residual spectra relative to Brune model. The blue lines represent residuals obtained by subtracting log base 10 of the best fit Brune- k model from the log of the observed spectrum for each $M_L \geq 3.0$. The red line is the mean of 35 total comparisons. The "+" symbols are included to make the red line more easily visible. The figure width is limited to the band in which spectra are fit, $0.5 \leq f \leq 35$ Hz. This plot shows that a systematic signal can be extracted from the spectral misfit. A clear excess of energy (ratio > 1.0) is evident between 1.5 and ~ 15 Hz.

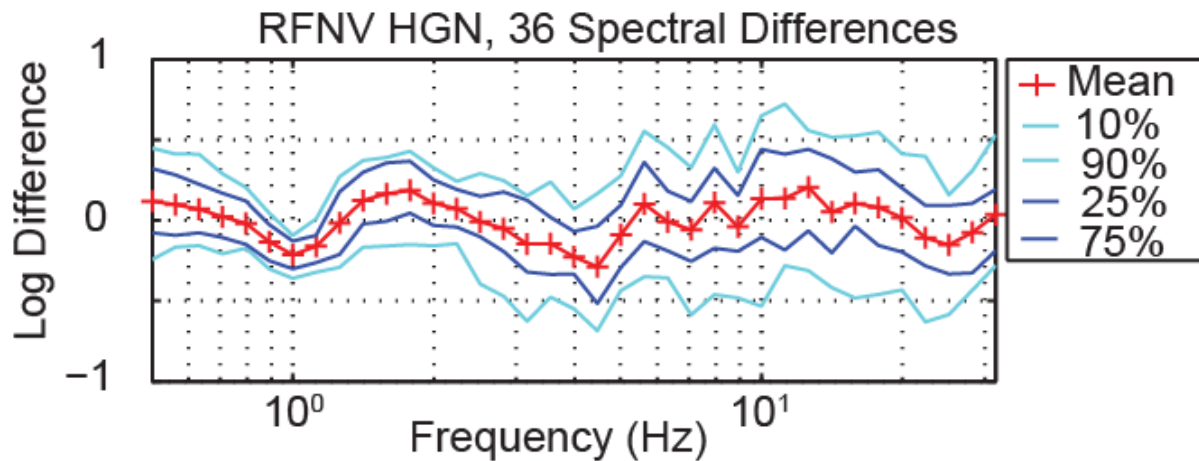


Figure 14. Station RFNV, the N-channel residuals to a Brune- k model source spectrum. Compared with Figure 4, only the mean deviation and empirical deviation ranges are shown. The relatively flat residual indicates that site effects are modest at this site and that the Brune- k spectral model reasonably describes the source. 36 events contribute to the average and range estimates.

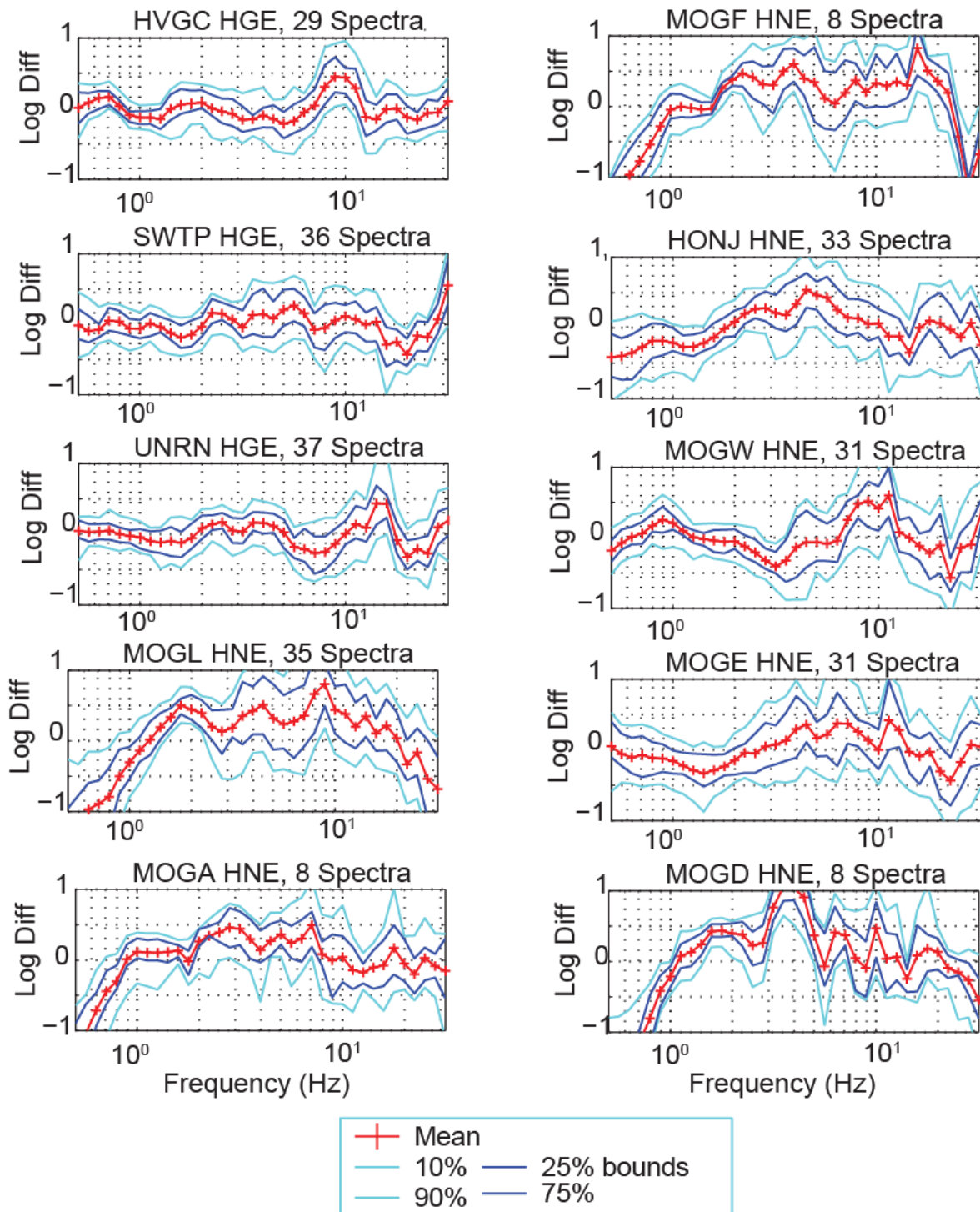


Figure 15. Example spectral residuals for ten stations near the Mogul swarm. Stations HVGC, SWTP, and UNRN are part of the Reno area permanent strong motion network, and are 18.2, 19.2, and 9.4 km, respectively, from the Mogul main shock. The other stations were deployed specifically for the Mogul swarm. Stations MOGL, MOGE, MOGW, and HONJ were deployed early in the swarm and recorded nearly the complete sequence.

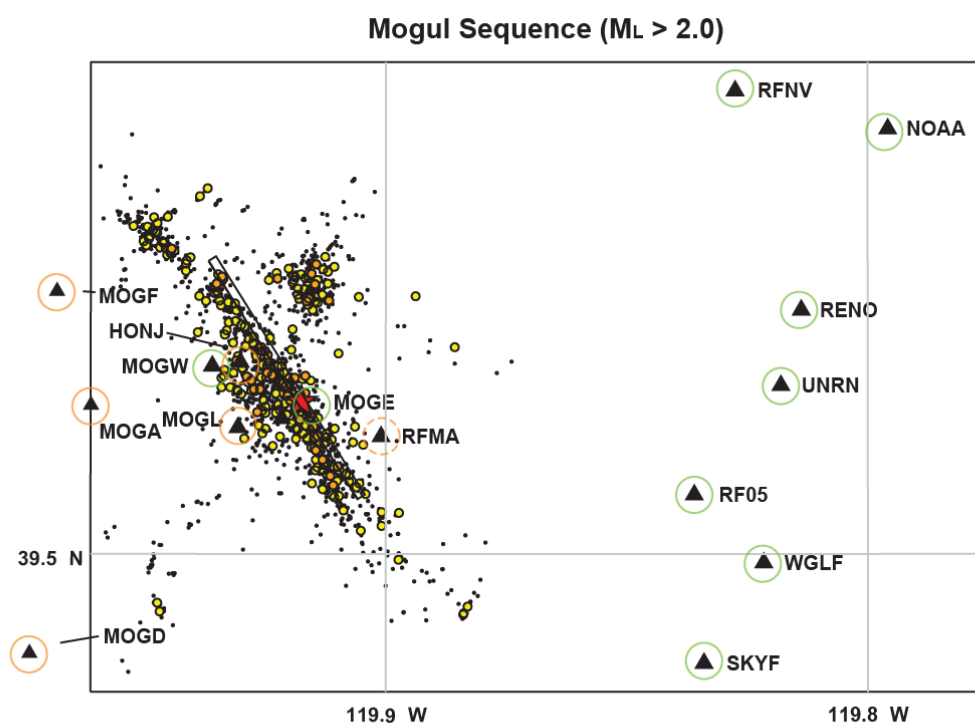


Figure 16. Map of stations and larger events of the Mogul sequence. Stations with orange circles have anomalous low-frequency spectral asymptotes indicative of surface wave phase contamination interpreted as R_g . Station RFMA is dashed because it is based on a very small sample. Attenuation of R_g is rapid; thus spectral asymptotes at green circles are normal. The red star shows our location of the main shock. Small filled orange circles show earthquakes with network $M_L \geq 3$, yellow circles show earthquakes with $M_L \geq 2$, and black dots show smaller events. Altogether, this figure shows 1953 relocated earthquakes between Feb. 25 and June 5, 2008.

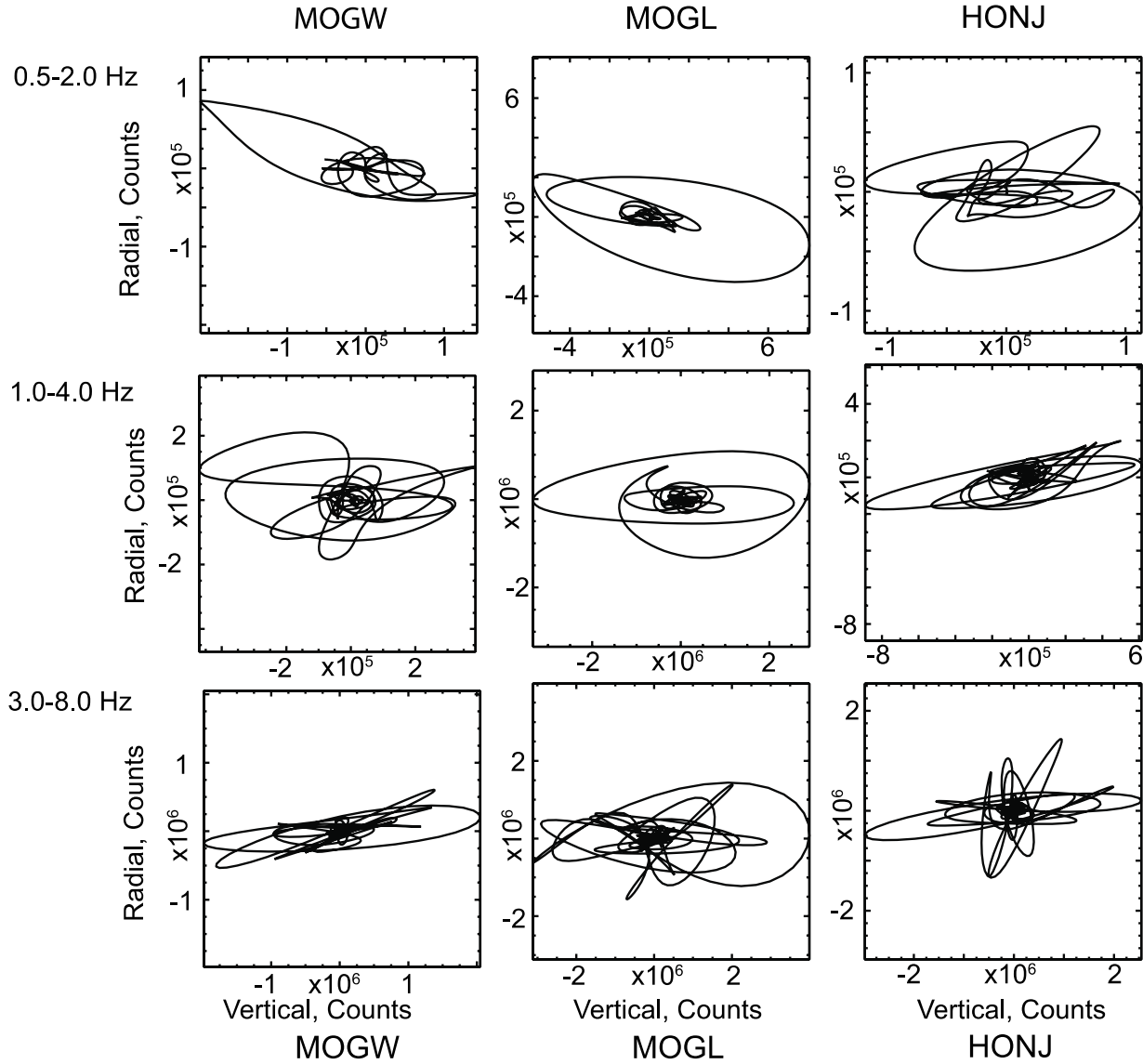


Figure 17. Particle motions for three near-field stations recording the Mogul main shock. *Pass bands for filters vary by row, as labeled in the figure. Radial and vertical component motions are plotted on horizontal and vertical axes, respectively. Elliptical motions diagnostic of surface waves are observed at all three sites, but most prominently in the 1-4 Hz band at stations MOGL and MOGW. Excess energy in this band distorts estimates of event corner frequency.*

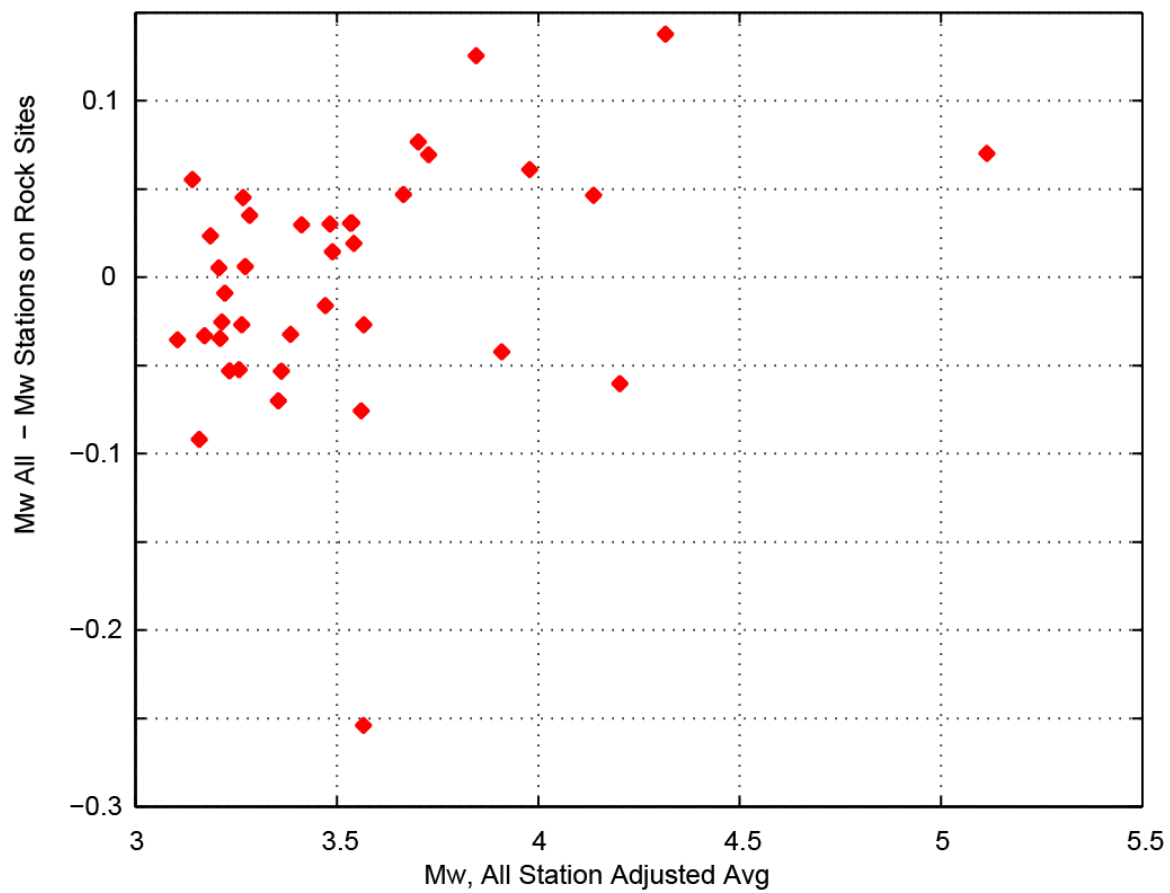


Figure 18. After adjusting soil sites downward by a constant factor of 2.35, M_w event average and rock M_w estimates agree well. Red symbols show the difference of event average and rock sites. There may be a small upward bias of the soil site contributions to the event averaged for the largest events, but averaged over all events, the difference in M_w estimates is negligible.

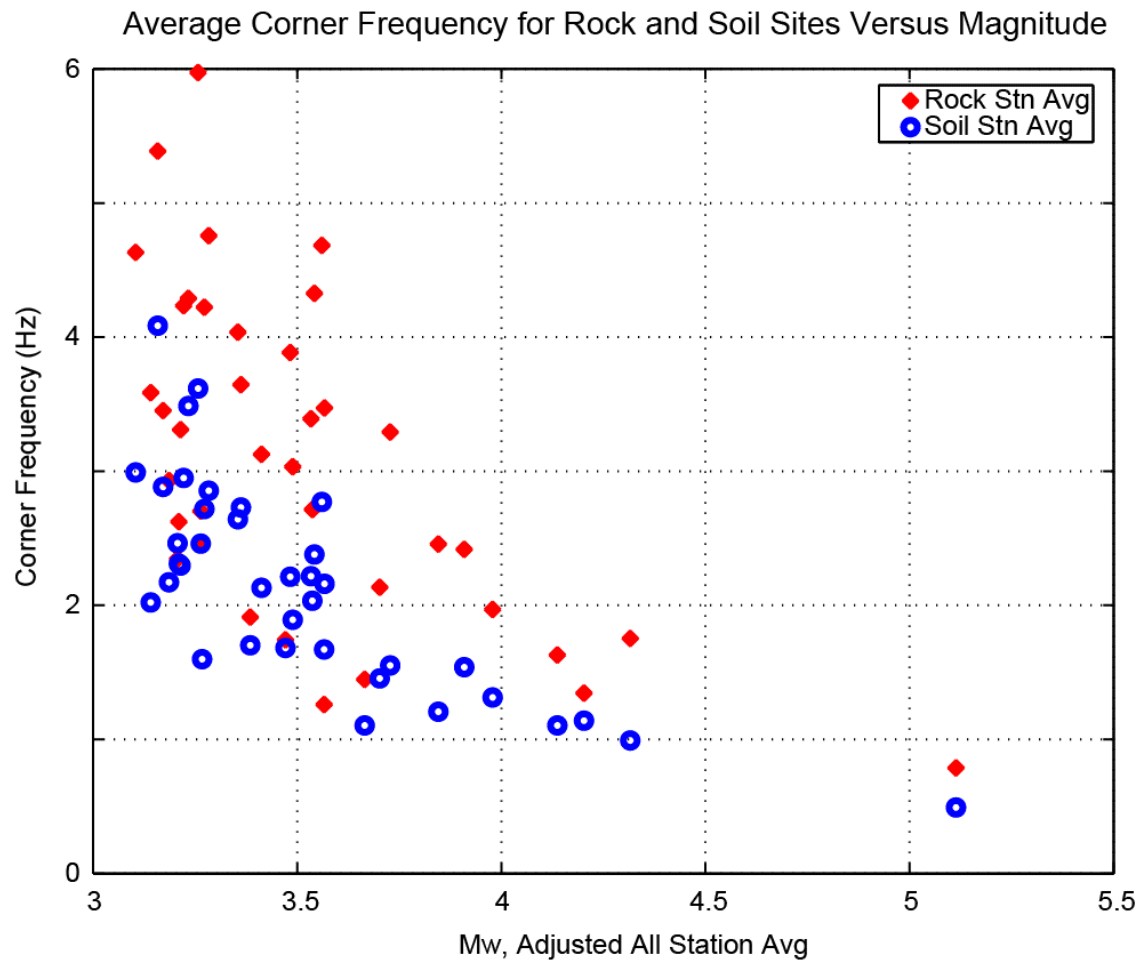


Figure 19. Corner frequency estimates are plotted for averaged soil and rock component averages. *Rock station averaged corner frequencies (red) are systematically larger than corresponding soil station averages (blue) because of site attenuation.*

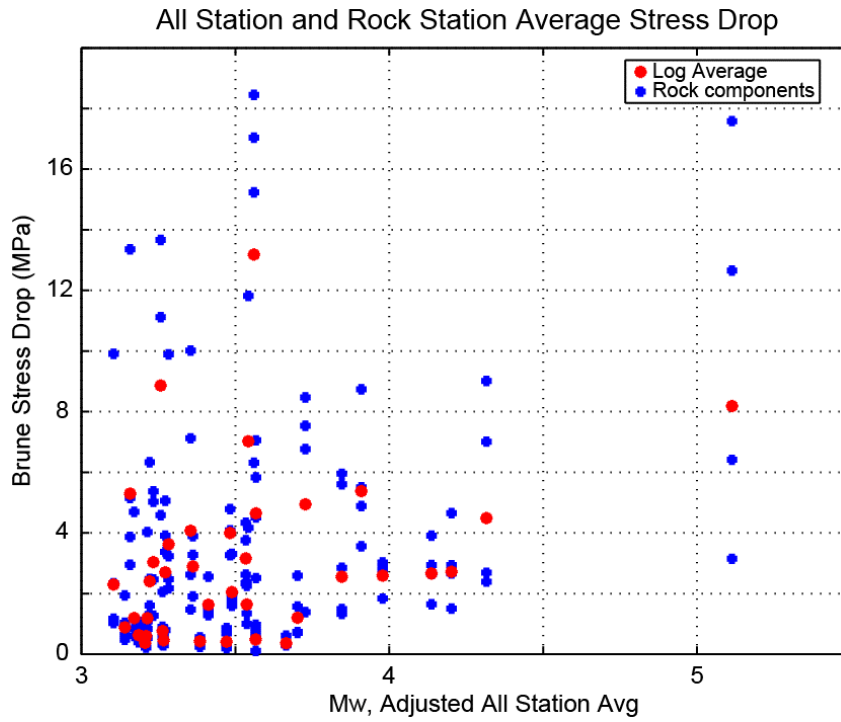


Figure 20. Brune stress drop (MPa) for rock site horizontal components (blue) are plotted versus M_w developed from all strong-motion stations. Component estimates are log-averaged to produce a more stable average stress drop estimate (red stars).

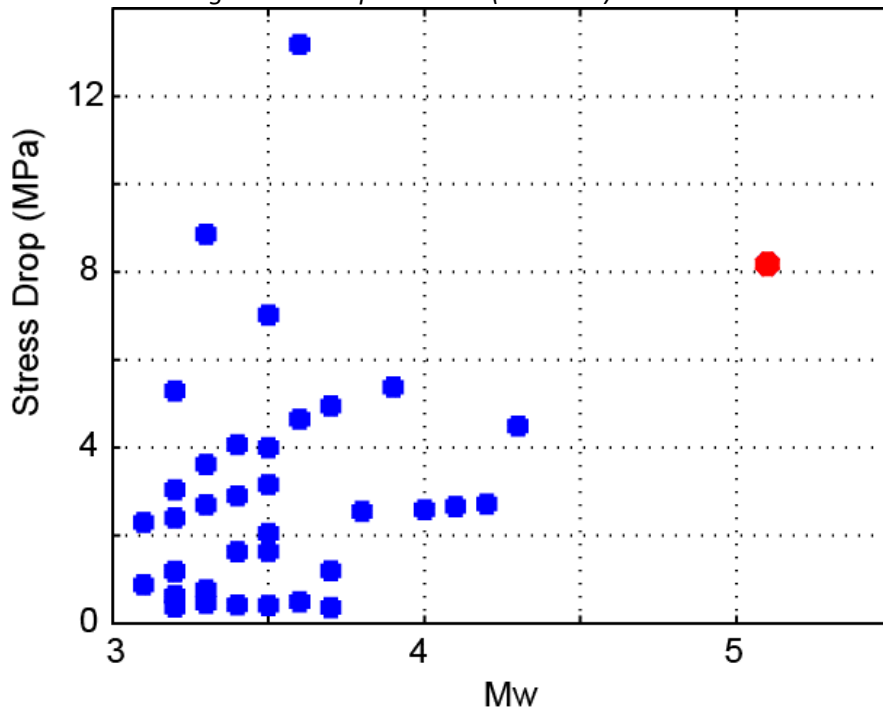


Figure 21. Final estimates for stress drop versus M_w for the Mogul M3+ event set. Values are given in Table 3.

Table 3. Source parameters for the Mogul sequence: moment magnitude (M_w), local magnitude (M_L), corner frequency (f_c) and stress drop developed using only the log-averaged rock component averages.

Date	Time (GMT)	M_w	M_L	M_0 (N-m)	f_c	Stress drop (MPa)
3/08/2008	10:07:00.330	3.3	3.2	1.06e+14	4.76	3.62
3/24/2008	19:16:14.220	3.1	2.8	6.48e+13	3.59	0.88
3/27/2008	03:42:14.290	3.3	3.1	1.00e+14	2.46	0.46
4/15/2008	14:59:37.350	3.5	3.4	2.52e+14	3.39	3.16
4/15/2008	21:26:35.280	3.2	3.0	7.56e+13	2.93	0.63
4/15/2008	21:32:31.780	3.7	3.4	4.50e+14	2.13	1.20
4/15/2008	21:33:57.640	3.5	3.5	2.16e+14	3.03	2.05
4/21/2008	19:14:10.440	3.2	3.0	8.23e+13	2.62	0.60
4/24/2008	22:47:04.200	4.0	3.8	1.17e+15	1.97	2.59
4/24/2008	22:55:49.020	4.3	4.2	3.75e+15	1.75	4.49
4/25/2008	01:00:33.460	3.3	3.1	9.68e+13	5.97	8.86
4/25/2008	17:30:10.080	3.3	3.2	1.02e+14	4.22	2.70
4/26/2008	01:13:20.910	3.7	3.5	4.92e+14	3.29	4.95
4/26/2008	06:39:59.720	3.6	3.2	2.81e+14	1.26	0.49
4/26/2008	06:40:10.590	5.1	4.8	5.91e+16	0.79	8.18
4/26/2008	06:43:50.800	3.5	3.4	2.54e+14	2.71	1.64
4/26/2008	07:29:20.120	3.6	3.4	2.76e+14	4.68	13.18
4/26/2008	09:11:59.820	3.5	3.3	2.59e+14	4.33	7.02
4/26/2008	14:35:29.190	3.1	2.8	5.70e+13	4.63	2.30
4/26/2008	14:47:37.300	3.2	3.1	8.92e+13	4.29	3.04
4/26/2008	15:20:40.490	3.5	3.4	2.11e+14	3.88	4.00
4/27/2008	17:49:49.820	3.4	3.3	1.35e+14	4.04	4.07
4/27/2008	18:31:10.600	3.4	3.0	1.39e+14	3.64	2.90
4/28/2008	11:33:18.210	4.1	4.1	2.02e+15	1.63	2.66
4/28/2008	12:12:31.230	3.2	2.9	8.14e+13	2.34	0.37
4/29/2008	05:51:05.530	3.2	3.0	6.88e+13	5.39	5.29
4/29/2008	06:01:53.580	3.4	3.0	1.66e+14	3.13	1.63
4/29/2008	16:14:59.850	3.5	3.0	2.03e+14	1.74	0.41
5/08/2008	05:55:01.600	3.9	3.6	9.21e+14	2.42	5.38
5/15/2008	13:44:48.430	3.6	3.3	2.82e+14	3.47	4.65
5/31/2008	09:09:56.830	3.2	3.0	7.20e+13	3.45	1.19
6/08/2008	10:13:58.620	3.4	3.0	1.51e+14	1.91	0.42
6/08/2008	17:53:40.640	3.8	3.6	7.39e+14	2.46	2.55
6/08/2008	17:55:19.360	4.2	3.9	2.54e+15	1.35	2.72
6/10/2008	00:18:34.910	3.2	2.8	8.35e+13	3.31	1.18
6/17/2008	14:01:49.190	3.3	3.0	9.90e+13	2.70	0.77
7/29/2008	10:34:42.110	3.7	3.2	3.96e+14	1.45	0.36
11/13/2008	07:42:08.480	3.2	3.0	8.56e+13	4.24	2.40

4.2.2 Investigation of Source Scaling of the Mogul Sequence

4.2.2.1 Probing the 2008 Mogul, Nevada, Earthquake Using Empirical Green's Functions

INTRODUCTION

Shallow earthquakes (< 4 km deep) are interesting for several reasons. They provide opportunities to explore source physics in a higher frequency range than is normally possible, due to the potential proximity of instrumentation. They occur in regions of low lithostatic stress, so thus the distribution of stress drop may be bounded at relatively small values. Their proximity to the surface can cause large ground motions, of interest to seismic hazards. Finally, their occurrence at depths accessible to drilling and mining activities make the difference between these events and explosions of particular interest for nuclear discrimination.

The shallow 2008 Mogul, Nevada, earthquake occurred as a part of a cluster of events lasting several months (Smith et al, 2008). This cluster was recorded by a dense array, including four IRIS RAMP instruments that were in place within one kilometer of the causative fault for the largest event, with $M_w 5.0$, on April 26, 2012 at 06:40 UTC. von Seggern et al (2014) relocated events in the cluster with $M_L \geq 1$. Strong motions recorded in this mainshock are described by Anderson et al. (2009). Our relocation of the largest earthquake places the hypocenter 2.7 km below the surface. The foreshocks and aftershocks in this cluster are mostly located between 1 and 5 km below the surface. The close-distance recordings and shallow events offer the opportunity to investigate the source processes of this event with a high resolution.

DATA

Figure 16 shows a map with aftershock locations and locations of stations used in this study. This study uses relocated earthquakes. The four near-distance stations (HONJ, MOGE, MOGL, MOGW) are RAMP stations. Five additional RAMP stations were installed after the April 26 mainshock. (At the time it was unclear that would be the mainshock).

The main shock occurred after a sequence of foreshocks initiated on February 29, 56 days before the main shock (Figures 2 and 3). The triangular-shaped bounds for the spatial extent of these events initially expanded upwards at about 20 m/day, downwards at about 40 m/day, to the northwest (positive strike) at about 30 m/day, and to the southeast at about 60 m/day. The horizontal and vertical extent of the area affected increased in the day before the largest event. The vertical extent of the active area extended from about 1.3 - 4.3 km depth, and the horizontal extent was from -1.5 to +2.0 km along strike, measured from the hypocenter. After the main shock, the aftershock extent immediately increased to the distance range from -2.0 to +2.6 km, and the depth range increased slightly to the range from 0.9 to 4.3 km.

Alternate models of the main shock focal mechanism based on seismic moment tensor inversion were given by Anderson et al. (2009). Within the range of models, and consistent with the aftershock distribution, the fault model adopted for this study had the parameters given in Table 4. Figure 22 shows two cross sections of earthquakes in the 24 hours after the April 26 mainshock. Figure 22 shows the fit of this plane to the aftershocks. The spatial aftershock extent described in Table 4 and shown in Figure 22 is reasonably considered an upper bound on the extent of rupture in the main shock.

As shown above, the station SKYF (Figure 16) is located nearly along strike of the active fault structure. Arrival times of relocated aftershocks at SKYF provide a profile allowing estimation of the seismic velocity in the source region, i.e. at depths of 2-4 km. Our result is that the P-velocity is $\alpha=5.13\pm0.18$ km/s, and the S-velocity is $\beta=2.87\pm0.22$ km/s. Based on the relationships of both P- and S-velocity with density (Ludwig et al, 1970; reproduced in Lowrie, 2007, p81) $\rho = 2.6\pm0.1$ gm/cm³, implying that the shear modulus in the source region is $\mu=2.1\text{e}11$ dyne/cm².

METHOD

The contribution of the wave propagation from a point fault to the site of interest (the Green's function) is needed to understand the contribution from the source, i.e. the slip on the fault. The mathematical framework for this study is the representation theorem. Using the notation of Aki and Richards (2002), the representation theorem is expressed as:

$$u_n(\vec{x}, t) = \int_{-\infty}^{\infty} d\tau \iint_{\Sigma} \left[u_i(\vec{\xi}, \tau) \right] c_{ijpq} v_j \frac{\partial G_{np}(\vec{x}, t - \tau; \vec{\xi}, 0)}{\partial \xi_q} d\Sigma \quad (5)$$

In this equation, $u_n(\vec{x}, t)$ gives the n^{th} component of the displacement of the ground at an arbitrary location \vec{x} and at time t . The vector \vec{v} is normal to the fault, and the positive direction of the normal defines the positive side of the fault for defining the slip discontinuity. The i^{th} component of the discontinuity in the slip across the fault is given by $[u_i(\vec{\xi}, \tau)] = u_i^+(\vec{\xi}, \tau) - u_i^-(\vec{\xi}, \tau)$ where $\vec{\xi}$ represents a location on the fault surface Σ and τ is the time that this discontinuity occurs. The Green's function is given by $G_{np}(\vec{x}, t; \vec{\xi}, \tau)$. This gives the displacement in the n direction at location \vec{x} and time t caused by an impulsive point force acting in the p direction at location $\vec{\xi}$ and time τ . Finally, c_{ijpq} gives the elastic constants of the medium. For an isotropic medium, $c_{ijpq} = \lambda \delta_{ij} \delta_{pq} + \mu (\delta_{ip} \delta_{jq} + \delta_{iq} \delta_{jp})$, where λ and μ are the Lamé constants and δ_{ij} is the Kronecker delta, equal to 1 when $i=j$ and zero otherwise.

Equation 5 represents the ground motion at the site as the linear combination, through the integral over space, of the contributions from each point on the fault surface. The convolution over time incorporates the effect of the rupture at each point taking a finite amount of time to reach its final value. Through the representation theorem, the problem of predicting ground motions requires specification of the offset on the fault as a function of location and time, which incorporates earthquake source physics, and a specification of the Green's function, which incorporates wave propagation. Conversely, a model for the wave propagation is required to infer the slip function given observed ground motions. Because the wave propagation is through rather complex media, this study uses empirical Green's Functions to try to understand the slip on the fault.

As pointed out by Hartzell (1978) and Kanamori (1979), seismograms from a small earthquake give the wave propagation between the source and the station for an impulsive fault slip, and are for that reason designated as empirical Green's functions (EGFs). EGFs have been used for many purposes. In the frequency domain, they enable good estimates of the corner frequencies of larger events, and consequent evaluations of source scaling relations (e.g. Shearer et al., 2006). In the time domain, EGFs can be deconvolved from seismograms of larger earthquakes to determine the source time function of the larger earthquake (e.g. Mori and Frankel, 1990; Xie et al., 1991; Abercrombie and Mori, 1994). This process can be reversed to use EGFs to model main shock seismograms (e.g. Hartzell, 1978; Fukuyama and Irikura, 1986) or to match or predict statistical characteristics of large earthquakes (e.g. Hutchings, 1994). EGFs can also be used to invert for the slip time function on a finite fault (e.g. Sadeghi et al., 2012; Hartzell et al., 2013; Sun and Hartzell, 2014).

A small-event seismogram is not strictly a Green's function, since the focal mechanism is included and the rise time of the small event may have some effect, but it is called an empirical Green's function (EGF). The relationship between the seismogram from a small earthquake and a Green's function is explained in the context of Equation 5.

We begin by visualizing that the fault to be modeled is discretized into K elements ($k=1,2,...,K$) of equal area, designated as $\delta\Sigma_k$. A small earthquake in element k , with moment M_{0k}^{EGF} , is to be used as an empirical Green's function to extract the wave propagation effect. The actual fault dimension (D) of this small earthquake might be estimated from its corner frequency. However, because the EGF will represent an area of size $\delta\Sigma_k$, and considering the definition of the seismic moment ($M_0 = \mu AD$), the

elemental slip of this event as $\delta u_k^{EGF} = \frac{M_{0k}^{EGF}}{\mu \delta\Sigma_k}$. In the context of Equation 5, the slip discontinuity is a

vector with components $[\delta u_{ki}]$ for $i=1,2,3$. The magnitude of this vector is $|\delta u_k| = \left(\sum_{i=1}^3 \delta u_{ki}^2 \right)^{\frac{1}{2}}$. The approximation used for empirical Green's function analysis assumes that the small event is a good approximation for a point source, at location $\vec{\xi}_k$ and at time τ_k , with an impulsive time function, so we substitute $[u_i(\vec{\xi}, \tau)] = [\delta u_{ki}] \delta(\tau - \tau_k) \delta(\vec{\xi} - \vec{\xi}_k)$ into Equation 5, to obtain:

$$u_n^{EGF-k}(\vec{x}, t) = [\delta u_{ki}] c_{ijpq} v_j \frac{\partial G_{np}(\vec{x}, t - \tau_k; \vec{\xi}_k, 0)}{\partial \xi_q} \delta\Sigma = u_n^{EGF-k}(\vec{x}, t - \tau_k; \vec{\xi}_k) \quad (6)$$

To derive the proper way to use the EGF, one simply substitutes Equation 6 back into Equation 5. The substitution is valid with certain assumptions. The first is that the EGF has the same focal mechanism as the earthquake to be modeled. Under this assumption, the normal vector \vec{v} is the same and the direction of the dislocation vector $[\delta \vec{u}_k]$ is the same, so all the terms in the sums in Equation 5 and Equation 6 contribute with the same proportions. The second is that the EGF has a corner frequency

higher than any frequency of interest. A third assumption is that the medium and hence the Green's function does not change with time so that τ_k can be replaced with a general time τ . Then:

$$u_n(\vec{x}, t) = \sum_{j=1}^{J_k} \sum_{k=1}^K \frac{[u_k(\vec{\xi}, \tau_j)]}{\delta u_k^{EGF}} u_n^{EGF-k}(\vec{x}, t - \tau_j, \vec{\xi}) \quad (7)$$

The integrations in Equation 5 have been approximated by a sum over all the fault elements (k), and for each fault element, a sum over the contributions at different times. The term $[u_k(\vec{\xi}, \tau_j)]$ represents the slip that takes place in fault element k (located at fault coordinate $\vec{\xi}$, at time τ_j . At this point it is more intuitive to switch the order of operations, and write the equation so that the discretized representation of the convolution is carried out first. Equation 7 becomes:

$$u_n(\vec{x}, t) = \sum_{k=1}^K \frac{\sum_{j=1}^{J_k} [u_k(\vec{\xi}, \tau_j)] u_n^{EGF-k}(\vec{x}, t - \tau_j, \vec{\xi})}{\delta u_k^{EGF}} \quad (8)$$

Multiplying both the numerator and denominator in Equation 8 by $\mu \delta \Sigma$, Equation 7 becomes:

$$u_n(\vec{x}, t) = \sum_{k=1}^K \frac{\sum_{j=1}^{J_k} M_{0k}(\vec{\xi}, \tau_j) u_n^{EGF-k}(\vec{x}, t - \tau_j, \vec{\xi})}{M_{0k}^{EGF}} \quad (9)$$

where $M_{0k}(\vec{\xi}, \tau)$ is the total seismic moment that has been released in element k of the fault at time τ during the rupture of the large event. The convolution, in Equation 9, of the empirical Green's function with a function of finite duration for each element of the fault is an essential step, as the simple summation of empirical Green's functions cannot match large earthquake spectra over a broad bandwidth. This problem is discussed more fully in a later section.

As will be subsequently shown, the source dimension for the mainshock is only 1-2 km across. The corner frequency is in the 1-3 Hz range. Thus to resolve details of the source, Green's functions need to be reliable at frequencies above 3 Hz. The recorded empirical Green's functions were compared with synthetic seismograms for existing layered velocity models for all stations, with the conclusion that layered velocity models to generate Green's functions are not satisfactory after low-pass filtering even with a filter frequency of 2 Hz. Thus, synthetic Green's functions for a layered model were not used.

5. Inversion Using the Empirical Green's Functions

Initially, we investigated the use of EGFs as described in Equation 9. We identified 25 events with $M_L > 2.4$ located within 500 m of the fault plane, from among the events occurring within 24 hours of the time of the main shock (events before and after were included). Locations of these events projected onto the fault are shown in Figure 23.

The inversion was set up using linear algebra in the form

$$Gm=d \quad (10)$$

where G represents the contribution of each empirical Green's function, d is the data, and m is the unknown slip model. The unknown model m for an EGF consists of the incremental moments released at the location of that EGF in M time intervals of duration dt . Thus the times that are represented are $t_m=[0,dt,2dt,...,kdt,...,(M-1)dt]$. In G , the i^{th} EGF is repeated M times (M consecutive columns giving the amplitudes \mathcal{G}_k^i , the amplitude of the i^{th} EGF at time kdt). The duration of the Green's function can be longer than the source duration; in general it is sampled at $N+1$ time intervals of duration dt . Since each EGF has three components, the components are essentially stacked consecutively in the columns of G . In equations:

$$G = \begin{bmatrix} g_0^{1E} & 0 & 0 & 0 & \dots & g_0^{2E} & 0 & 0 & 0 & \dots \\ g_{dt}^{1E} & g_0^{1E} & 0 & 0 & \dots & g_{dt}^{2E} & g_0^{2E} & 0 & 0 & \dots \\ g_{2dt}^{1E} & g_{dt}^{1E} & g_0^{1E} & 0 & \dots & g_{2dt}^{2E} & g_{dt}^{2E} & g_0^{2E} & 0 & \dots \\ g_{3dt}^{1E} & g_{2dt}^{1E} & g_{dt}^{1E} & g_0^{1E} & \dots & g_{3dt}^{2E} & g_{2dt}^{2E} & g_{dt}^{2E} & g_0^{2E} & \dots \\ g_{4dt}^{1E} & g_{3dt}^{1E} & g_{2dt}^{1E} & g_{dt}^{1E} & \dots & g_{4dt}^{2E} & g_{3dt}^{2E} & g_{2dt}^{2E} & g_{dt}^{2E} & \dots \\ \vdots & \vdots & \vdots & \vdots & \ddots & \vdots & \vdots & \vdots & \vdots & \ddots \\ g_{Ndt}^{1E} & g_{(N-1)dt}^{1E} & g_{(N-2)dt}^{1E} & g_{(N-3)dt}^{1E} & \dots & g_{Ndt}^{1E} & g_{(N-1)dt}^{1E} & g_{(N-2)dt}^{1E} & g_{(N-3)dt}^{1E} & \dots \\ g_0^{1N} & 0 & 0 & 0 & \dots & g_0^{2N} & 0 & 0 & 0 & \dots \\ g_{dt}^{1N} & g_0^{1N} & 0 & 0 & \dots & g_{dt}^{2N} & g_0^{2N} & 0 & 0 & \dots \\ g_{2dt}^{1N} & g_{dt}^{1N} & g_0^{1N} & 0 & \dots & g_{2dt}^{2N} & g_{dt}^{2N} & g_0^{2N} & 0 & \dots \\ g_{3dt}^{1N} & g_{2dt}^{1N} & g_{dt}^{1N} & g_0^{1N} & \dots & g_{3dt}^{2N} & g_{2dt}^{2N} & g_{dt}^{2N} & g_0^{2N} & \dots \\ g_{4dt}^{1N} & g_{3dt}^{1N} & g_{2dt}^{1N} & g_{dt}^{1N} & \dots & g_{4dt}^{2N} & g_{3dt}^{2N} & g_{2dt}^{2N} & g_{dt}^{2N} & \dots \\ \vdots & \vdots & \vdots & \vdots & \ddots & \vdots & \vdots & \vdots & \vdots & \ddots \\ g_{Ndt}^{1N} & g_{(N-1)dt}^{1N} & g_{(N-2)dt}^{1N} & g_{(N-3)dt}^{1N} & \dots & g_{Ndt}^{1N} & g_{(N-1)dt}^{1N} & g_{(N-2)dt}^{1N} & g_{(N-3)dt}^{1N} & \dots \\ g_0^{1Z} & 0 & 0 & 0 & \dots & g_0^{2Z} & 0 & 0 & 0 & \dots \\ g_{dt}^{1Z} & g_0^{1Z} & 0 & 0 & \dots & g_{dt}^{2Z} & g_0^{2Z} & 0 & 0 & \dots \\ g_{2dt}^{1Z} & g_{dt}^{1Z} & g_0^{1Z} & 0 & \dots & g_{2dt}^{2Z} & g_{dt}^{2Z} & g_0^{2Z} & 0 & \dots \\ g_{3dt}^{1Z} & g_{2dt}^{1Z} & g_{dt}^{1Z} & g_0^{1Z} & \dots & g_{3dt}^{2Z} & g_{2dt}^{2Z} & g_{dt}^{2Z} & g_0^{2Z} & \dots \\ g_{4dt}^{1Z} & g_{3dt}^{1Z} & g_{2dt}^{1Z} & g_{dt}^{1Z} & \dots & g_{4dt}^{2Z} & g_{3dt}^{2Z} & g_{2dt}^{2Z} & g_{dt}^{2Z} & \dots \\ \vdots & \vdots & \vdots & \vdots & \ddots & \vdots & \vdots & \vdots & \vdots & \ddots \\ g_{Ndt}^{1Z} & g_{(N-1)dt}^{1Z} & g_{(N-2)dt}^{1Z} & g_{(N-3)dt}^{1Z} & \dots & g_{Ndt}^{1Z} & g_{(N-1)dt}^{1Z} & g_{(N-2)dt}^{1Z} & g_{(N-3)dt}^{1Z} & \dots \end{bmatrix} \quad (1) \quad (11)$$

The superscripts E , N , and Z in Equation 11 represent the east, north, and vertical motions. Stacking the three components like this is appropriate since they are all excited by the same source. Let u represent the observed strong motion seismogram that is to be modeled using the sum of EGFs in Equation 8. Then the data vector is:

$$d = \begin{bmatrix} u_0^E \\ u_{dt}^E \\ u_{2dt}^E \\ u_{3dt}^E \\ u_{4dt}^E \\ \vdots \\ u_{Ndt}^E \\ u_0^N \\ u_{dt}^N \\ u_{2dt}^N \\ u_{3dt}^N \\ u_{4dt}^N \\ \vdots \\ u_{Ndt}^N \\ u_0^Z \\ u_{dt}^Z \\ u_{2dt}^Z \\ u_{3dt}^Z \\ u_{4dt}^Z \\ \vdots \\ u_{Ndt}^Z \end{bmatrix} \quad (12)$$

Different approaches to the solution of Equation 10 were explored. The most successful was possibly the simplest: to use a singular value decomposition of G , and retain only a very small number of eigenvalues and eigenvectors to obtain its generalized inverse matrix H . The solution $m=Hd$ obtained in this way has negative values, which would represent back-slip on the fault. We simply replaced all negative values with zero. In investigations of the number of eigenvalues to keep, we monitored the difference between the model including negative values (i.e. with backslip) and without it. For most stations these two solutions had small differences for the largest eigenvalues of the *SVD*, and only diverged later. An example is shown in Figure 24. A non-negative least squares inversion for m closely resembled the SVD approach for all of the applications where this alternate approach was tested.

The sample interval was intentionally chosen considering the size of the problem. First, we note that, when two identical pulses are added with a lag time, then if the lag time is small enough the pulses can add to give a smooth, flat shape. For a sinusoidal wave with period T , a lag time of $\tau_1 = T/10$ is about right to achieve this. The highest frequency considered in our inversion is 3 Hz, which thus requires a lag time, i.e. a sample interval, of $\tau_1 = dt \cong 0.03s$. Using the SVD, there is no penalty for using small values of dt , except for increased computer time. We also consider a fault represented by a grid spacing of distance dl . Adjacent points rupturing in a propagating rupture will be lagged by time $\tau_2 = dl/c$, where

c = rupture velocity. For a rupture speed of $c=3$ km/s, events on the fault with spacing of 100 m would have this lag time. For 3 Hz wave in a medium with shear velocity of about 3 km/s, the wavelength is 1 km. Thus adjacent events at 100 m spacing would not be uniquely resolvable, but that level of sampling would assure that aliasing does not occur. With EGFs, this point is moot, however, as the spatial sampling depends on the distribution of suitable aftershocks.

RESULTS

The first inversion used the full set of 25 EGFs to model the main shock. An independent, single-station inversion was performed for each of the 11 stations on Figure 16. Figure 23 shows the relative magnitude of the contributions of each of the EGFs for the inversion using station HONJ. Symbol sizes in Figure 23 are proportional to the log of the total moment contributed by each EGF. As noted in the caption, several of the EGFs do not make a significant contribution to models of the seismograms. From southeast to northwest, the EGFs that contribute strongly are EGFs 20, 19, 24, 7, 5, 12, 6, 25, and 21. The EGFs at the bottom of the fault that do not contribute significantly (EGF 11, 10, 22, 26, and 15) are taken as evidence that the rupture only proceeded down-dip by about 0.6-0.7 km. The minor contribution from EGFs 3, 4, 9, 13, 23, and 17 would seem to indicate that the rupture did not proceed significantly more than about 0.6 km to the northwest, with perhaps an irregular rupture front suggested by the shallow aftershock EGF 25. The noticeable contribution for EGF 21, 2.7 km northwest of the hypocenter, is somewhat problematical. For the P-wave velocity in the hypocentral region, the P-wave from the hypocenter would reach this location 0.53 seconds after the earthquake origin time, and the S-wave would arrive at 0.94 seconds. However, the inversion finds its time function starting much sooner. We will return to this problem subsequently.

The second inversions used a set of the ten largest EGFs contributors, including EGF21, in spite of our skepticism about the reality of its contribution. In these cases, the inversions are still carried out on a station by station basis. For this case, we executed many more trial inversions, including every number of eigenvalues from 1 to 15, plus 20, 25, 30, 35, and 40 eigenvalues, for each station. The inferred source time functions for each case were reviewed, looking for consistency among the inferences based on each station. We found that EGFs 20 (at the southeast end of rupture), 8 (at the base of the rupture), and 21 (at the northwest end of the rupture) showed very little consistency in this sense. As an example of the effect, Figure 25 compares the source time functions of EGF 7 and 21. The source functions for EGF7 mostly indicate a strong source pulse between 0.5-0.9 seconds into the rupture, with some of the sources suggesting a smaller pulse from this location earlier. The source functions for EGF21 do not show a coherent pattern. There is a certain amount of judgment in this conclusion, since the shape of the source function does change based on the number of eigenvalues. Thus it was important to look at the solutions for varying numbers of eigenvalues. For most stations the shape of the source function varies as the number of retained eigenvalues varies, but the overall pattern is relatively stable. If any patterns did appear for EGF 8, 20, or 21, they did not show the same stability. For that reason we concluded that these three contributions were essentially fitting noise in the system. To prevent contamination with noise from EGF 8, 20, and 21, the final calculations used a seven EGF set: EGF 2, 5, 7, 12, 19, 24, and 25.

The locations of remaining hypocenters in the 7 EGF set (Figure 23) indicate that the main shock rupture extended about 0.5 km northwest from the hypocenter (EGF2), and about 1.0 km to the southeast (EGF19, but not EGF20). To the extent that there is directivity, that would be expected more to the southeast. The vertical extent of rupture seems to be predominantly within 0.5 km above and below the main shock hypocenter. Depths shallower than 0.5 km above the hypocenter are poorly sampled with only one large aftershock in this set of EGFs. EGF 25 is the most marginal of the EGF's retained at this stage.

Figure 26 shows fits of the seismograms in the final inversion of the seven EGF set. From these it can be seen that the seismograms are modeled reasonably well using the EGFs.

One would hope that the time functions inferred for the slip from each of the EGFs would be identical, since the radiation to each of the separate stations originates from the same fault. For EGF7 in Figure 25, the source time functions estimated from the 11 stations peak at different times and have differing shapes. Further analysis was not done on the estimates shown in Figure 25, but rather on source time functions (STFs) estimated from the 7 EGF inversion set. Figure 27 shows those time functions plotted roughly by station azimuth, for EGF 2, 5, and 7, which contribute the majority of the seismic moment at most stations. Focusing on EGF 2 (Figure 27A), one sees that the main pulse is estimated to come later than the average at stations MOGE, MOGL, HONJ and MOGW, but earlier at stations NOAA, RFNV, RENO, UNRN, RF05, and WGLF. One possible explanation for this result is that the spatial location of the centroid of the EGF is not collocated with the centroid of the slip that it is representing on the fault. For instance, this EGF is located 145 m west of the estimated fault location used for Figures 16 and 21. If the centroid of the represented slip were at this nearest point on the fault, east of the EGF hypocenter, the method of finding the slip function would advance or delay the source function for stations depending on the difference in the centroid distances.

We experimented with adjustments to the EGF centroids to account for this effect, based on the differences in the times of peaks in the source time functions. The adjustments resulted in minor reduction in the variability of the source functions when determined independently at each station. But qualitatively the source functions were quite similar to the unadjusted results. Therefore, we concluded that the source time functions obtained from the stations on Figure 16 is approaching the limit of the resolution of these data.

Figure 28 shows the average source time functions determined for the seven EGFs. These are found using seismograms filtered at 2 Hz. This provides evidence of an interesting, and complex rupture process. The first significant peak in the moment rate time series is seen on EGF12 at 0.03s, offset slightly northwest and downdip from the hypocenter. This is followed by roughly simultaneous slip detected by EGF5 peaking at 0.15 s and EGF2 peaking at 0.12s, with the slip at EGF2 being greater. The next relatively large peak is at EGF7 at 0.22s. Together, this sequence, which lasts about 0.3 seconds, indicates rupture propagating updip and towards the southeast.

The moment rate at EGF2 does not return to zero after its first peak, and this apparently reactivates EGF12 at about 0.3 s, which in turn reaches a second peak at 0.4s. This in turn seems to reactivate EGF 5

to radiate a stronger pulse than its first one, peaking at 0.55s. The interaction with the part of the fault represented by EGF12 also seems to release EGF2 and EGF7 to slip again. It is in this second slip episode that EGF2 radiates the strongest pulse in the earthquake, peaking at 0.66s.

The contribution from EGF24, the deepest of the EGFs, is a slightly longer period pulse than the other EGF pulses, and starts roughly as the first pulse at EGF5 ends. One might speculate that this slight difference is caused by some differences in the fault properties at the bottom of the rupture. The contribution from EGF25, the shallowest, seems to essentially follow the slip at EGF2 that is almost directly below, but with a smaller amplitude, as might be expected for a location near the top edge of the rupture.

In summary, these time functions are consistent with a source slip function in which locations of slip are interacting, and resulting in one part of the fault (sampled by EGF 5 and 12) stopping and restarting the rupture progresses. Lee et al. (2011) have previously suggested repeating rupture of parts of the fault that caused the 2011 Tohoku, Japan earthquake (M_w 9.1). Uchide et al. (2013) suggested repeating rupture of the same part of the causative fault in the 2010 El Mayor-Cucapah earthquake (M_w 7.2). Gabriel et al (2012) describe a rupture dynamic model that can predict this type of behavior, and cite other examples where it may have been observed. Figure 28 suggests that a repeated rupture is possible on a much smaller scale.

The majority of the contribution in the source model from these inversions comes from EGFs centered within 0.6 km of the hypocenter. The contribution from EGF 2 is dominant, indicating that the majority of the slip was from a part of the fault that is shallower than the hypocenter (Fig 4). The contributions from EGF7 above the hypocenter, and EGF 5 and EGF12 below the hypocenter are similar in magnitude, so the 0.5 km below the hypocenter was also an important contributor.

The empirical Green's functions inversion implies that the dimension of rupture in the main shock was smaller than the extent of aftershocks in Figure 22. Considering that the hypocenter in Figure 22 is at the depth of 2.7 km, the aftershocks used here imply a depth range of 1.7 km to 3.4 km, and a lateral extent from -1.2 to +0.8 km along strike. As described on Figure 2 and 3, the aftershocks show a fault dimension 5 km long by 2 km wide. The inversions here find a fault dimension about 2 km in length and 1.7 km in vertical extent, for a rupture area of about 3.4 km². A fault radius of about 1.0 km would have the same fault area. This event is thus somewhat unusual in that the larger fault area was already mostly activated in the foreshock sequence, and the main shock apparently ruptured only a fraction of the activated fault.

For an earthquake with M_w 5.0, one expects that the source size will be potentially a few kilometers across. For instance, Kanamori and Anderson (1975) give the following relationship:

$$M_0 = \frac{16}{7} \Delta \tau_s r_E^3 \quad (13)$$

For $M_w 5.0$, the seismic moment is 4.0×10^{23} dyne-cm. For a typical $M_w=5.0$ earthquake with 3 MPa (30 bar) stress drop (Allman and Shearer, 2009), the expected source radius is 1.8 km. A source radius $r_E=1$ km corresponds to stress drop = 175 bars (17.5 MPa).

We note that mislocation errors of earthquake sequences which emanate from a given source area will always serve to enlarge the estimate of "fault area" somewhat. Also, there is the tendency for aftershock sequences to expand over time. Those mechanisms are not contributing significantly to the uncertainty here, however. The uncertainties in this case emanate from the limited distribution of aftershocks with magnitude sufficient to be used in the inversion, and the difference between the EGF locations and the locations of the slip that each EGF represents. However the brief duration of the seismograms themselves would argue that the energy in the main shock had to emanate from an area with the dimension not much larger than what was found here.

DISCUSSION

The source area of the Mogul earthquake was ~ 2 km along strike and somewhat smaller along dip. The greatest energy release was in the depth range of 2.0-3.2 km, with more energy released above the hypocenter (2.7 km) than below. Our estimate of the stress drop in this event was 17.5 MPa, which is a relatively high stress drop. For a crustal density of 2.6 gm/cm^3 , the lithostatic stress at 2 km is ~ 50 MPa (500 bars), and at 3.2 km it is ~ 80 MPa. If the hypocentral depth is taken as representative, the stress drop was about 25% of the lithostatic stress.

Bell et al (2012) found that the aseismic slip in this earthquake implies a seismic moment exceeding the seismic slip, indicating that this fault may have had essentially a complete stress drop during the sequence. The matches to the seismograms in Figure 27 tend to have smaller amplitude surface waves than the observations. This may be caused by not having enough EGFs, so that some part of the fault with significant slip is not contributing. This suggests that the probes are finding slip focused on a small part of the fault.

CONCLUSIONS

The approach used here to probe the slip function at different locations in the source may have more general applications. It differs from inversion using EGF as in Hartzell et al. (2013) and Sun and Hartzell (2014) in several significant ways. That approach aims to find slip at a grid of points on the fault. It does this by considering only a single phase in the EGF, and adjusting the arrival time of that phase in the inversion to match a model travel time from each of the grid of points. Several EGFs are used as available to represent different parts of the fault. Hartzell et al. (2013) also assume a uniform rupture velocity across the fault, and require that all of the slip at a point occur within a window around the

implied rupture time. The approach used here, instead, used the entire EGF, including P-waves, S-waves, and surface waves, and thus a single adjustment of different phases to different points on the fault is not possible. On the other hand, by retaining all three components of the entire seismogram, the approach used here is able to extract the slip representative of the part of the fault. Using the EGF as a probe thus makes no assumption about the character of the slip function, and thus if a part of the fault slips, stops, and then slips again much later, this is detectable.

This approach may be more difficult to apply for EGFs at greater distances than those used in this study. However, its application to probe the sources of strong ground motions in particular is worth future study.

DATA SOURCES

All data for this project was gathered by the Nevada Seismological Laboratory. It has been submitted to the IRIS Data Center. The strong motion records for the main shock are also available from the Center for Engineering Strong Motion Data (CESMD).

Table 4. Model of the Mogul mainshock used in this study.

Parameter	Value
Origin time	April 26, 2012, 06:40:10.59 UTC (April 25, 2012, 11:40:10.59 local time, PDT)
Hypocenter	39.5244° N, 119.9175° W, 2.763 km depth (Depth measured from local mean elevation, which is about 1.6 km above sea level.)
Fault orientation	Strike: 144°; Dip: 85°; Rake: 180°
24 Hour aftershock extent (see Figure 2) This is an upper bound on the fault size during the main shock.	Relative to the hypocenter: 2 km in + strike direction, 3 km in - strike direction 1 km updip, to 1.2 km downdip. Depths from 1.7 to 3.9 km

Table 5. Seismic stations used in this study. More information on these stations is available in Anderson et al. (2009).

Station	Lat.	Long.	Elev. (m)	Station Type ¹	Inst. Type
MOGL	39.52027	-119.93066	1463	IRIS RAMP	Episensor 200 Hz 10 V/g with Reftek 130 RAMP.
MOGE	39.5217	-119.9216	1440	IRIS RAMP	Episensor 200 Hz 10 V/g with Reftek 130 RAMP.
HONJ	39.5307	-119.9302	1563	IRIS RAMP	Episensor 200 Hz 10 V/g with Reftek 130 RAMP.
MOGW	39.5301	-119.9360	1584	IRIS RAMP	Episensor 200 Hz 10 V/g with Reftek 130 RAMP.
NOAA	39.5681	-119.7958	1490	USGS ANSS	Episensor-K2.
RENO	39.5391	-119.8138	1384	USGS	Episensor-Etna.
RF05	39.5095	-119.8360	1400	USGS ANSS	Episensor-K2.
RFMA	39.5188	-119.9010	1518	USGS ANSS	Episensor-Etna
RFNV	39.5742	-119.8275	1544	USGS ANSS	Episensor-Etna.
SKYF	39.4825	-119.8340	1552	USGS ANSS	Episensor-Etna.
UNRN	39.527	-119.818	1390	USGS ANSS	MEMS-RT130.
WGLF	39.4986	-119.8216	1413	USGS ANSS	MEMS-RT130.

Notes:

1 ANSS is Advanced National Seismic System; RAMP is Rapid Array Mobilization Program.

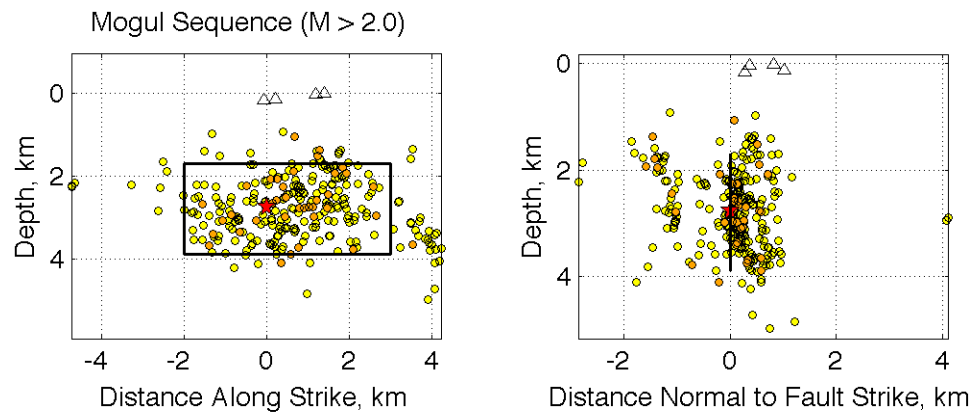


Figure 22. Cross sections of Mogul, Nevada source area. *Left shows hypocenters projected onto a fault with strike 328 and dip 86. The view is towards the southwest. The four nearest stations are shown projected into this plane.*

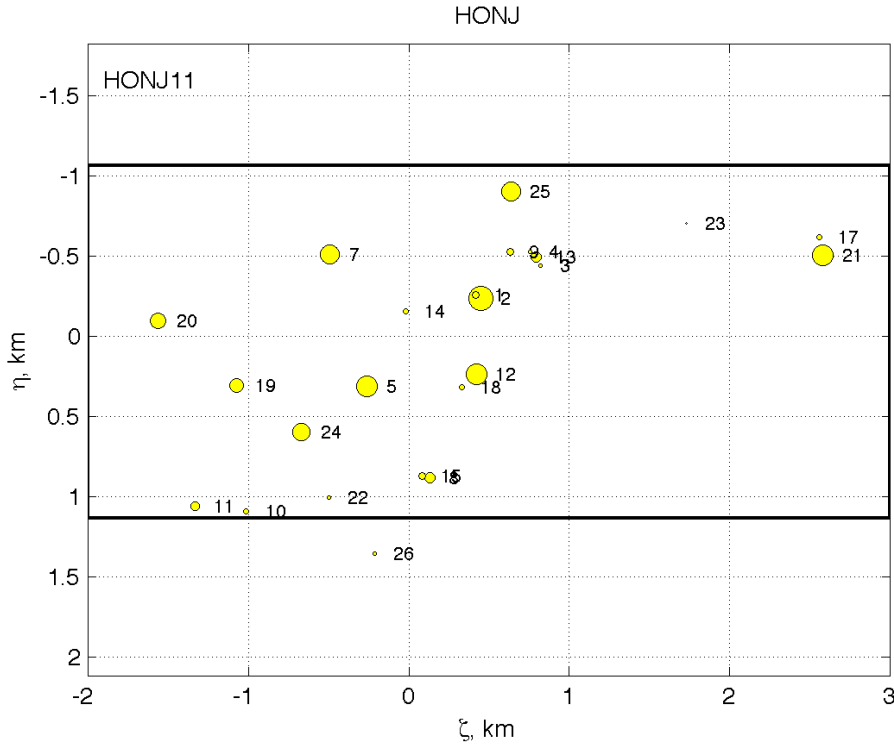


Figure 23. Locations of EGFs for initial inversion for the fault dislocation model. *The horizontal axis ζ increases in the positive strike direction, and the vertical axis η is measured along the inclined fault plane, which dips at 86 degrees in this model, and increases downdip. The origin ($\zeta=0$, $\eta=0$) is our location for the hypocenter. This perspective views the fault from the northeast, thus northwest is on the right. The symbol sizes are proportional to the contribution for fault slip using the EGFs. Symbol radius is proportional to the log of the moment contribution, so the contribution from all EGF locations with symbols noticeably smaller than the largest are in the noise.*

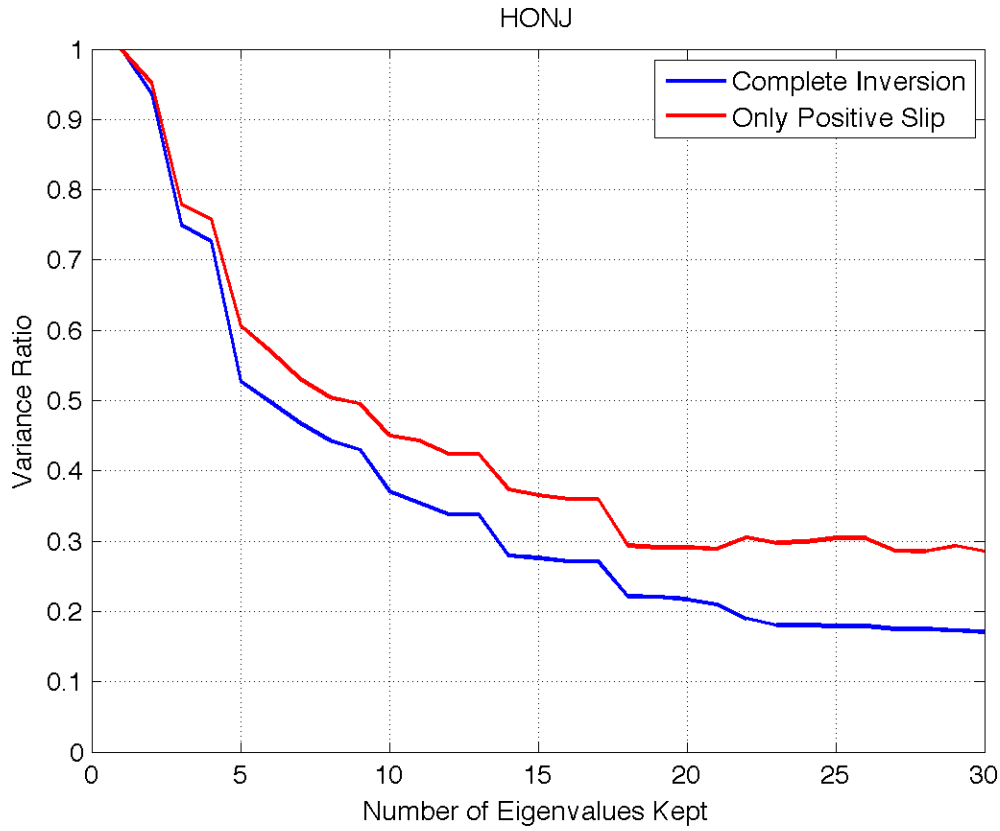


Figure 24. Quality of fit of the strong motion records at station HONJ, as a function of the number of eigenvalues kept from the singular-value decomposition of the matrix G . The variance ratio is the ratio of the variance of the misfit of the model to the variance of the data $(\sum (d_i - \hat{d}_i)^2 / \sum d_i^2)$.

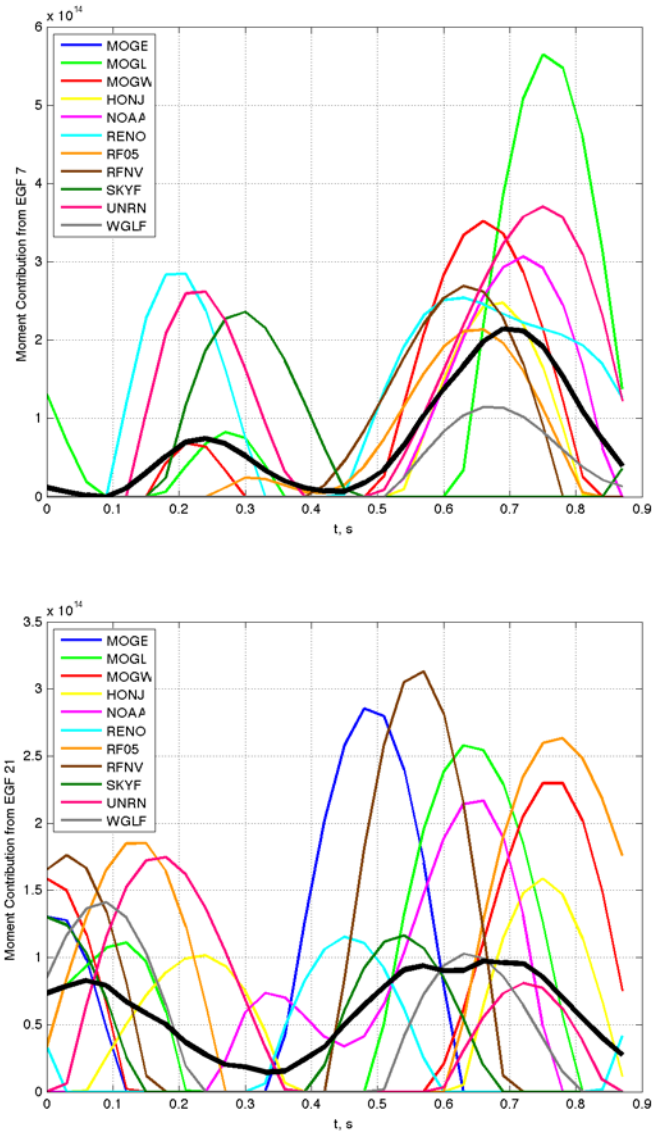


Figure 25. Comparison of source functions for two EGFs, EGF 7 and EGF 21, in the 10 EGF inversion sequence.
These were both determined using 10 eigenvalues.

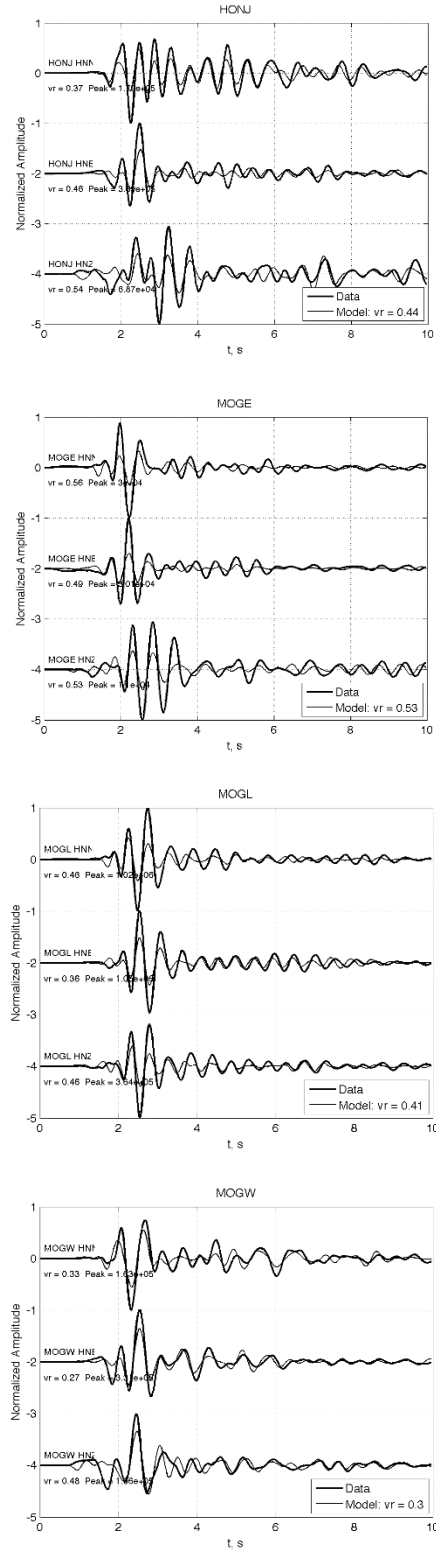


Figure 26. Matches between observed seismograms and the attempt to recreate them using the sum of empirical Green's functions.

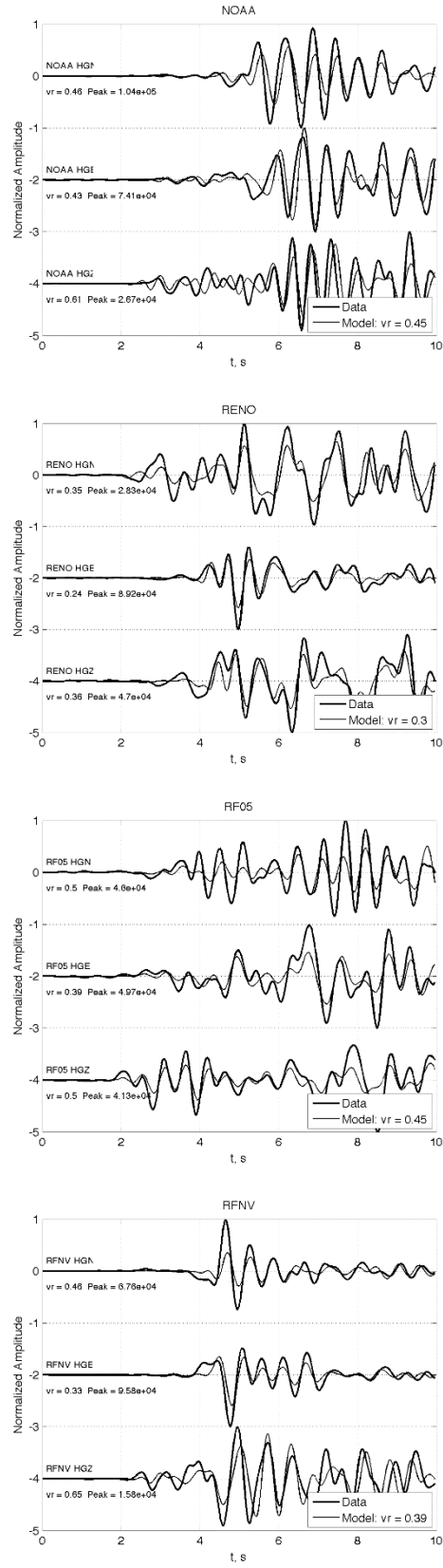


Figure 26. Continuation

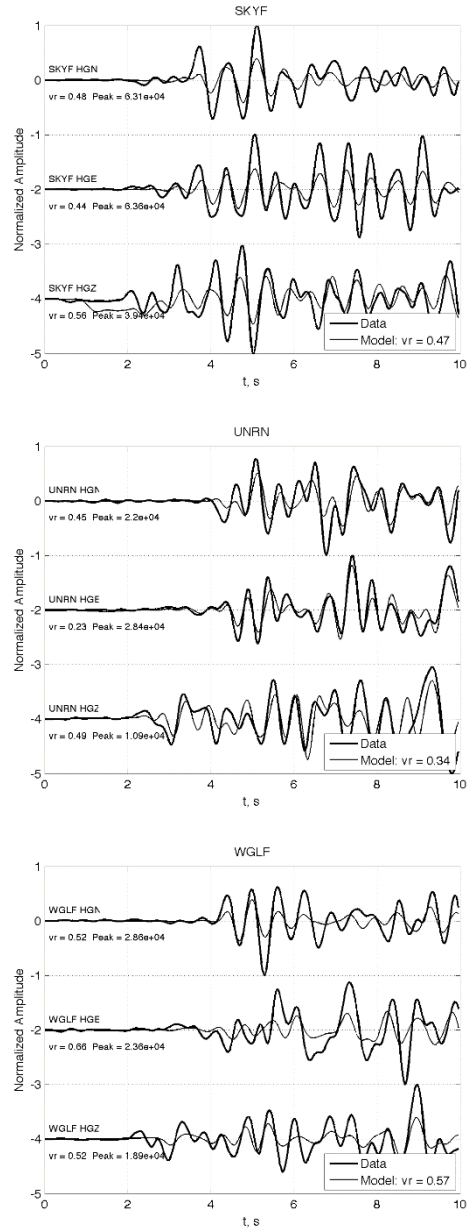


Figure 26. Continuation

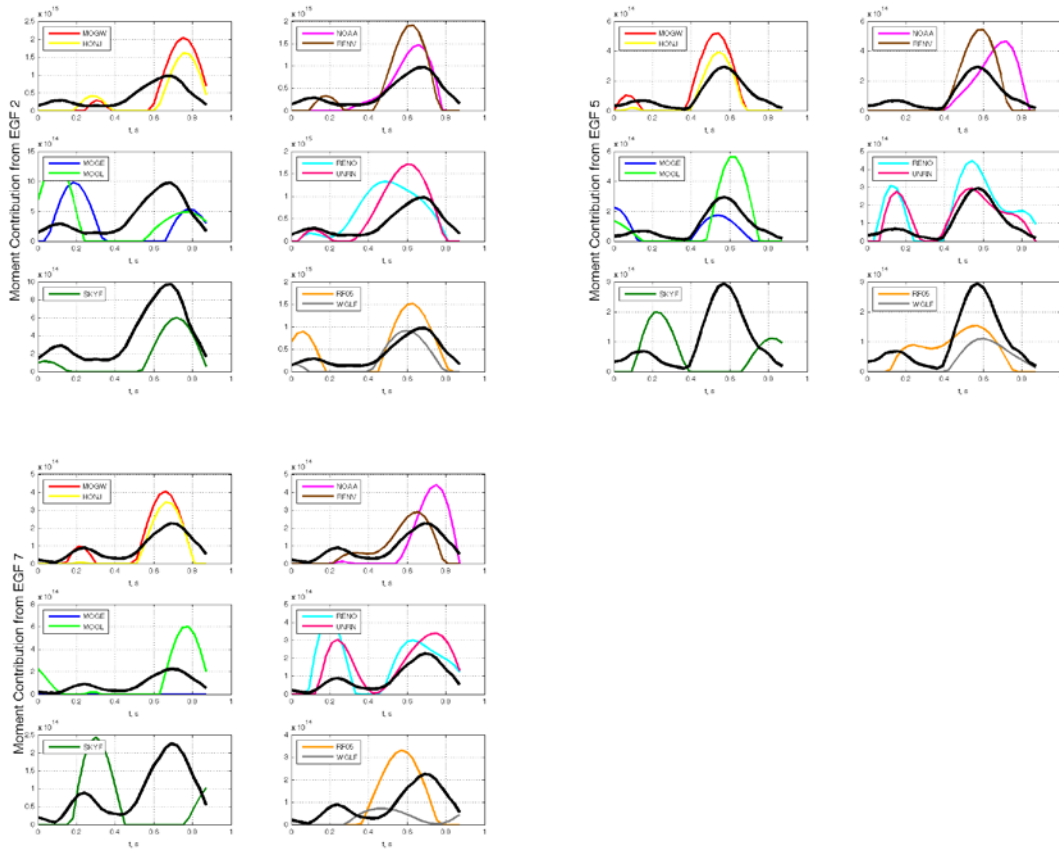


Figure 27. Slip time functions for the three EGFs that contribute most strongly to reproduce the Mogul earthquake seismograms. In each subfigure, the time functions are shown for stations grouped approximately by location.

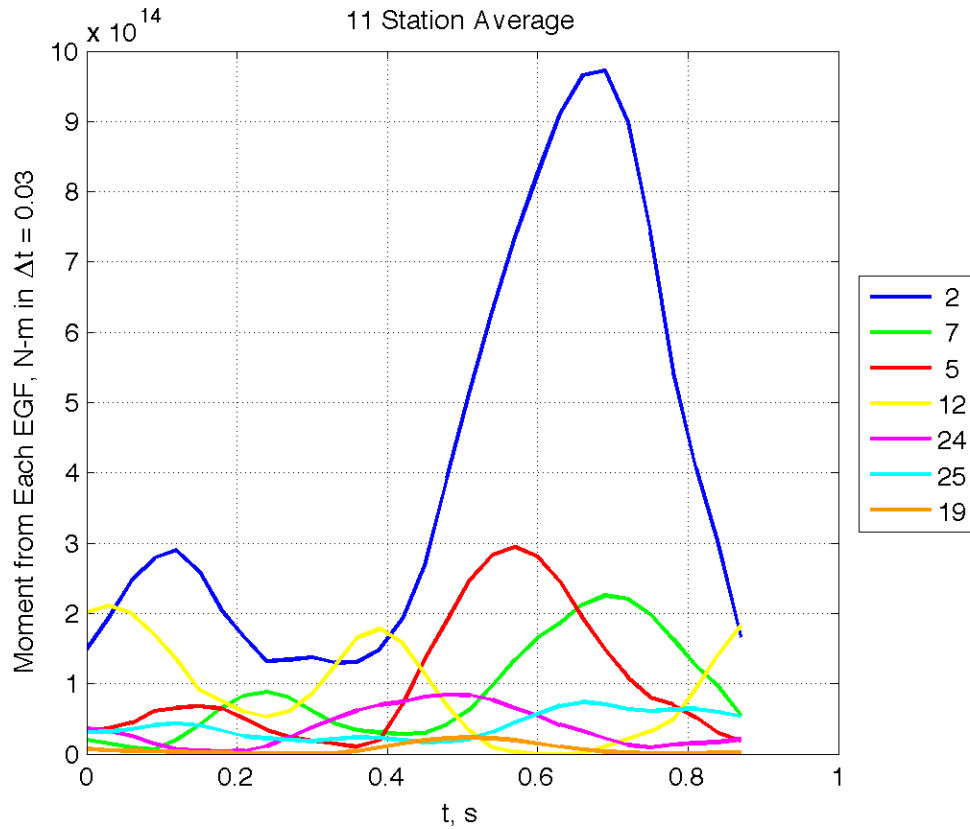


Figure 28. Moment rate for the seven EGFs used to reproduce the seismograms in Figure 25.

4.2.2.2. Measurements of Coda Envelopes to Estimate Moment Magnitude and Seismic Stress Drop

INTRODUCTION

An unusually shallow earthquake sequence occurred in 2008 in Mogul, west of Reno, Nevada. This sequence consisted of over 1938 earthquakes with M_L 1.0 or greater, 909 earthquakes with $M_L \geq 1.5$; 295 earthquakes with $M_L \geq 2.0$; 83 earthquakes with $M_L \geq 2.5$; 38 earthquakes with $M_L \geq 3.0$ and four events with $M_L \geq 4.0$. These earthquakes were concentrated in depth between 1 and 4 km and ranging in magnitude up to M_w 5.0 (the “main shock” named MS).

Direct wave amplitude measurements are affected by source radiation pattern, directivity, and heterogeneities along the path, all of which can contribute to large amplitude variability (Morasca *et al.*, 2005). Thus, a third approach was used to estimate stress drop and radiated energy: measurements of coda envelopes at different frequencies (Mayeda and Walter, 1996; Mayeda *et al.*, 2003, Malagnini *et al.*, 2006). Application of the L_g (S_g) coda amplitude ratio method is appropriate because the events in the Mogul sequence are roughly collocated (Table 6). This method takes advantage of the common path, site, and radiation pattern of co-located event pairs and it was previously used to characterize other earthquake sequences. In northern Nevada, Mayeda and Malagnini (2010) estimated the stress

drop between 5 and 10 *MPa* for the Wells, 2008, crustal earthquake sequence. This study applies coda analysis similar to methods described by Mayeda and Malagnini, (2010) and Abercrombie, (2012).

DATA

The Mogul, west Reno, NV, earthquake sequences include fifteen earthquakes with $M_w > 3.0$ (Table 6). A database of more than 8,000 broadband and short-period horizontal waveforms recorded at broadband stations in Nevada was analyzed by visual inspection. The earthquakes (Figure 29) in Table 6 were recorded by 53 Nevada Network and Transportable Array (TA) USArray (Figure 30) and by temporary broadband stations, with good signal-to-noise ratio, at 1-600 km epicentral distance. One limitation of the dataset was that some of the TA stations (all stations to the west of the line including M10A and N10A, were removed to other locations before the occurrence of the Mogul main shock. Most of the TA stations within 200 km only recorded from Julian day 059 to Julian day 081 in 2008.

METHOD

The analysis method was chosen in the context of an intense debate over stress drop scaling. Whether earthquakes are self-similar or not self-similar, and whether there is a “breakdown from constant-stress drop over some magnitude range” (Abercrombie, 2012) is not yet agreed upon. Recently, for a sequence of earthquakes in Wells, Nevada, using Lg coda analysis, it has been estimated that the main shock had higher stress drops than the largest aftershocks (Mayeda and Malagnini, 2010; Yoo and Mayeda, 2013). Using a different method and Empirical Green’s Functions (EGF’s), analysis of the Wells sequence resulted in estimated stress drops of 100–200 *MPa* for both the main shock and aftershocks (Baltay *et al.*, 2010). In a comparative analysis of both methods, Abercrombie, 2012, demonstrated that the differences in stress drop values may have been related to whether the main shock was in the numerator or the denominator of the spectral ratio. This author concluded that “although the smaller earthquake can be considered a reliable EGF at frequencies and wavelengths corresponding to the source size and duration of the large earthquake, the reverse is not true” and “it is possible that the source parameters of the smaller earthquake cannot be resolved well from spectral ratios, and the poorer resolution leads directly to an overestimate of the source size and duration”.

Considering the Abercrombie (2012) results, an attempt was made in this study to use spectral ratios with every event as a reference event. Our preliminary estimates, however, did show that, for this dataset, when using an L1 norm, the estimated smaller earthquake corner frequencies were not much different (within tenths of a second) when another event than the main shock was used. Thus, also to facilitate comparison to previous studies, the method of Mayeda and Malagnini, (2010) was selected. Lg coda ratios of the main shock and smaller earthquakes ($M_L > 3$) in the sequence were used. With the goal of improving analysis by using more high-frequency spectral ratios, Sg spectral ratios at stations very close to the epicenter (as close as 1 km) were also analyzed.

Waveform selection and decimation criteria closely followed the procedure used by Phillips *et al.*, 2008. After deconvolving the instrument, the velocity (*nm/s*) trace was decimated, then filtered using a Butterworth, four-pole, zero phase band-pass filter in eleven consecutive narrow frequency bands ranging between 0.02 and 8.0-Hz. Decimation was performed to maintain the bandwidth to Nyquist frequency ratio greater than 0.05, ensuring stability of the band-pass filter. After Hilbert transform envelope processing and taking a base-ten logarithm, the resulting envelopes were smoothed and horizontal component envelopes were averaged together. An example of an event and of envelope

estimates is shown in Figure 31. To remove events with coda contaminated by other event arrivals, the coda windows were hand-picked and their median values are listed in Table 7.

Calibrated synthetic envelopes were used to measure the observed envelope's amplitude as a function of frequency by shifting the synthetics until they matched the observed envelopes. The envelope interpolation used an L-1 norm. Coda shape parameters γ (here named GAMMA) and b (here named BETA) as used by Mayeda et al., 2003, Equation 3, were estimated using a grid search and the Matlab function *fminsearch* (Lagarias et al., 1998). Examples of fitting synthetic envelopes to the observed data are shown in Figure 32.

RESULTS AND DISCUSSION

Maps of GAMMA, respectively BETA values estimated at each station are shown in Figures 33 and 35. Maps of the GAMMA and BETA interquartile range (*iqr*) are shown in Figures 34 and 36. Note relatively invariant coda shape with distance and back azimuth (GAMMA and BETA) at frequencies below 1 Hz and relatively large variation in coda shape parameters at highest frequencies, particularly in the near-field. Data spread is higher at higher frequencies for GAMMA. When compared to GAMMA, variations of the BETA parameter and of its *iqr* with distance and back azimuth are relatively small over the study area, at all frequencies. Figures 33-36 show that relatively significant spatial variations of the *Lg* (or *Sg*) coda shape parameters may be expected for frequencies exceeding 2 Hz at distances from 1 to 600 km. As they seem to follow tectonic complexity, such as basins and the Sierra Nevada outlines, these variations may be due to unique crustal complexities in the western Basin and Range.

The spectral ratio fits are shown in Figure 38 (as a result of a one "free" parameter *fminsearch* application). At each frequency, each point (black open circles) in this figure is the median value, for all the stations, of the spectral ratios between the MS and the largest aftershocks. The spectral ratios at the lowest frequency are fixed, i.e. are the ratios of the seismic moments listed in Table 6. Spectral ratios smoothed with a 5 point step are the blue dots. The *iqr* of the unsmoothed data is shown in each figure as blue vertical bars. When vertical bars are missing, *iqr* is zero, because it was calculated for one estimate. The highest frequency point is fixed and equal to the median of the last three ratio values.

The MS corner frequency was estimated in a first iteration with a two "free" parameter *fminsearch*. Initially, based on visual inspection of all the available spectral ratios, the "preferred" MS corner frequency was chosen as 0.6 s and was the first parameter input in *fminsearch*. The second input parameter, the "preferred" corner frequency of the smaller events was empirically chosen for all the smaller earthquakes. Applying this search for every spectral ratio, an initial set of corner frequencies was estimated. The second iteration used a one "free" parameter *fminsearch*. For each earthquake, the input "preferred" parameter was the corner frequency estimated in the first iteration. The MS median corner frequency was fixed at 0.72 Hz. The final spectral fits are shown in Figure 37, and the estimated corner frequencies are shown in Table 8. The corner frequency of the MS was estimated as 0.8 Hz by Biasi and Anderson (Task 2.1), who estimated the corner frequencies of the other $M_L > 3$ events between one and four Hz for soil sites and between two and six Hz for rock sites.

As shown Figure 37, this sequence of earthquakes appears to violate self-similarity, similar to the Wells, Nevada sequence (Mayeda and Malagnini, 2010). Even when using observations at stations as close as 1 km, the observed high-frequency level never reaches the theoretical high-frequency asymptote (dotted line in Figure 37).

Uncertainties in the corner frequencies of the smaller earthquakes can be estimated from plots in Figure 38. The sum of the absolute values of the differences between the observed and estimated spectral fits (“Sum abs err” named here SE) is represented as a function of percent variations of the corner frequencies from the values in Table 8. While for some earthquakes (events 6, 14 and 15) SE increases rapidly for corner frequency within 10% of the estimated values, for other earthquakes (events 2,8,10 and 11) low SE values indicate a larger (up to 20%) set of possible corner frequencies. The plots in Figure 38 show that at least some of the corner frequency values may be under-estimated by as much as 10-20 %. This result may be in accord to the conclusion in Abecrombie (2012) that “Corner frequencies determined for an earthquake that is the smaller in a spectral ratio are systematically lower (and typically less well constrained) than when the same earthquake is the larger in the ratio.”

The apparent stress and stress-drop were estimated using equation 11 in Phillips et al., 2008, and equations 3 and 4 in Mayeda and Malagnini (2010). The *S*-wave velocity was 2.87 km/s and the *P*-wave velocity was 5.13 km/s (Biasi *et al.*, 2012). The median apparent stress for the main shock was estimated at 1.2 MPa, for a moment of 4.07×10^{16} Nm, with an *iqr* of 0.84 MPa. The ten-base logarithm of the apparent stress as a function of the ten-base logarithm of the seismic moment (Table 6) is shown in Figure 39 and the dependence does not seem linear, as predicted theoretically.

The Brune (1970) median stress drop in MPa (Mayeda and Malagnini, 2010) was estimated for the main shock as 5.6 MPa, with *iqr* of 4.1 MPa. Although the corner frequency estimates were proportional to the estimated seismic moment values, Figure 40 shows a non-linear dependence of ten-base logarithm of the seismic moment and the ten-base logarithm of the stress drop. As with apparent stress, the 100-fold lower values for the smallest earthquakes in the Mogul sequence may be method errors, which result in too low estimates of corner frequency (Abercrombie, 2012).

The stress drop estimated as a function of seismic moment is shown in Figure 41, superposed on Figure 3 from Mayeda et al., 2013, for comparison. The yellow dot is the Mogul MS and the black dots are the Mogul smaller earthquakes, with $M_L > 3.0$. The estimates of this study are within the range of the stress drops observed in Northern Nevada by Mayeda and Malagnini (2010) and support different scaling for the MS.

The results of this study agreed with the results obtained using direct phases by Biasi and Anderson, Task 2.1, however, differed from the results of Anderson *et al.*, (Task 2.2). Using EGF's these authors estimated the main shock stress drop as 17.5 MPa, which was “a very high stress drop”. They calculated that, for a crustal density of 2.6 g/cm³, the lithostatic stress at 2 km would be ~50 MPa (500 bars), implying that the stress drop in this earthquake was a large fraction of the lithostatic stress. In support of these affirmations, they cited Bell *et al* (2012) found that the aseismic slip in this earthquake had a seismic moment exceeding the seismic slip, indicating that this fault may have had essentially a complete stress drop during the sequence.

Errors in corner frequency estimates when using this method may be due to the lack of long period waveforms for all the earthquakes except for the main shock and to using the moment ratios instead. Another possible method error may be due to the main shock being at the numerator of the spectral ratios, ie overestimation of the MS corner frequency, and underestimation of the smaller event corner frequency.

Figure 42 shows M_w , as a function of the network magnitude M_L . M_w was estimated using the Hanks and Kanamori (1979) formula, $M_w = 2/3 \log_{10} (M_0) - 6$ (where M_0 is in Nm). The correspondence of the two magnitude scales was good for all events, except for the main shock.

CONCLUSIONS

Using L_g coda, estimates of the apparent stress for the MS were 1.2 MPa, for a moment of 4.07×10^{16} Nm, with iqr of 0.84 MPa. The stress drop in MPa was estimated for the main shock at 2.3 MPa, with a range from 2.3 MPa to 3.9 MPa. 5.6 MPa, with iqr of 4.1 MPa. The stress drop values are consistent to the direct phase spectral analysis at Task 2.2 and to stress drops estimated using the same methods in northern Nevada by other authors, however, are smaller than the values estimated using Greens Function analysis in Task 2.2. The MS corner frequency was 0.72 Hz, with iqr 0.2 Hz. Unlike for the main shock, the local and moment magnitude values for the smaller earthquakes with $M_L > 3.0$ are within 0.2 units.

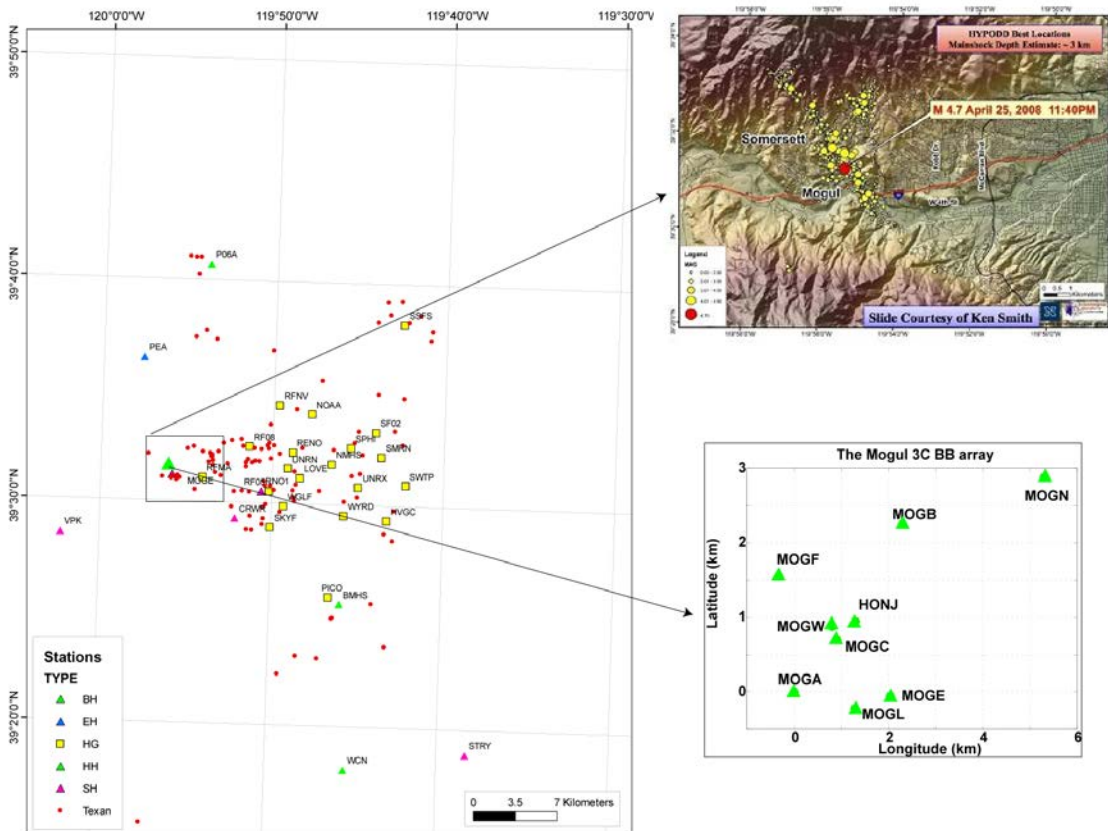


Figure 29. Permanent and temporary stations recording the Mogul sequence. Lower-right inset shows the IRIS Rapid Array Mobilization Program (RAMP) deployment. Stations MOGE, MOGL, MOGW, and HONJ (green triangles) recorded the mainshock and the most energetic fore- and aftershocks. “Texan” digitizers (red dot locations) were deployed with high frequency geophones to study basin structure using natural sources, and recorded continuously for only three days at each point. The seismicity of the Mogul sequence is shown in the upper right plot (Smith et al., 2008). Earthquakes shown are from a set relocated with a double-difference algorithm.

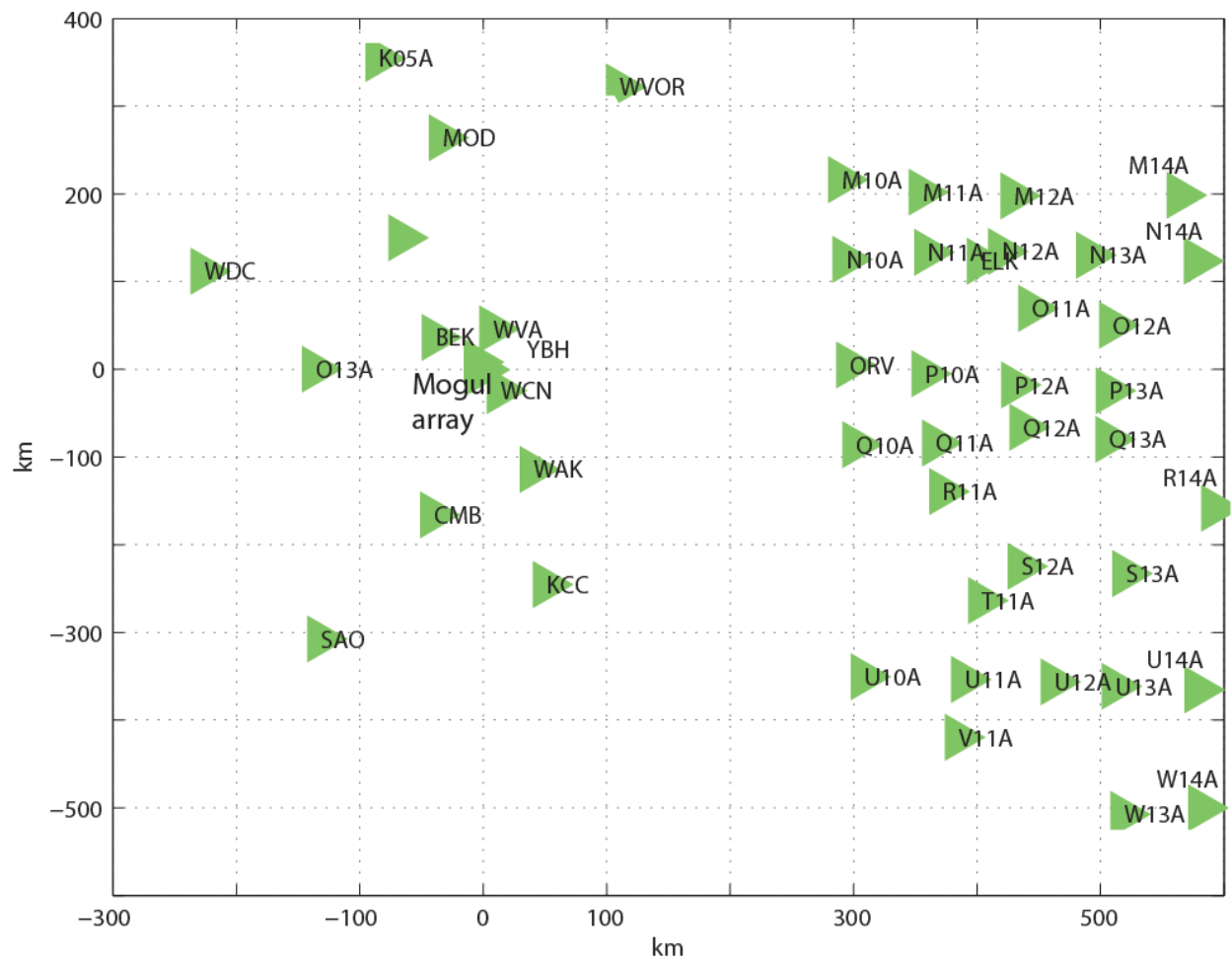


Figure 30. Stations (green triangles) used in this study. *The Mogul array stations used were: MOGA, MOGB, MOGC, MOGE, MOGF and MOGL.*

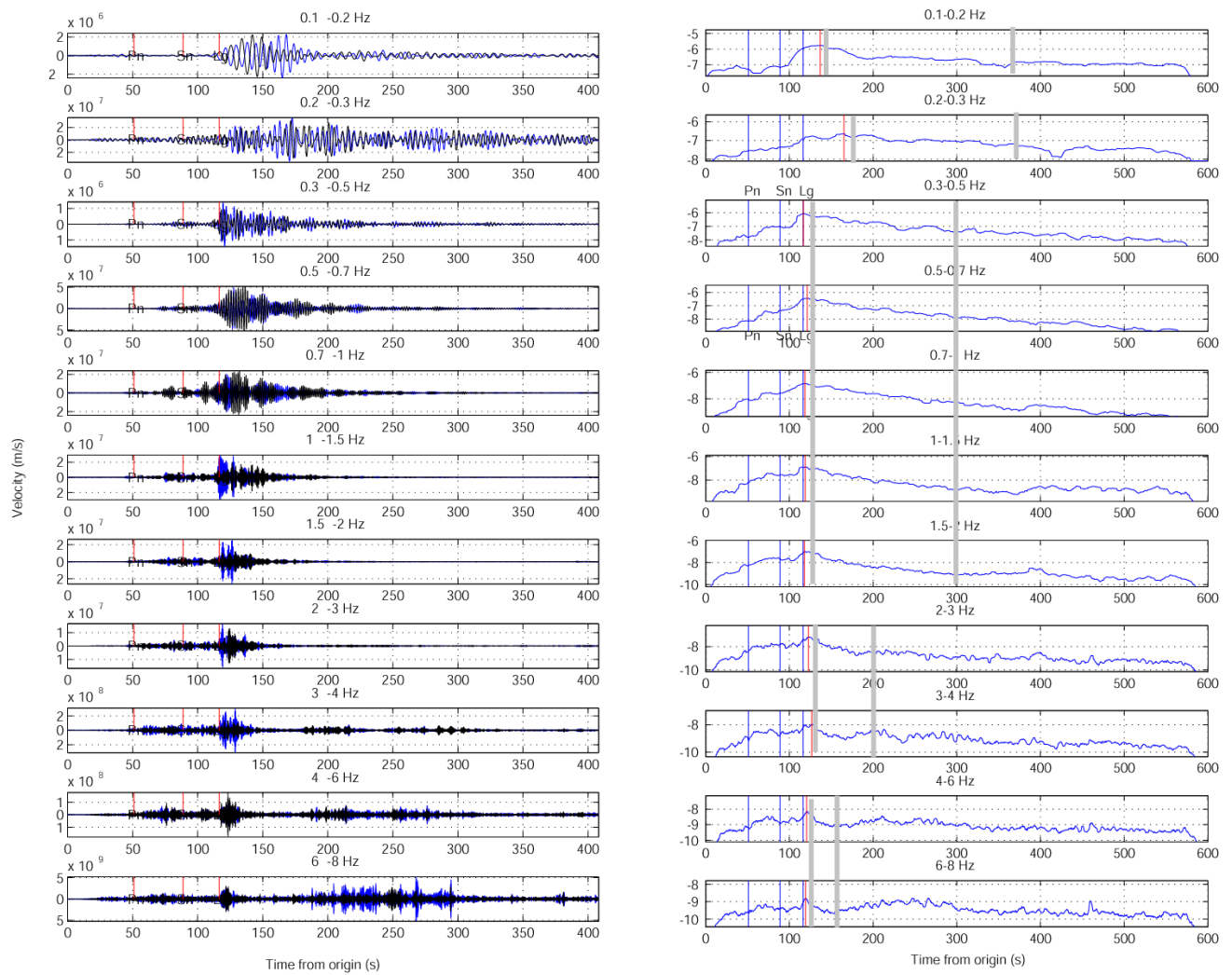


Figure 31. Earthquake No 3 (Table 6) waveforms and coda envelopes at station M11A. *Left: Waveforms filtered in consecutive frequency bands from 0.1 to 8 Hz. Right: Narrow band envelopes. Note a strong frequency-dependence in the coda envelopes shape, which makes manually picking the windows necessary.*

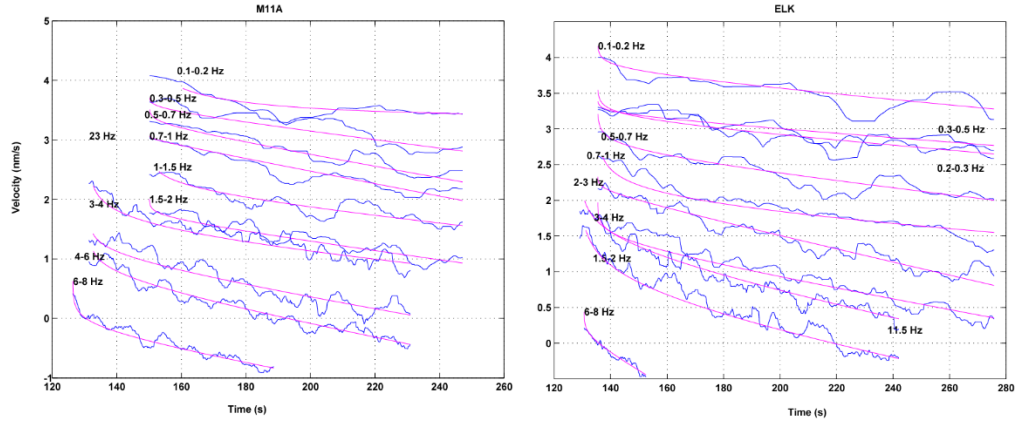


Figure 32. Synthetic envelopes (red) were fit to the observed main shock coda envelopes (blue), and Lg coda amplitudes were estimated for each event in each frequency band.

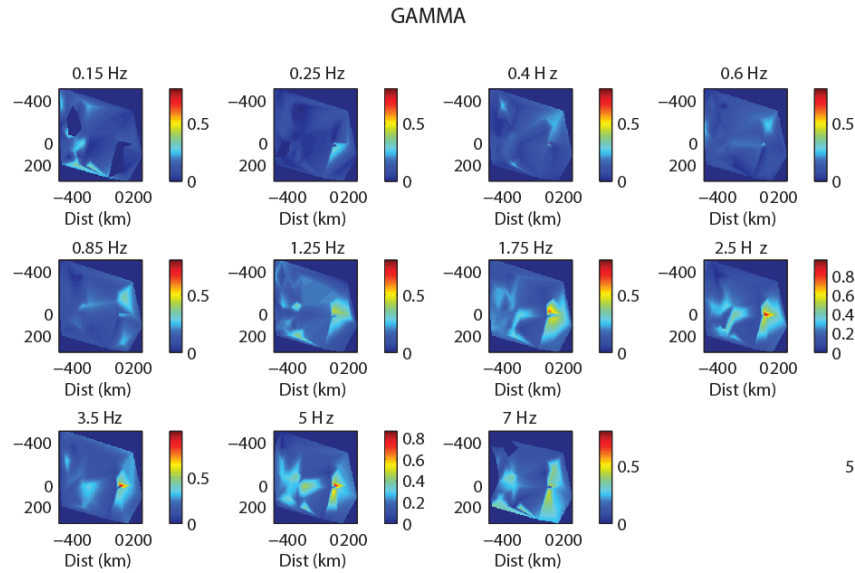


Figure 33. Maps of the coda shape parameter GAMMA estimated at each station for each center frequency. The point of coordinates (0,0) is the location of the MS. Note relatively invariant GAMMA as a function of distance and back azimuth up to approximately 1 Hz, and strong variations at higher frequencies at the near-field stations.

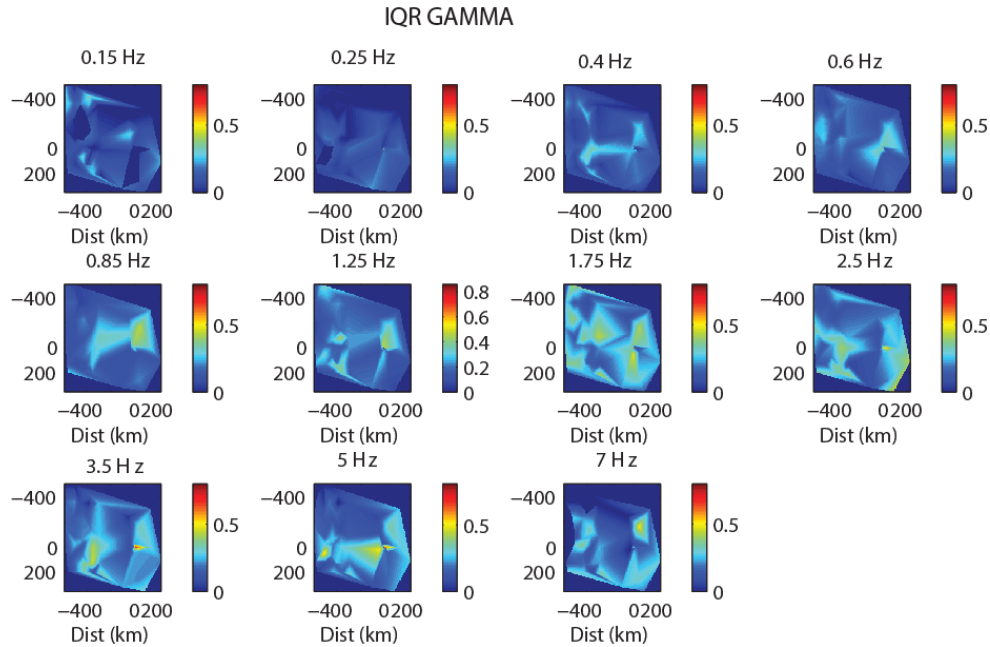


Figure 34. Maps of the interquartile range (a measure of statistical dispersion, being equal to the difference between the 75th upper and 25th lower quartiles) of the coda shape parameter **GAMMA** estimated at each station for each center frequency. The point of coordinates (0,0) is the location of the MS. Note relatively high spread of the GAMMA values at frequencies higher than 1 Hz.

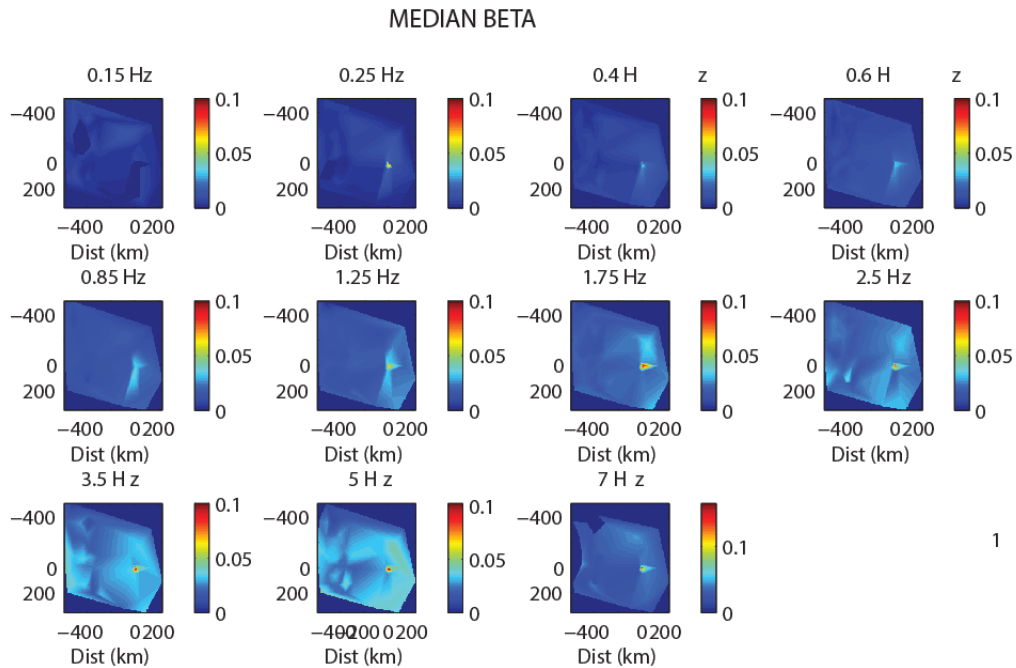


Figure 35. Maps of the coda shape parameter **BETA** estimated at each station for each center frequency. The point of coordinates (0,0) is the location of the MS. Note relatively invariant BETA as a function of distance and back azimuth, however, note strong variations at higher frequencies, at the near-field stations.

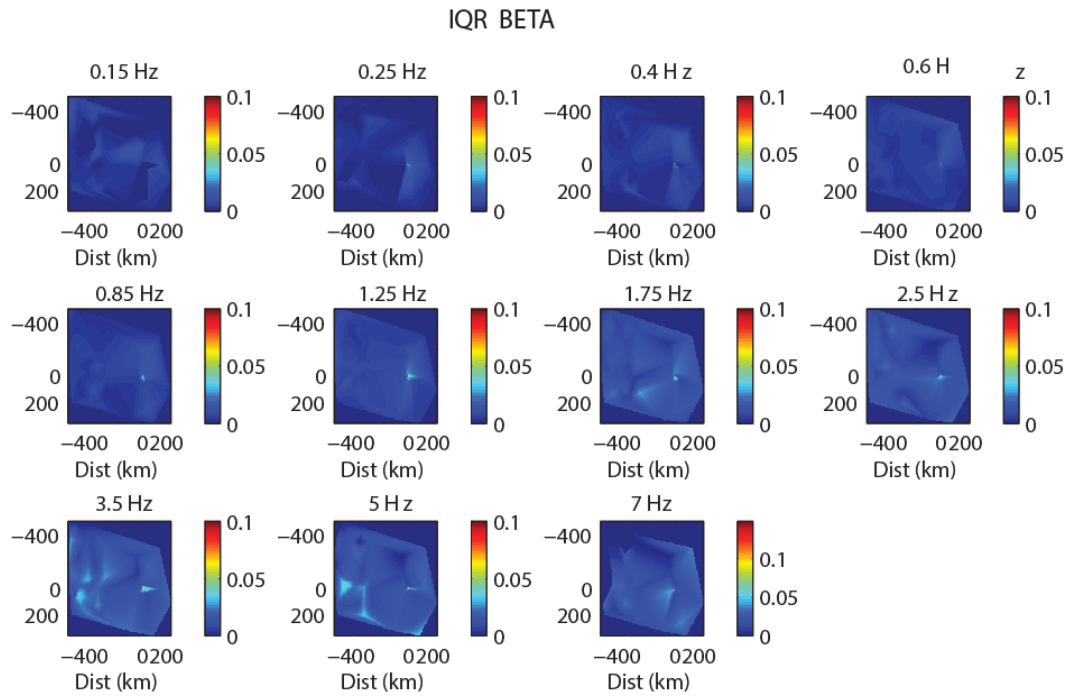


Figure 36. Maps of the interquartile range (a measure of statistical dispersion, being equal to the difference between the upper and lower quartiles) of the coda shape parameter BETA, estimated at each station for each center frequency. *The point of coordinates (0,0) is the location of the MS. Note relatively invariant BETA as a function of distance and back azimuth. Note relatively low spread of the BETA values.*

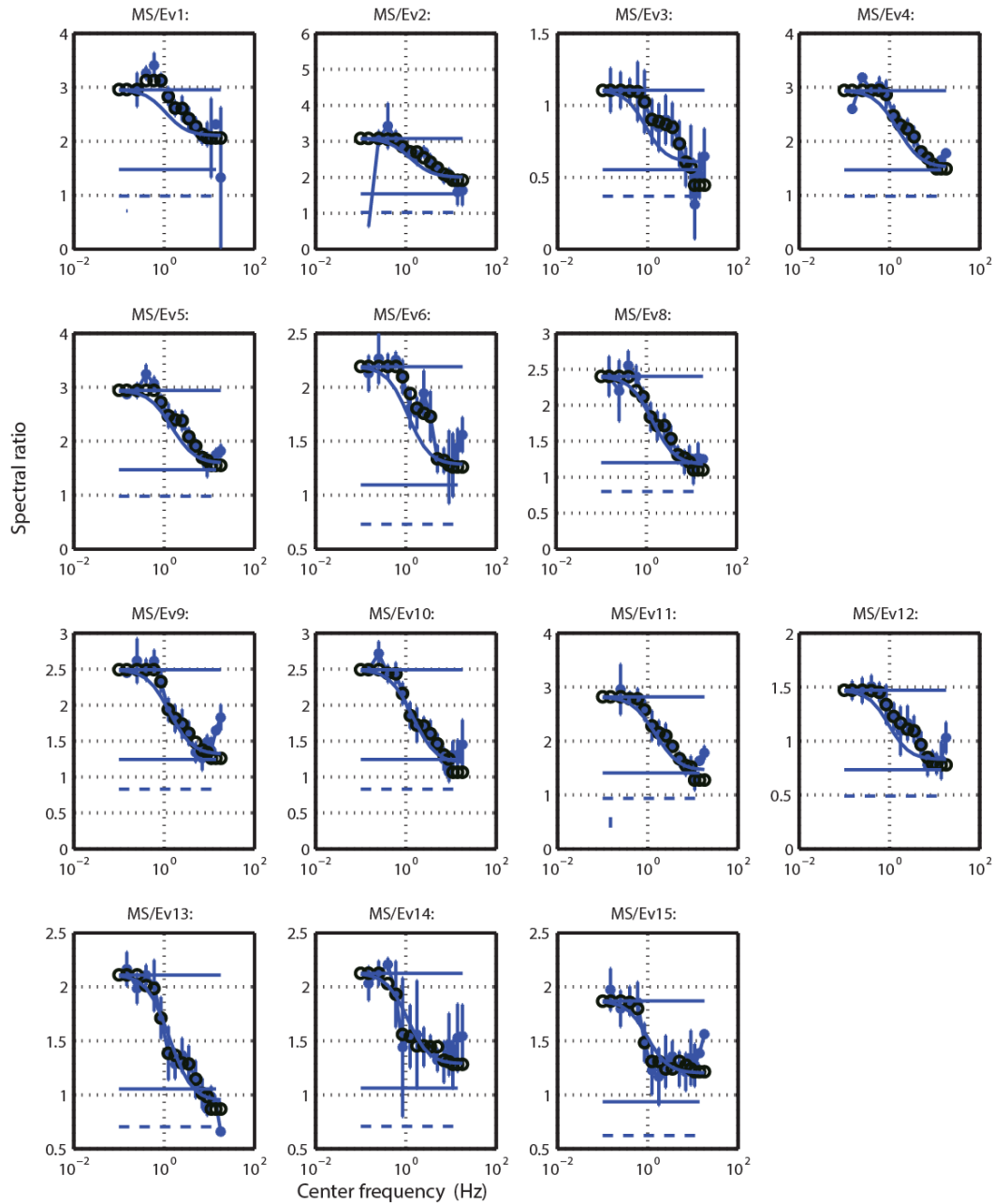


Figure 37 The spectral ratio fits for the events in Table 6, in the case with MS 0.72 Hz and small earthquake frequencies are unconstrained. The black open circles are the median spectral ratios over all stations at each frequency. The blue dots at each frequency are the smoothed spectral ratios, each point representing the median of a set of five points, centered on the respective frequency. The vertical blue lines are the iqr valued of the un-smoothed data. The thin blue lines are the fitted function after corner frequency estimation by the *fminsearch*. The top horizontal solid line represents the theoretical low-frequency limit based upon the two events' moment estimates, the bottom solid line represents the theoretical high-frequency limit assuming self-similarity, and the dashed line is when $p = 1.5$ in equation (1) in Mayeda and Malagnini (2010). MS represents the main shock.

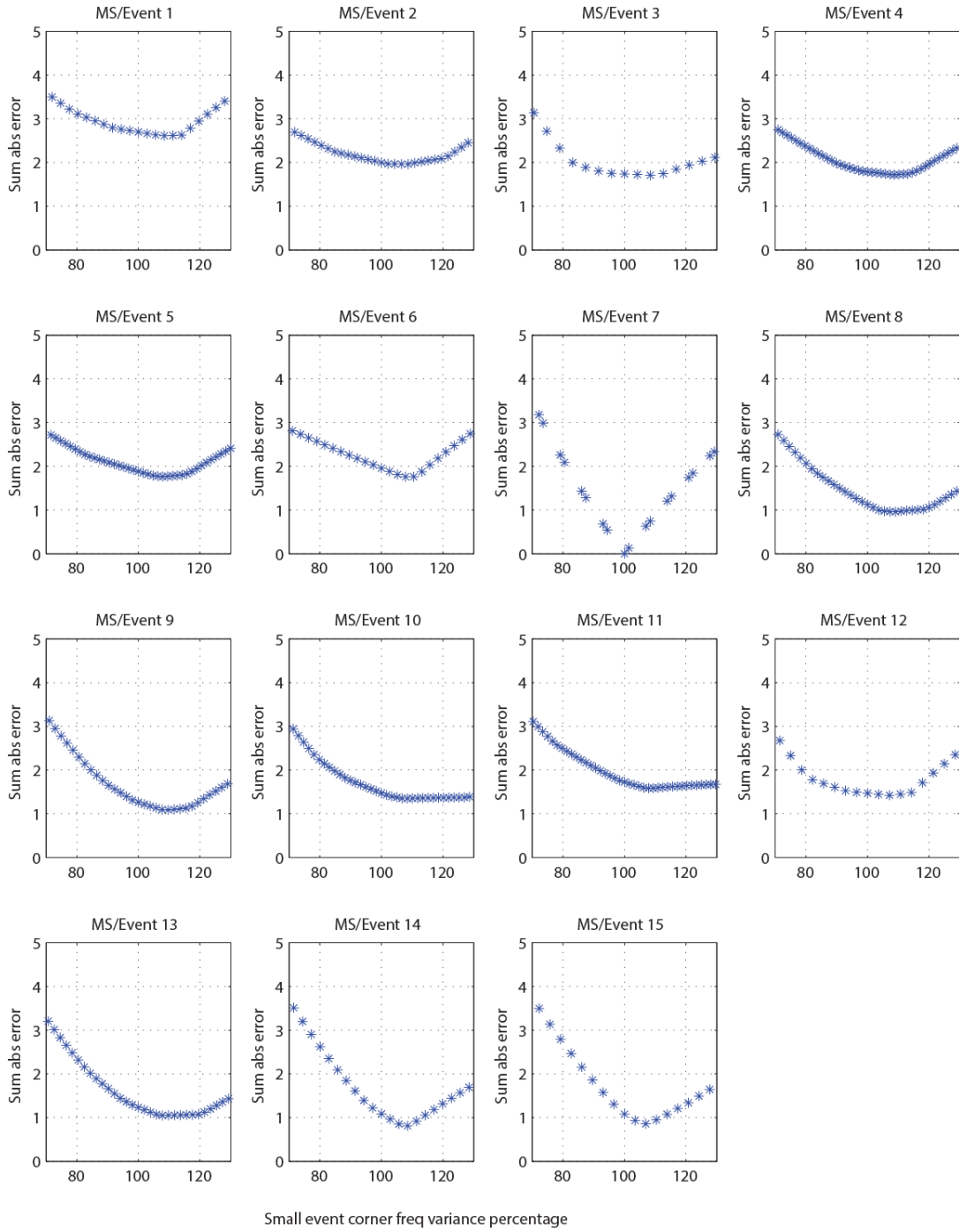


Figure 38. The sum of the absolute errors of the fits in Figure 37 as a function of percentage variance of the corner frequency from the values in Table 8.

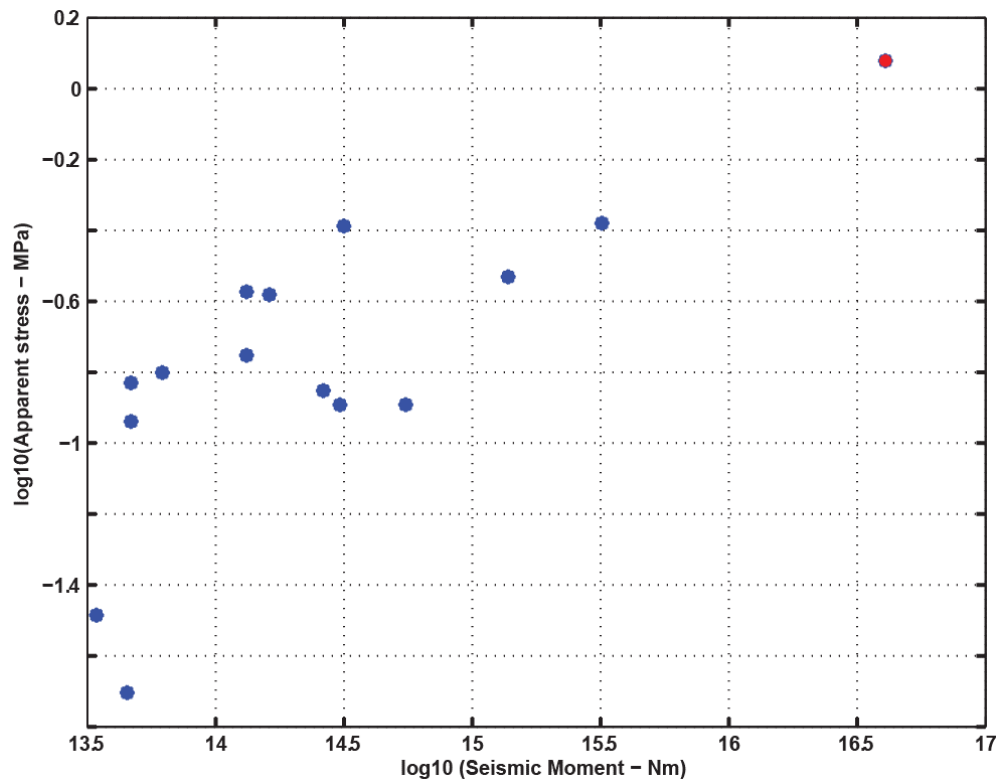


Figure 39. The ten-base logarithm of the apparent stress (MPa) as a function of ten-base of the seismic moment in Table 6.

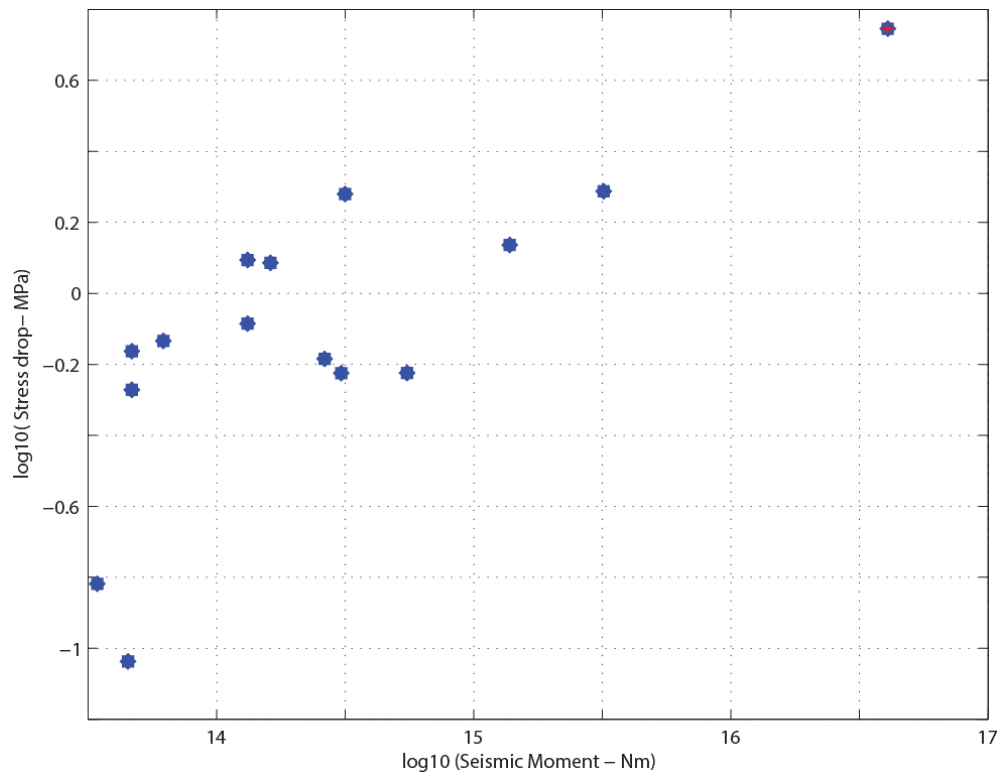


Figure 40. The ten-base logarithm of the stress drop (MPa) as a function of the ten-base logarithm of the seismic moment in Table 6.

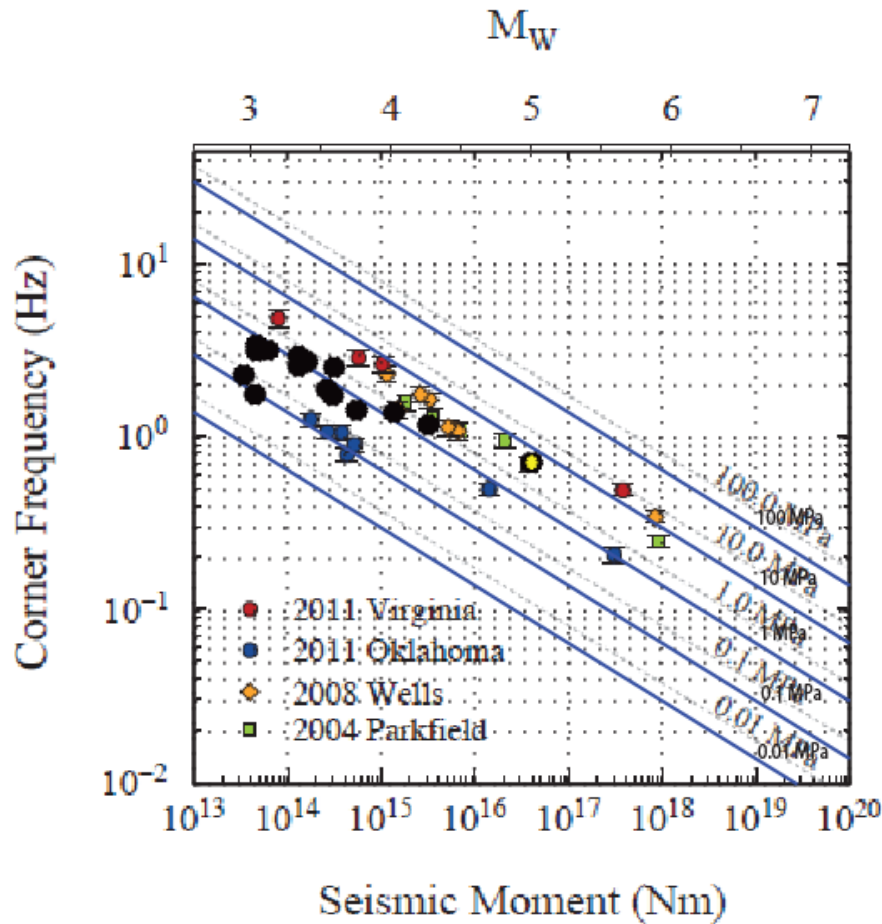


Figure 41. Corner frequency as a function of the seismic moment for the Mogul sequence (yellow dot, the MS and black dots, the smaller earthquakes) superposed on Figure 3 in the study by Yoo and Mayeda, 2013. The Mogul sequence observations were as Mayeda et al observed, “Results of corner frequency versus seismic moment for all four U.S. sequences all show an increase in stress drop and apparent stress. A dramatic difference in apparent stress is observed which appears to be dependent upon the source region.” The 100-fold lower stress drop observations for the smallest earthquakes in the Mogul sequence may affected by method errors (too low estimates of corner frequency). Also, the corner frequency – moment variation look similar for the 2011 Oklahoma and the 2008 Mogul sequences.

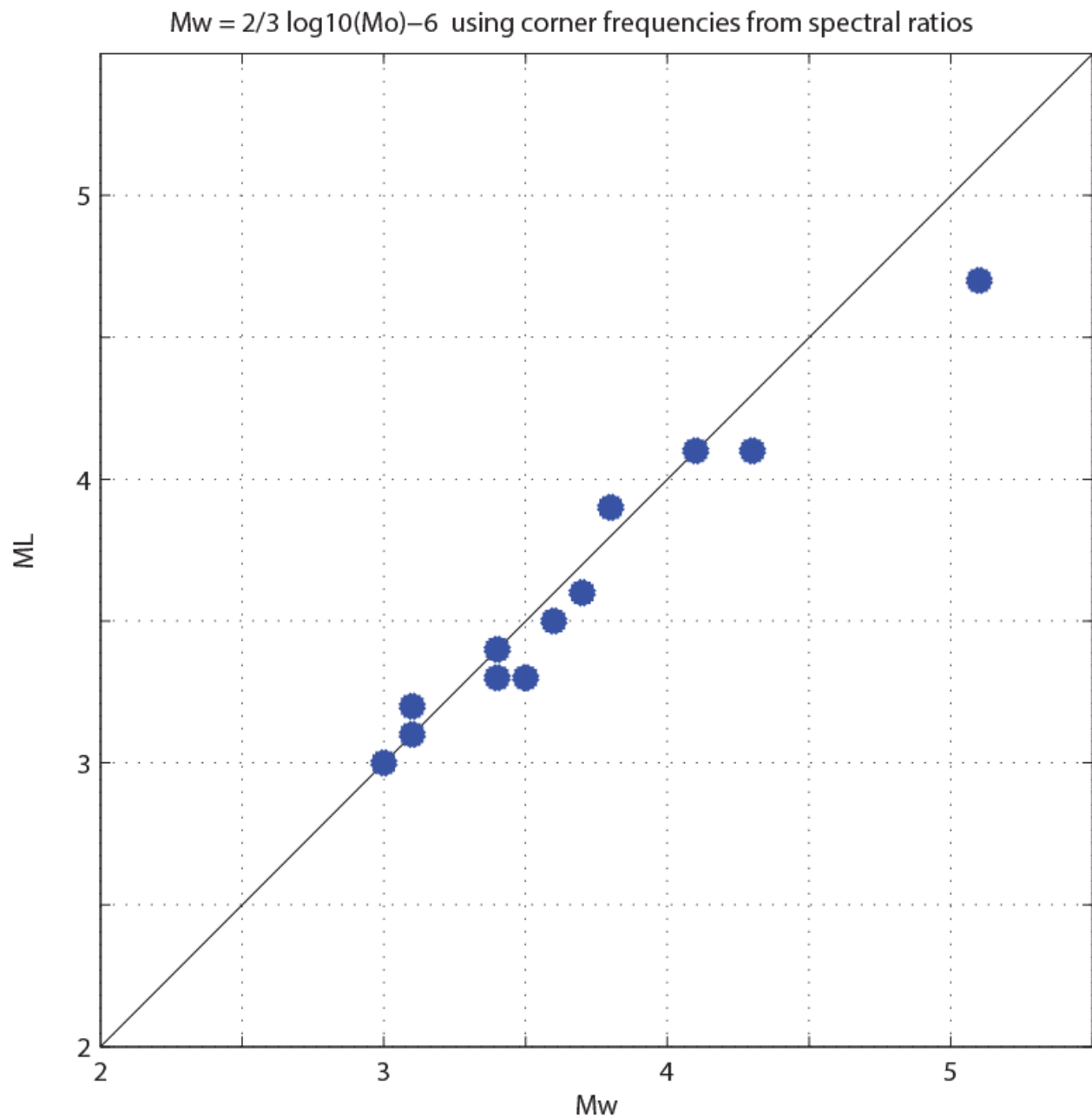


Figure 42. M_L as a function of M_w for events used in this study. M_w was estimated using the Hanks and Kanamori (1979) formula, $M_w = 2/3 \log_{10}(M_0) - 6$, where M_0 is in Nm.

Table 6. Focal mechanism and moment tensor of the largest ($M_L > 3.0$) Mogul earthquakes. The relation between seismic moment, M_0 and moment magnitude M_W is $\log M_0 = 1.5 M_W + 16.05$, where the seismic moment is in units of dyne-cm. Gray colors are used to mark sources of moment tensor solutions. M_W UNR was estimated by Biasi et al, 2012.

Event (date, Julian day, time)	NSL (this study) HYPODD -estimated event parameters (latitude deg, longitude deg, depth km, M_L)	Other party (source) location (latitude deg, longitude deg., depth/moment-tensor depth km)	Moment M_0 (dyne-cm)	M_W/M_W UNR	Focal mechanism solution			Source
					Strike (deg)	Dip (deg)	Rake (deg)	
2008/04/21 (112) 19:14:10.44	39.5166, -119.9145, 2.941, 3.1	39.517, -119.922, 2.6/8	0.0452e+22	3.07/3.3	51 142	32 90	0 -122	Gene Ichinose moment tensor estimate at NSL
2008/04/24 (115) .22:47:04	39.5299, -119.9167, 4.35, 4.0	39.533, -119.932	0.495e+22	3.7/4.0	146 240	76 75	164 15	SLU Moment Tensor Solution
		39.533, -119.932, 1.1/4	0.82e+22	3.91/4.0	239 331	50 88	-2 -140	Gene Ichinose moment tensor estimate at NSL
2008/04/24 (115) 22:51:06	39.5316, -119.9278, 2.13, 3.0	39.533,- 119.932,1.8/4.0	0.0343e+22	3.0	37 128	60 89	-1 -150	Gene Ichinose moment tensor estimate at NSL
2008/04/24 (115), 22:55:48	39.5299, -119.9260, 3.233, 4.1	39.550 -119.887 0.0	3.20e+22	4.3/4.4	245 152	85 60	30 174	SLU Moment Tensor Solution
		39.527, -119.929, 2.8/4.0	6.0954 e+22	4.49/4.4	61 152	83 81	-9 -173	Gene Ichinose moment tensor estimate at NSL
2008/04/25 (116) 01:00:33	39.5248,- 119.9204,2.56,3.3	39.531,-119.929,2.2/6	0.0468 e+22	3.08/3.4	226 321	79 70	-20 -168	Gene Ichinose moment tensor estimate at NSL
2008/04/25 (116) 17:30:10	39.5255, - 119.9204,2.52,3.3	39.531,-119.928, 1.4/4.0	0.0468 e+22	3.08/3.4	228 318	89 78	-12 -179	Gene Ichinose moment tensor estimate at NSL
2008/04/26 (117) 01:13:20.92	39.5276, -119.9217, 2.43, 3.7	39.529, -119.918, 1.6/5	0.263e+22	3.58/3.8	72 341	64 88	3 154	Gene Ichinose moment tensor estimate at NSL
2008/04/26 (117), 06:40:10	39.5247, -119.918, 2.6, 4.7	39.520 -119.930 8.0	2.72e+23	4.9/5.1	240 147	80 75	15 170	SLU moment tensor solution http://www.eas.slu.edu/eqc/eqc_mt/MECH.NA/20080426064010/index.html
2008/04/26 06:40:15.1	39.5247, -119.918, 2.6, 4.7	39.57 119.91 15.4	3.87e+23	5.0/5.1	328 238	86 87	-177 -4	GCMT (Meredith Nettles)
2008/04/26 06:40:14.07	39.5247, -119.918, 2.6, 4.7	39.4687 -120.0587 5	3.40e+23	4.9/5.1	60 328	25 174	85 65	Achung, UCB Seismological Laboratory
2008/04/26 06:40:	39.5247,- 119.918,2.60,4.67	39.52, -119.93, 1.4/4	4.0738e+23	5.04/5.1	57 147	85 85	-5 -175	Gene Ichinose moment tensor estimate at NSL
2008/04/26 (117) 07:29:20	39.5286, -119.9195, 2.88, 3.5	39.527, -119.927, 2.7/7	0.162e+22	3.44/3.6	166 277	36 76	-25 -123	Gene Ichinose moment tensor estimate at NSL
2008/04/26 (117) 09:11:59	39.5265, -119. 9171, 1.99, 3.4	39.525, -119.927,2.1/4	0.132e+22	3.38/3.6	26 136	52 67	-30 -138	Gene Ichinose moment tensor estimate at NSL
2008/04/26 (117) 15:20:40.23	39.5435, -119.9354, 2.18, 3.5	39.543,-119.936,1.1/5	0.132e+22	3.38/3.6	41 135	36 87	-6 -126	Gene Ichinose moment tensor estimate at NSL

2008/04/27, (118), 17:49:49.82	39.5192, -119.9145, 3.20, 3.3	39.529,-119.918,1.8/5	0.062e+22	3.16/3.4	213 311	59 77	-15 -148	Gene Ichinose moment tensor estimate at NSL
2008/04/28,(119) 11:33:18	39.5273, -119.9213, 2.12,4.3	39.533 -119.931, 0.1/5	1.38e+22	4.06/4.1	225 315	87 87	-3 -177	Gene Ichinose moment tensor estimate at NSL
2008/04/28, (119), 11:33:18	39.5273, -119.9213, 2.12,4.3	39.570 -119.913 1.0	1.45e+22	4.0/4.1	135 45	90 85	-175 0	SLU Moment Tensor Solution
2008/05/08 05:55:02	39.5405, -119.9166, 2.72, 3.8	39.539 -119.915 3	0.316e+22	3.6/3.9	25 117	85 70	-20 -175	SLU Moment Tensor Solution
2008/06/08 (160), 17:53:41	39.5462,- 119.9145,1.89,3.6	39.55 -119.91 2.6	0.305e+22	3.6/3.9	132 40	80 80	-170 -10	SLU Moment Tensor Solution
2008/06/08 (160), 17:55:19	39.5430, -119.9148, 1.88, 3.9	39.55 -119.92	0.550e+22	3.8/4.2	210 330	55 55	45 -135	SLU Moment Tensor Solution

Table 7. Used frequency bands and median coda window for each band. “*” refers to frequency bands only available at stations within 20 km from the main shock.

Frequency band (Hz)	Median coda window (sec)
0.1 - 0.2	118
0.2 - 0.3	96
0.3 - 0.5	131
0.5-0.7	136
0.7-1.0	134
1.0-1.5	128
1.5-2.0	108
2.0-3.0	87
3.0-4.0	66
4.0-6.0	56
6.0-8.0	44
8-10*	31
10-12*	31
12-16*	31
16-20*	31

Table 8. Earthquake parameters for the smaller earthquakes in the Mogul sequence. f_c is the corner frequency.

Event No.	Event	Moment $\times 10^{-22}$ dyne cm	Event f_c (Hz)
1	2008112191410	0.0452	1.8
2	2008115225106	0.0343	2.3
3	2008115225549	3.2	1.2
4	2008116010033	0.0468	3.4
5	2008116173010	0.0468	3.2
6	2008117011320	0.263	1.9
7	2008117072920	0.162	2.8
8	2008117091159	0.132	2.6
9	2008117152040	0.132	3.0
10	2008118174949	0.062	3.2
11	2008119113318	1.38	1.4
12	2008129055501	0.316	2.5
13	2008160175340	0.305	1.8
14	2008160175519	0.550	1.4

4.3 TASK 3

For the third task, we investigate the effect of source depth on P and S spectra and spectral ratios, signal complexity, and m_b - M_s discrimination. In a region of the world where natural and man-made seismic sources are scarce, and verification decisions will have to be made with little prior data for comparison, it is crucial to know if a discriminant may fail for a very shallow earthquake sequence.

Several forms of discriminant analysis were considered, as follows: 1) Short-period spectral amplitude ratio discriminants (Sub-task 4.3.1); magnitude-to-magnitude ratios (Sub-task 4.3.2), depth and complexity discriminants (Subtask 4.3.3).

We aimed to answer questions including:

- 1) Are the Mogul earthquakes classified by classic discrimination algorithms as different from deeper earthquakes and nuclear and commercial explosions?

- 2) Are the parameters of very shallow earthquakes uncharacteristic only in the vicinity of the source?
- 3) What is the magnitude threshold below which the classic discriminants stop working?

4.3.1 Spectral Ratio Discrimination

INTRODUCTION

When using short-period spectral ratio discriminants, very shallow events (depth < 5 km) have been found to look explosion-like (Walter *et al.*, 1995). We are reporting investigations of the effectiveness of frequency $f > 0.2$ Hz spectral ratio discrimination algorithms when applied to the very shallow earthquake sequence that occurred in 2008 in Mogul, west Reno, Nevada. We compare the results to results from deeper (depth > 5 km) earthquake sequences in the Basin and Range, and to commercial explosions and nuclear explosions that occurred at or near the Nevada Test Site (NTS).

P/S low-frequency to high-frequency spectral-amplitude ratios (spectral ratios) are chosen because they are widely used short-period discriminants. High-frequency (3–8 Hz) *P/Lg* amplitude or spectral ratios are considered among the most promising regional distance seismic discriminants (e.g., Bennett and Murphy, 1986; Evernden *et al.*, 1986; Taylor and Randall, 1989; Baumgardt and Der, 1994; Walter *et al.*, 1995; Goldstein, 1995; Taylor, 1996; Hartse *et al.*, 1997; Kim *et al.*, 1997). When using these discriminants, explosions are expected to have higher *P/S* ratios than earthquakes (Walter *et al.*, 1995), however, these results may vary with the tectonic region, frequency, and seismic phases used.

The Mogul sequence occurred in the western US (WUS), in a region which, because it includes the area of the Nevada Test Site (NTS), has been the location of numerous discrimination studies.

Three seismic phases were most studied in the WUS: 1) *Pn*, a phase observed to be slower (7.5-7.9 km/s) in the western Basin and Range, beneath the Sierra Nevada (Tibuleac and Herrin, unpublished study at TXAR; Evernden, 1967); 2) *Pg*, a phase well-observed up to 1000 km from nuclear explosions at NTS at 6 km/s (Evernden, 1967) and 3) *Lg*.

Lg spectral ratios were found to be the best of all regional phase discriminants in the western US (Taylor *et al.*, 1988, Taylor and Randall, 1989), for NTS explosions and WUS earthquakes recorded at broadband stations at 200-400 km distance, in the magnitude range of 2.5 to 6.5. In other regions, however, these ratios were not as effective. Other relatively successful ratios used were (1-2 Hz)/(6-8 Hz) spectral ratios of *Pn*, *Pg*, and *Lg*. The *Pn* spectral ratios showed the least separation between populations. Lynnes and Baumstark (1991) investigated *Pg* and *Lg* (1-2 Hz)/(4-8 Hz) spectral ratios for signals recorded at Jamestown, California, and found that *Lg* spectral ratios worked better than *Pg* spectral ratios. Taylor, 1996, found that the *Pg/Lg* spectral ratio discriminant was effective and displayed improved separation between earthquakes and explosions as frequency was increased. The high-frequency *Pn/Lg* or *Pg/Lg* discriminant appeared to perform well in every region and showed a marked improvement over the *Pg/Lg* ratio taken at around 1 Hz (e.g. Walter *et al.*, 1995; Baumgardt and Young, 1990; Chan *et al.*, 1990; Dysart and Pulli, 1990; Chael, 1988). The main drawback of the *Pg/Lg* discriminant was low signal-to-noise ratio and increased propagation effects at higher frequencies. Walter *et al.*, (1995) using Nevada Test Site (NTS) explosions and earthquakes located on the NTS found that, at 6 to 8 Hz, *Pn/Lg* discriminated all except the shallowest earthquakes, while *Pg/Lg* discriminated all but the high gas-porosity explosions. They found that network – averaged *Pn/Lg* amplitude ratios (6-8 Hz) plotted versus

$M_L(\text{coda})$ fairly well separated events with $M_L(\text{coda}) \geq 3.5$ barring one significant outlying shallow earthquake at Rock Valley. All the spectral ratios showed dependence on magnitude and for P/Lg ratios at (1-2 Hz)/(6-8 Hz), none performed well at distances greater than 200 km below magnitude 3.5.

Multiple factors influence the discriminants and corrections may be implemented to improve their performance. Walter *et al.*, 1995 found that the source effects which most influenced the discriminants in their study were depth for the earthquakes, and the source medium properties of gas porosity, density, and velocity for the nuclear explosions. Of the spectral ratios, Lg-coda performed the best, at least in part because of its extremely small interstation variability, discriminating all but the low gas porosity explosions. The best discriminant performance was given by combining phase and spectral ratios. A sum of the logarithmic values of Pn/Lg , Pg/Lg , and the Lg coda discriminated all but two of the shallowest earthquakes. Xie and Patton, 1999, found that Pn/Lg were dependent on magnitude, thus they implied a possible dependence of the discriminant on source scaling.

Scatter in regional discriminant measurements associated with varying path propagation effects was typically suppressed by empirical means such as distance corrections (either based on direct data interpolations or models constructed to match data), attenuation corrections (Taylor *et al.*, 2002, Pasyanos and Walter, 2009), spatial averaging of event populations by cap averaging or kriging (e.g., Hartse *et al.*, 1998; Phillips *et al.*, 1998; Schultz *et al.*, 1998; Rodgers *et al.*, 1999; Phillips, 1999), or regression on wave-guide parameters such as crustal thickness, sediment thickness, and elevation measures (e.g., Zhang *et al.*, 1994; Fan and Lay, 1998a,b,c). Zeiler and Velasco (2009) developed local ($d < 200$ km) amplitude discriminants using earthquakes, single-fired explosions, and delayed-fired explosions and found that magnitude and amplitude ratios are effectively used to discriminate between small earthquakes and explosions at local distances, with each performing the best in the hard-rock lithology. They also found that source lithology, local site effects, and large-scale geologic features controlled most of the variability in the amplitude measurements. Mayeda and Walter, 1996, found that shallow (depth < 5 km) earthquakes, collapses and nuclear explosions showed anomalous spectral peaking in the 0.2 – 0.4 Hz frequency range of coda waves, relative to deeper earthquakes.

Low- to high-frequency spectral-amplitude ratio discriminants are tested in this subtask on each of the phases Pn , Pg and Lg for the Mogul earthquakes and for earthquakes and explosions within 600 km of the main shock epicenter. For reference, we apply the method to earthquakes and explosions on, or near the NTS. The results of this study are compared to findings of major discrimination studies in Nevada.

DATA

A number of earthquakes and commercial explosions that occurred near Reno from 2005 to 2013 were used, as well as nuclear explosions and earthquakes that occurred near the NTS from 1988 to 1992 (Table 9). The earthquakes ranged from about 1 to 15 km in depth and displayed a variety of focal mechanisms, in a magnitude range M_L from 2.5 to 5.6. The nuclear explosions were kindly provided by Dr William Walter from Lawrence Livermore National Laboratory (Walter *et al.*, 2004). One of the challenges in our study is that the available commercial explosions in the Reno area are small ($M_L < 2.5$). Numerous Mogul earthquakes, however, have magnitude less than 4. This is why Mogul earthquakes with M_L from 1 to 4.7 were selected for analysis.

We analyzed data at station-event distances from 40 to 500 km, as shown in Table 10. These events were recorded at seven broadband and short-period digital seismic stations. Station MNV has been replaced with the co-located broadband station NV31, thus waveforms recorded at both stations have been used, after the instrument removal. Earthquakes and nuclear explosions on or near NTS are also used at stations CMB, MNV and ELK. Waveforms from these events have different travel paths than the events in northeast Nevada and this is why the results from these event categories may be comparable only against each other. An attempt was made to correct for the path following Phillips and Stead (2008), i.e. using the Walter and Taylor (2001) Q values for paths south of the parallel 38° N, however, using higher, $Q_{OLg} = 220$ (and proportional values for Q_{OPn} and Q_{OPg}) for paths beneath the Sierra Nevada and lower, $Q_{OLg} = 180$ for paths from Reno to ELK. Only the Q values were changed, the other parameters in Walter and Taylor (2001) were kept the same. At local stations WAK, WIL, WVA and YER the proximity of recent earthquake epicenters to the Mogul epicenter makes it possible to study the discriminant under conditions of relatively similar paths and common recording sites, thus focusing on source differences.

Sample waveforms of a similar magnitude crustal earthquake, a Mogul earthquake, a subcrustal Rock Valley earthquake, and a nuclear explosion in the frequency bands used in this study, recorded at MNV are shown in Figure 43. In the 6-8 Hz band, where P , S , and Lg amplitudes are often measured to form discrimination plots, the Mogul earthquake, the Rock Valley earthquake and the explosion are lacking S - and Lg -waves. Further, these events have similar impulsive P -waves. Thus, on standard high-frequency P/S or P/Lg discrimination plots, sub-crustal earthquakes sometimes merge into explosion populations.

METHOD

We compared the P/S discriminants applied on the Mogul earthquakes to results obtained using commercial explosions, nuclear explosions, and earthquakes. Pn , Pg , and Lg pseudo-spectral ratios were computed as in Taylor, 2002. For amplitude ratios in a particular frequency band, the instrument effect canceled. However, for ratios involving measurements in different frequency bands, knowledge of the instrument response was critical. Thus, for each event-station pair, the instrument-corrected spectra were calculated from windowed Pn , Pg , and Lg phases.

Group velocity windows are defined by t_1 and t_2 , where $t_1 (Pn) = \Delta/8$ and $t_2 (Pn) = \Delta/6.1$ for the Pn phase, $t_{1Pg} = \Delta/6.05$ and $t_{2Pg} = \Delta/5.0$ for the Pg phase, and $t_1 (Lg) = \Delta/3.65$ and $t_2 (Lg) = \Delta/3.0$ for the Lg phase (where Δ is the epicentral distance in km). Unlike previous studies, the Pn arrivals were not manually picked. Pn is a late arrival in the western Great Basin (WGB) and is seldom visible and easy to pick (mostly on east-west paths). If the energy of the waveforms in the Pn window met the condition $SNR > 1.4$, the value was considered for ratio estimation.

Noise spectra are calculated in a 30 second window preceding the Pn arrivals or, for shorter epicentral distance, starting at the earthquake origin and ending at 8.1 km/s time lag.

At a particular station, we assume the instrument-corrected amplitude spectrum for a given phase, $A_i(f)$, for source i , is given by

$$A_i(f) = G(r, r_o) S_i(f) P(f) \exp(-\pi * f * r_i / (Q(f) \mu)) \quad (14)$$

where $S_i(f)$ is the source spectrum (Taylor *et al.*, 2002, equation 5), r is the epicentral distance, f is the frequency, $Q_i(f)=Q_0 f^\gamma$ is the frequency-dependent attenuation (γ was chosen like in Walter and Taylor, 2001), μ is the group velocity, $P(f)$ is a unitless phase site/excitation factor, and $G(r,r_0)$ is the frequency-independent geometrical spreading (Street *et al.*, 1975) given by

$$\begin{aligned} G(r) &= r^{(-1)} & r < r_0 \text{ or} & & (15) \\ G(r) &= r_0^{(-1)} (r_0/r)^{(n)} & r_0 \geq r & \end{aligned}$$

where r_0 is a transition distance from spherical spreading to the spreading rate n .

Corrections for the attenuation factor Q for each phase used *MDAC* parameters from Walter and Taylor (2001). Because the measurements are at the same site, site corrections are not computed in this study. It is also assumed that site corrections are similar for different phases.

Corrections for the source term (Equation 6 in Walter and Taylor, 2001) assumed that the density at the source is less variable than the seismic velocity, and that corrections for the seismic velocity at the receiver were not necessary. Seismic velocity at the source varied, however, thus corrections were applied. As in Cramer and Boore, 1978, for nuclear explosions detonated at Yucca Flat the P -velocity was 1.6 km/s and for nuclear explosions detonated at Pahute Mesa the P -velocity was 2.7 km/s. The S -velocity was calculated from the P -velocity assuming the Poisson ratio to be 0.25. For the Mogul earthquakes, the P -velocity was 5.13 km/s and the S -velocity was 2.9 km/s. For the other events, a set of crustal velocity models in the western Basin and Range were used. These models were estimated in studies of seismic signal and ambient noise (Tibuleac *et al.*, 2011).

After instrument, geometrical spreading, attenuation and source velocity corrections, each phase pseudo-spectra (Taylor *et al.*, 2002) was measured using the entire phase window. The *rms* amplitudes were converted to spectral values using Parseval's theorem (Taylor *et al.*, 2002). Corrections were applied (Taylor *et al.*, 2002) when different length noise and signal windows were available. The phase pseudo-spectra was estimated as the square of the sum of the pseudo-spectra of vertical and horizontal components minus the same estimate for the noise. In order to reduce the noise effect on the signal spectra, only those frequencies for which the signal-to-noise ratio (*SNR*) level was greater than 1.4 were selected (using the pre - *Pn* noise). The minimum *SNR* level was higher in other studies (usually *SNR* > 2), however, in this study the threshold was lowered to allow the use of lower magnitude explosions and earthquakes. Thirteen different frequency bands were selected, based on previous successful outcomes of *P/S* discriminants in western US: 0.2-0.5; 0.5-1; 1-2; 2-3; 3-4; 4-6; 6-8; 8-10; 10-12; 12-16 and 4-10 Hz. Waveforms were filtered using a Butterworth, zero – phase, eight pole filter. Some of the frequency bands were available only at selected stations, depending on the sample rate. Eleven spectral ratios are calculated for *P/Lg* and for *Lg* at low and high frequency.

Base-ten logarithms of the eleven spectral ratios are plotted next as a function of a *Pg*-based magnitude measure. *Pg* was observed at all stations, and the maximum *Pg* amplitude was picked within the first 10 seconds of the arrival, or within $t1_{Pg}$ and $t2_{Pg}$. *Pn* and *Lg* were identified only at some of the stations. A

magnitude measure related to Pg was estimated, m_{Pg} , which related $\log_{10}(A_{Pg})$ to M_L through the results of a regression:

$$M_L - \log_{10}(A_{Pg}) = a \log_{10}(\Delta) + b \quad (16)$$

where A_{Pg} was the Pg zero-to-peak maximum amplitude (nm) in the first 10 seconds after 6.1 km/s time lag, and Δ is the epicentral distance in km. The m_{Pg} magnitude formula,

$$m_{Pg} = \log_{10}(A_{Pg}) + a \log_{10}(\Delta) + b + C \quad (17)$$

was calibrated against M_L and station correction constants (C) were estimated (Table 10). M_L is the Richter magnitude formed by convolving the waveforms with the frequency response of a Wood-Anderson instrument and is the network magnitude used at the Nevada Seismological Laboratory (NSL).

RESULTS

Cross-spectral (P/Lg) and same phase (Lg) pseudo-spectral ratios have been estimated for the stations in Table 10, for configurations of events shown in Figure 44. Figure 45 shows estimates of the parameters in Equation 16 at the 4 closest stations in Table 10. Figures 46 – 47 show the $\log_{10} P/Lg$ and Lg ratios for the different frequency bands at the 3 furthest stations. Figure 48 shows minor differences between the base –ten logarithmic ratio representation as a function of $\log_{10}(A_{Pg})$ and the representation as a function of m_{Pg} magnitude at station MNV. Only minor differences are observed the other stations as well.

Relatively better earthquake-explosion separation is observed at all stations for Pn/Lg and Pg/Lg ratios at 6-8 Hz. This was also noted by Taylor *et al.*, (1989) and by Walter *et al.*, (1995). The high-frequency Pn/Lg ratio shows similar separation as the Pg/Lg ratio. However, because of poor signal to noise for the Pn phase, the ratio was measured for only a limited number of events at stations MNV, ELK and CMB. The Lg spectral ratio taken in the 1 to 2 and 6 to 8 Hz frequency bands shows good separation between the earthquakes and explosions (similar to that observed by Taylor *et al.*, 1988). Except for a few, the small ($M_L < 2$) earthquakes observed the local stations separated from commercial explosions. The commercial explosions in the Reno Area, however, have most of the energy in the later part of the Sg wave train (after 3 km/s time lag).

One of the limitations of the high-frequency discriminants is that the performance is improved at high frequencies, but propagation effects can significantly reduce the number of high-frequency measurements. Accounting for propagation effects through regions with different attenuation improved the event separation at all stations. A comparison of the results with uniform attenuation factor Q and with Q variable as a function of tectonic region (see Method section discussion) at stations ELK and MNV was shown in Figure 49. To reach ELK and MNV, the Mogul and vicinity events have significantly different propagation paths than the paths of the events near or on the NTS. Figure 49 a and c show improved discrimination at higher frequency for the P/Lg spectral ratios at ELK and MNV, when phase

attenuation coefficients are chosen as a function of the propagation path as opposed to the case when the Walter and Taylor (2001) attenuation coefficients (Q) are used for all the events (Figure 49, insets b and d). A possible explanation is that higher frequencies are most affected by small (in this case 10%) changes in Q . Based on these results, variable attenuation was applied for all stations and all the results presented here are for variable Q .

The choice of the seismic velocity model at the source, through the source correction, also affected the ratios. Similarly, Gupta *et al.*, (1992) concluded that the higher-frequency L_g in the 3 to 7 Hz passband was dependent on source medium velocity. They hypothesized that for explosions detonated in low-velocity media, more energy from the free-surface pS conversion is trapped in the crust, enhancing L_g amplitudes. Taylor and Denny (1991) showed that there was a strong material dependence on the spectral shape that caused complications with the nuclear explosion ratios. The rate of high-frequency decay was greater for nuclear explosions detonated in rocks having high gas filled porosity, resulting in a higher spectral ratio (and better separation from the earthquakes).

CONCLUSIONS

Investigations of the P/S_g and the P/L_g discriminant in the western Great Basin show that the Mogul earthquakes can be distinguished from commercial and nuclear explosions even for small magnitude ($M_L < 2$) events. Pseudo-spectral amplitude ratios are estimated for earthquakes and explosions near Reno Nevada and compared to ratios of earthquakes and explosions on or near the NTS. The ratios are investigated at seven seismic stations.

The best earthquake – explosion separation was observed for P_g/L_g ratios at 6-8 Hz, and for L_g spectral ratios taken in the 1 to 2 and 6 to 8 Hz frequency bands, similar to previous observations in Nevada. Mogul earthquakes do not separate from deeper earthquakes when the above spectral ratios are estimated.

The good separation between earthquakes and explosions for the spectral ratio discriminant varies at each station. Different ratios perform better with greater station-event distance. For good performance, this type of discriminant requires knowledge of the attenuation characteristics and of the source seismic velocity model. As different frequency ratios perform best depending on station, combinations of P/S ratios at more stations may improve discrimination.

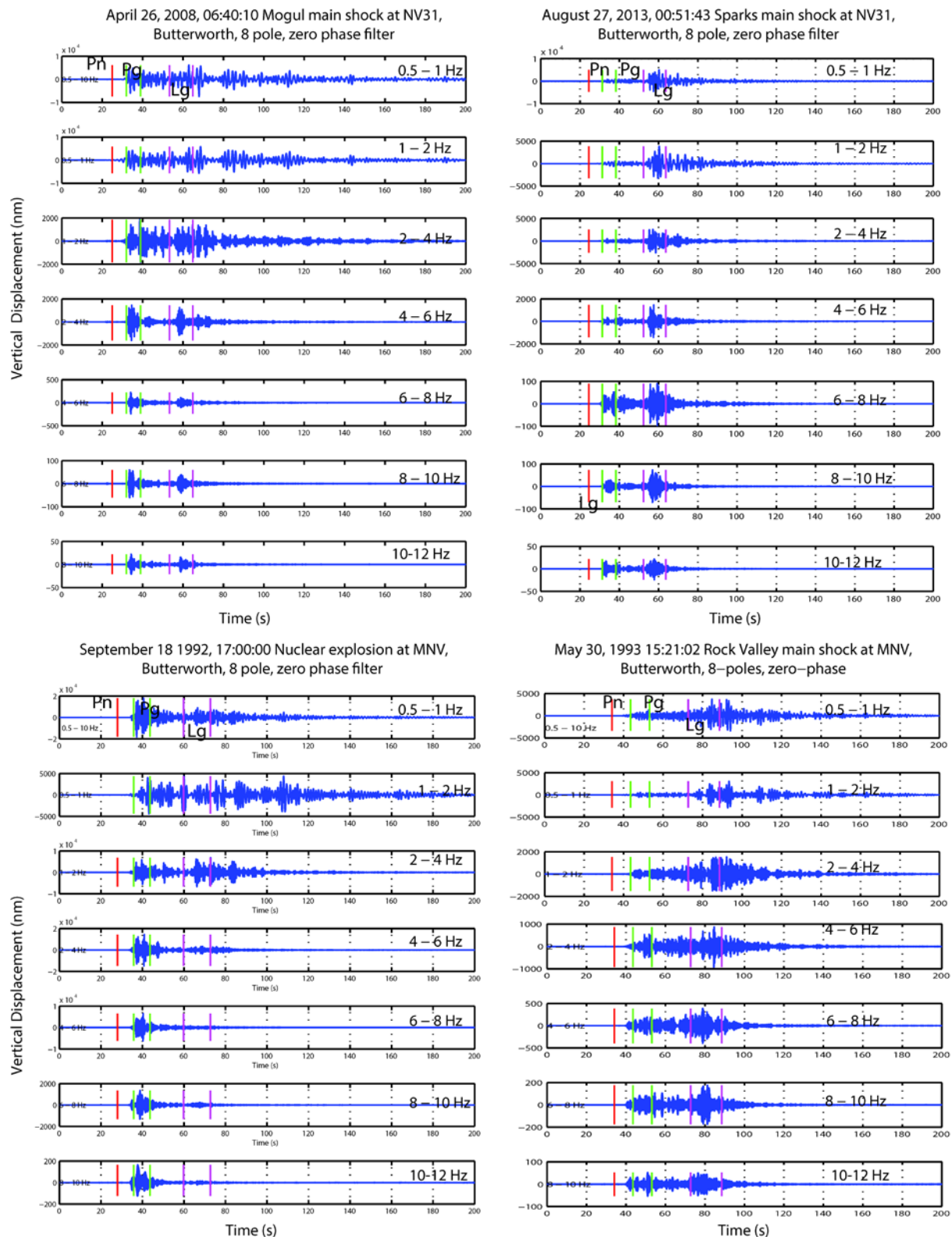


Figure 43. Example of bandpass-filtered seismograms, with a Butterworth, zero-phase, eight pole filter, from four events used in this study. The events were recorded at station MNV and are, from left to right: a normal-depth Sparks, Nevada main shock (3.9 ML -8-km depth), the Mogul, Reno NV main shock (4.7 ML, 2.8 km depth), the shallow Rock Valley mainshock (3.8 ML, 3-km depth), and an NTS explosion (3.7 ML, 0.3-km depth). Vertical lines indicate the start and finish of the analysis windows used for each of direct regional phases Pn, Pg, and Lg. The numbers on the right indicate the passband of the filtered data and the multiplicative factor applied before plotting. Note the similarity of the Mogul earthquake and the nuclear explosion. The frequency bands are in order from the top to the bottom: 0.5-10 Hz, 0.5-1 Hz, 1-2 Hz, 2-4 Hz, 4-6 Hz and 6-8 Hz.

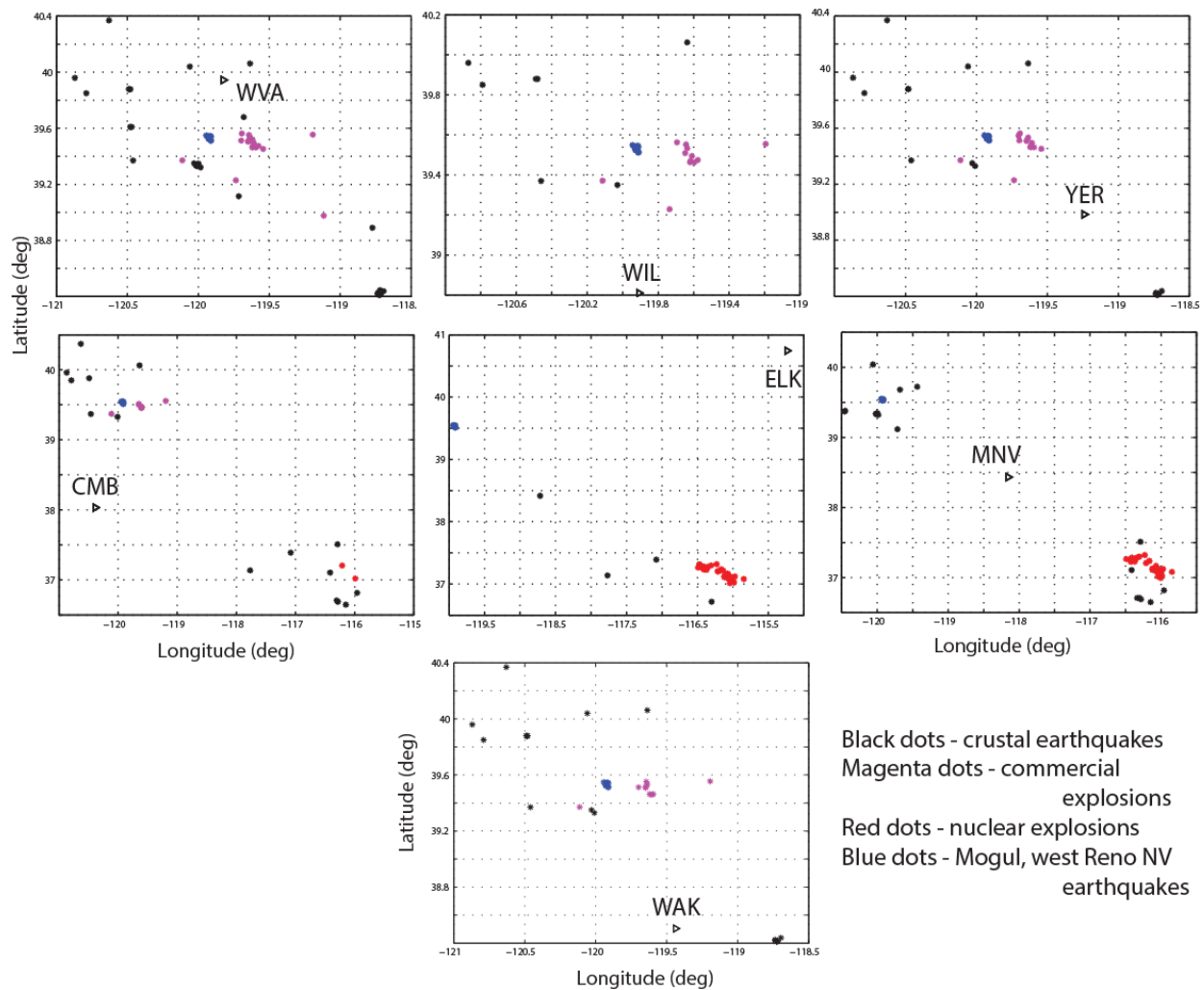


Figure 44. Locations of events recorded at Basin and Range seismic stations. *Black dots are crustal earthquakes, blue dots are Mogul earthquakes, red dots are nuclear explosions and magenta dots are commercial explosions. The black triangles show station locations.*

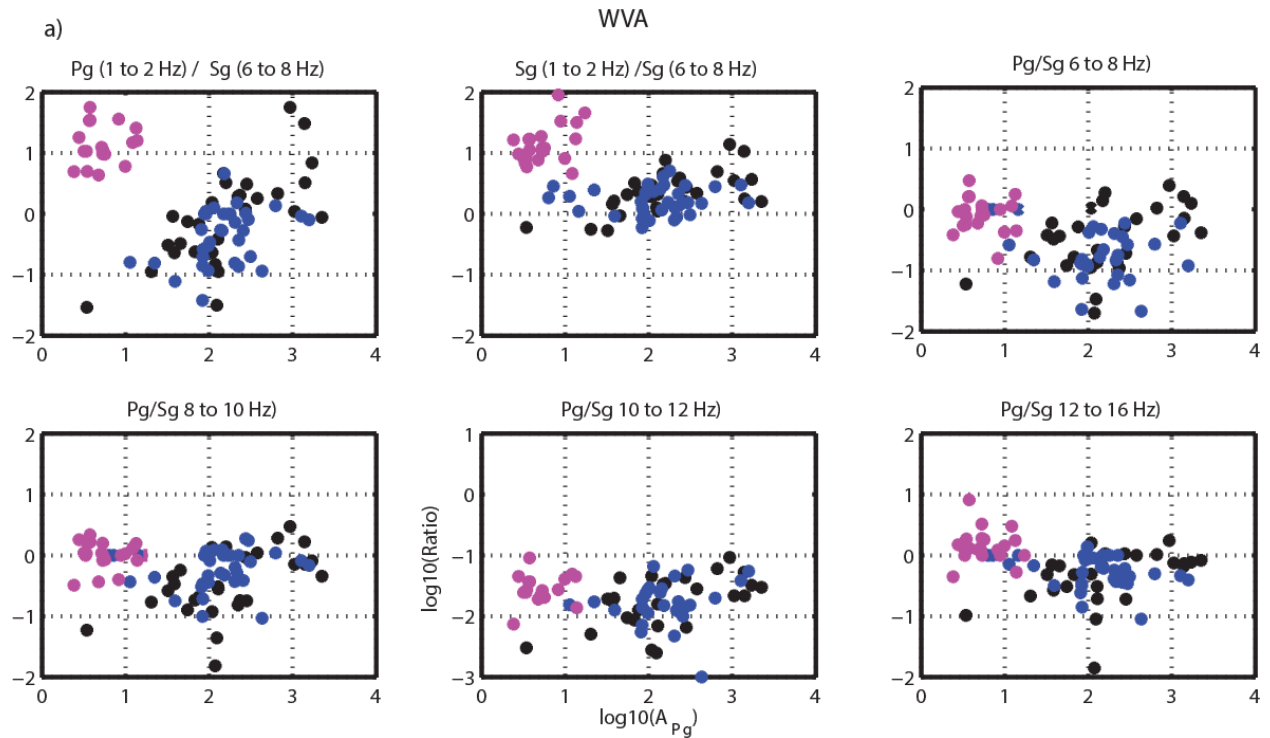


Figure 45. \log_{10} Pg/Sg and S spectral ratios for events recorded at Basin and Range seismic stations at distances less than 200 km, as a function of $\log_{10}(A_{Pg})$. Black dots are crustal earthquakes (depth > 5 km), blue dots are Mogul earthquakes and magenta dots are commercial explosions. Figure 45a shows P/S ratios at WVA. Figure 45b shows P/S ratios estimated at WIL. Figure 45c shows ratios estimated at YER and Figure 45d shows ratios estimated at WAK.

b) WIL

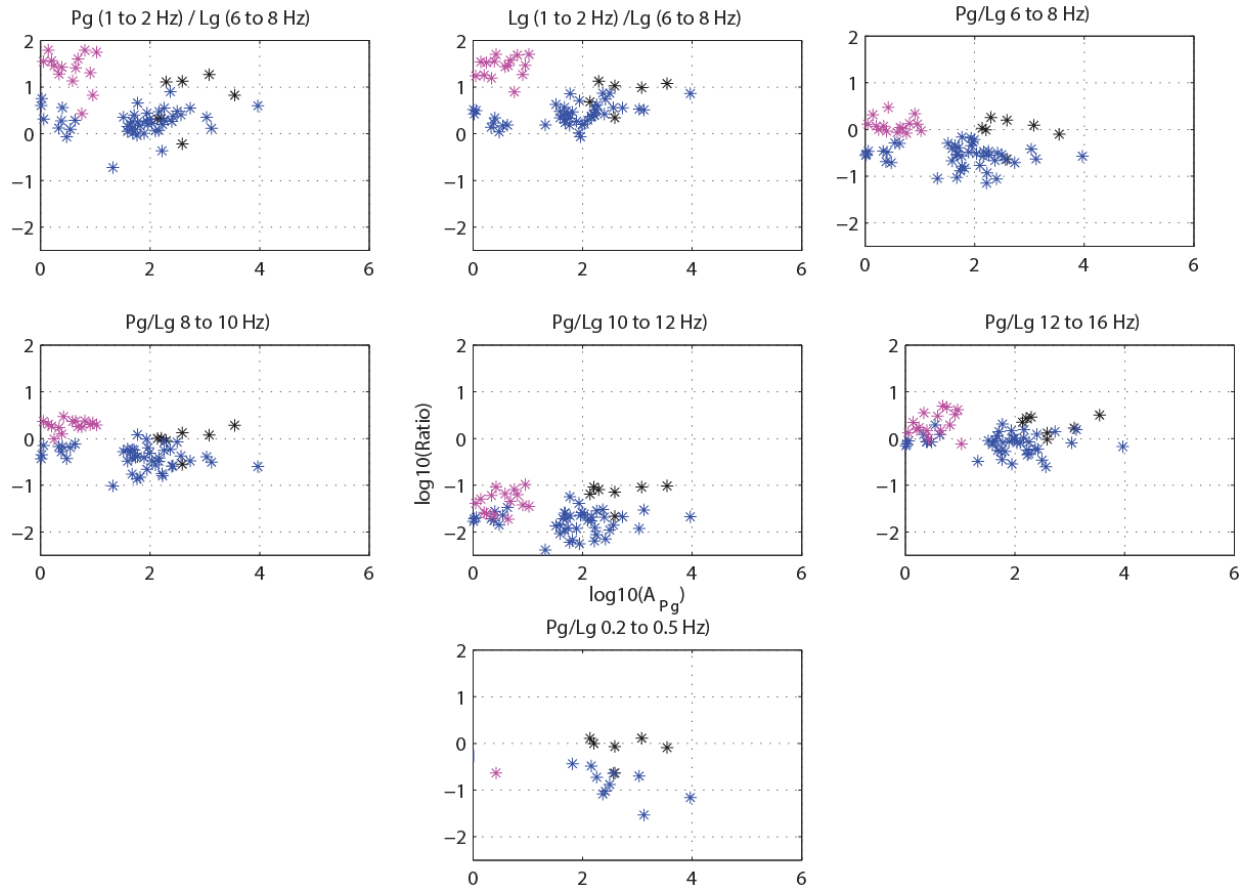


Figure 45. Continuation

c)

YER

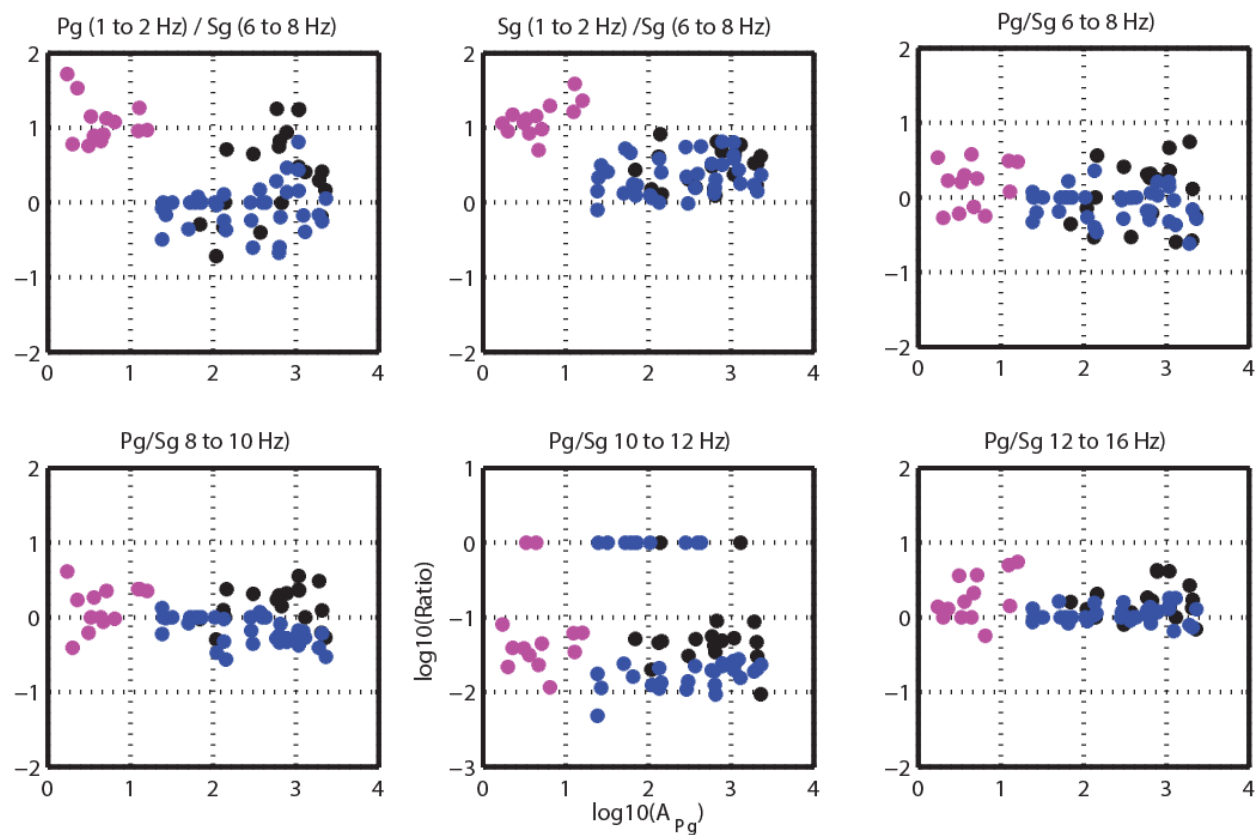


Figure 45. Continuation

d) WAK

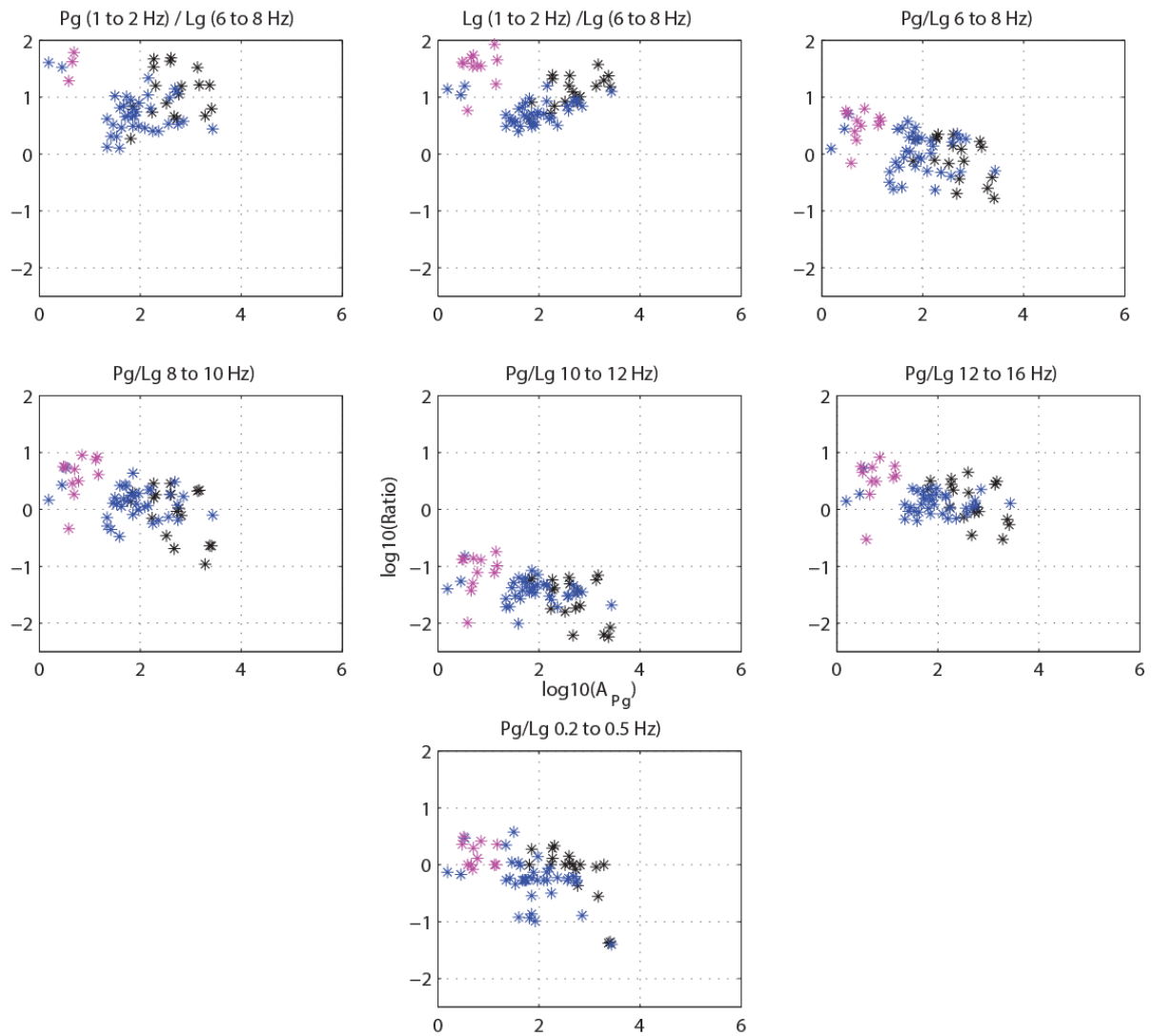


Figure 45. Continuation

a) CMB

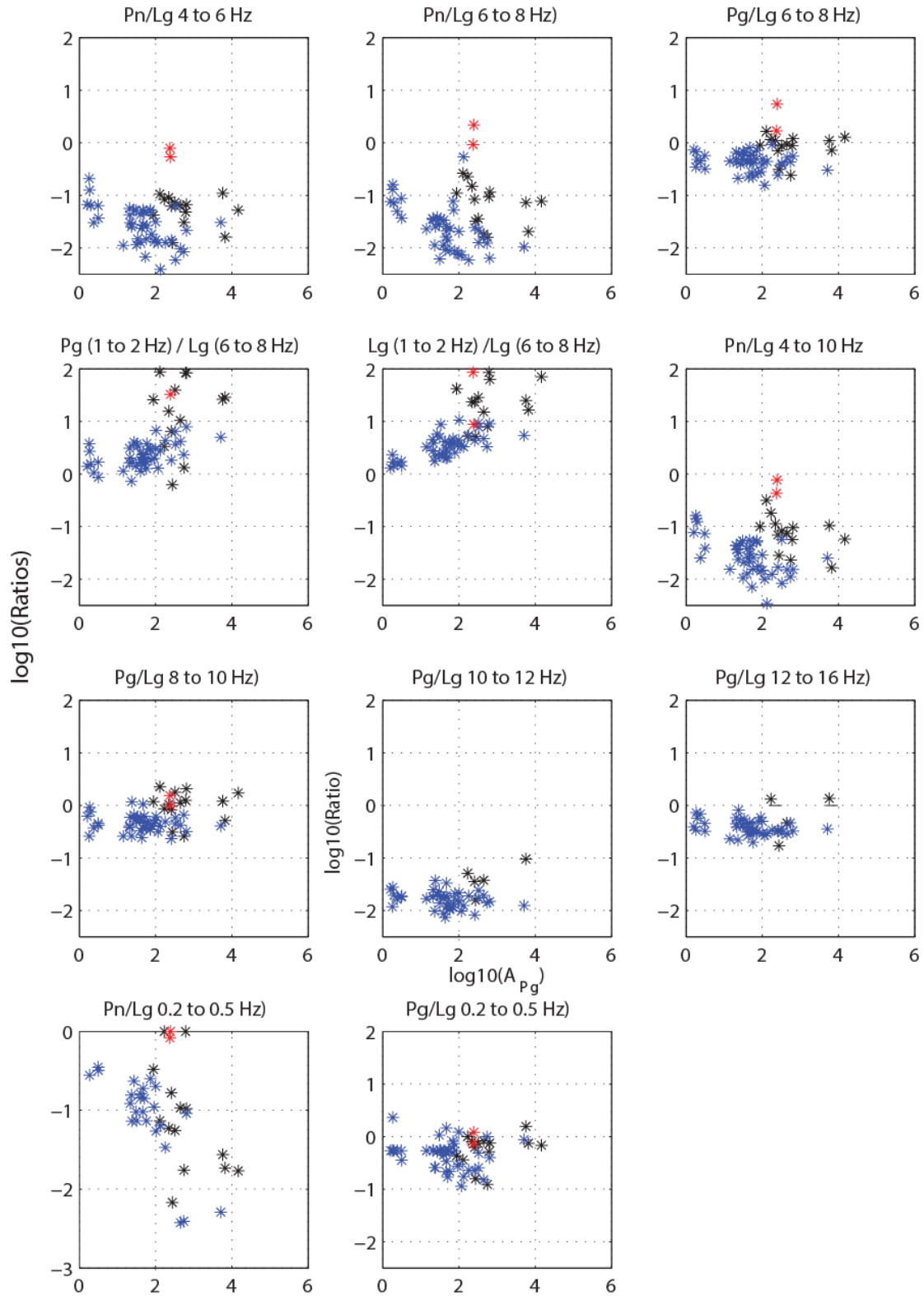


Figure 46. Base-ten logarithm of Pg/Lg ratios for events recorded at Basin and Range seismic stations at distances greater than 100 km. Black dots are crustal earthquakes (depth > 5 km), blue dots are Mogul earthquakes, red dots are nuclear explosions (where recorded) and magenta dots are commercial explosions. Figure 1a shows P/S ratios at CMB. Figure 1b shows P/S ratios estimated at ELK and Figure 1c shows ratios estimated at MNV.

b) ELK

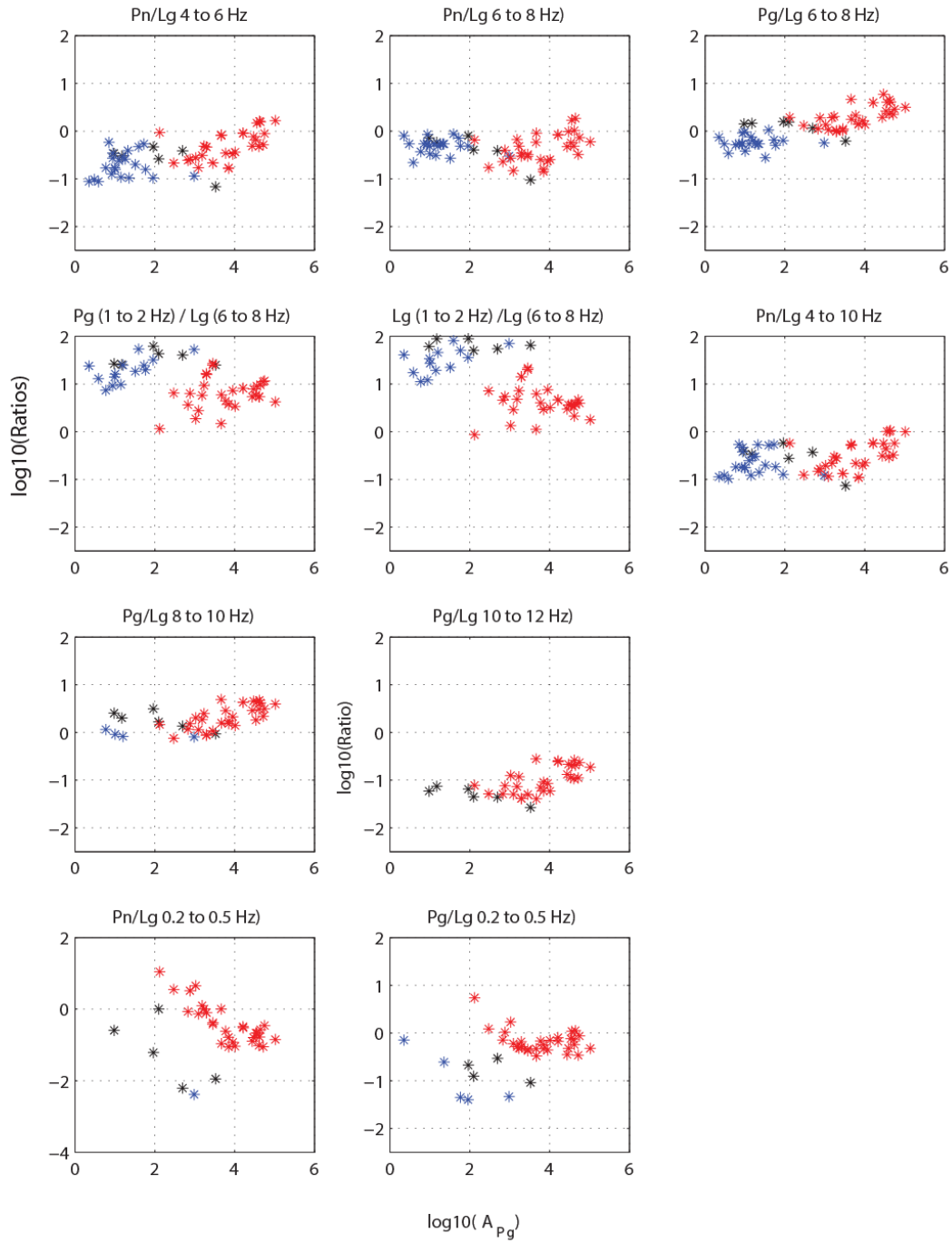


Figure 46. Continuation

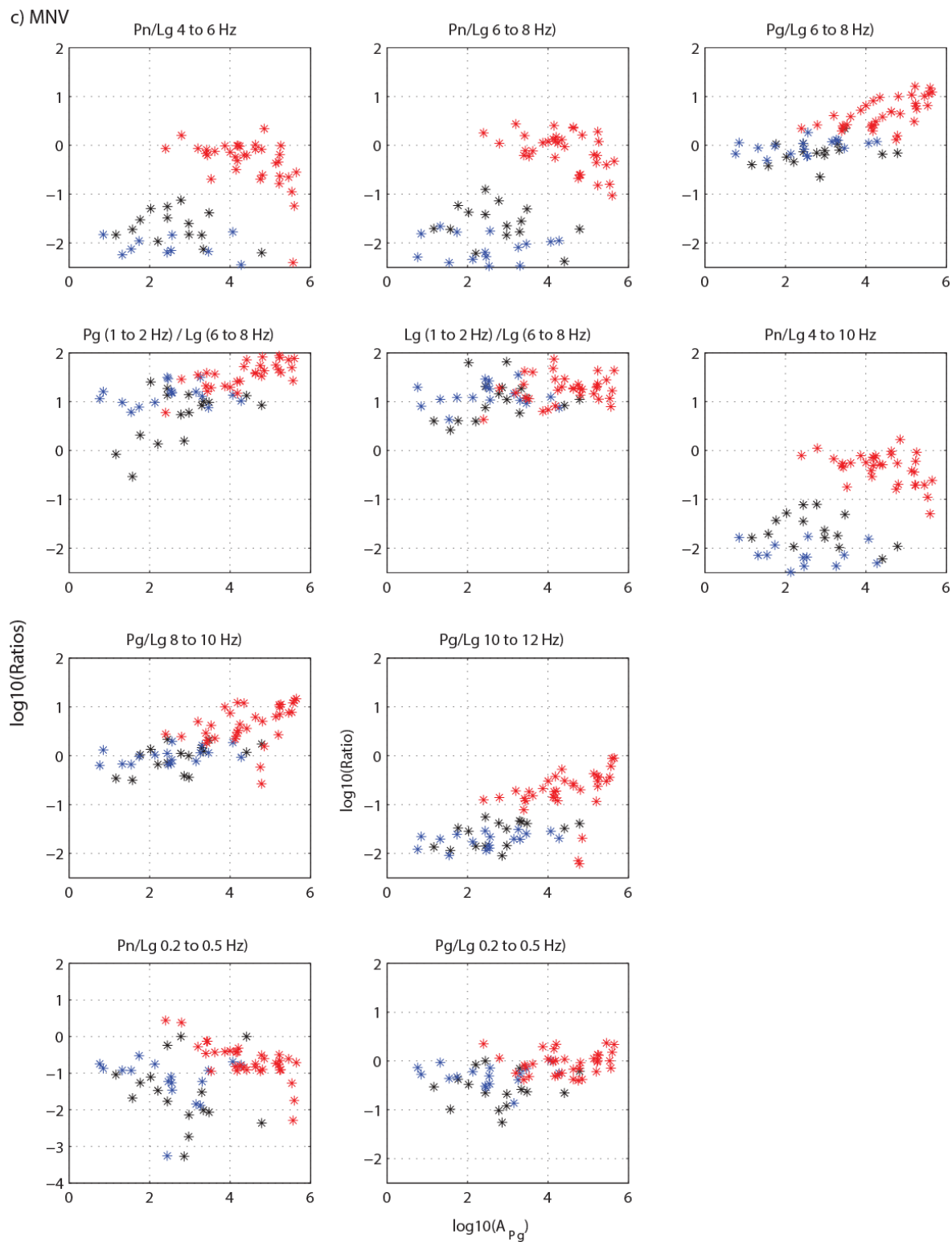


Figure 46. Continuation

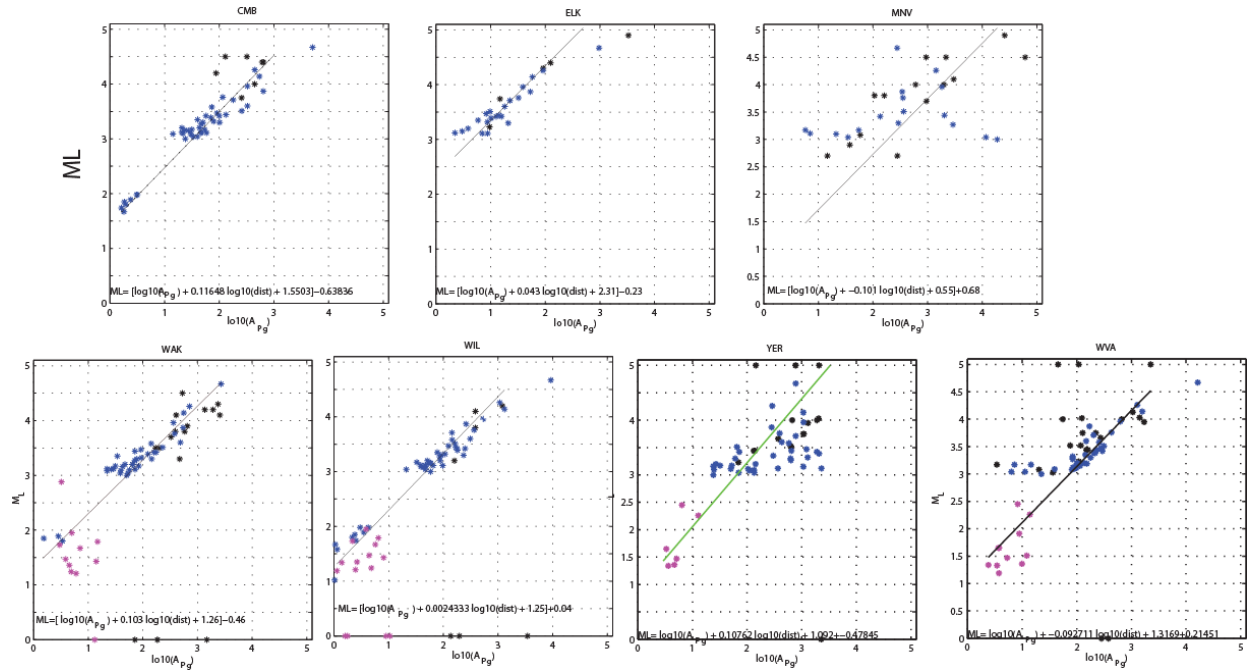


Figure 47. M_L - $\log_{10}(A_{pg})$ as a function of a $\log_{10}(\Delta) + b$ at each station. Black dots are crustal earthquakes (depth > 5 km), blue dots are the Mogul earthquakes and magenta dots are commercial explosions (where recorded) and magenta dots are commercial explosions. The results of this regression are also shown in Table 10.

ELK

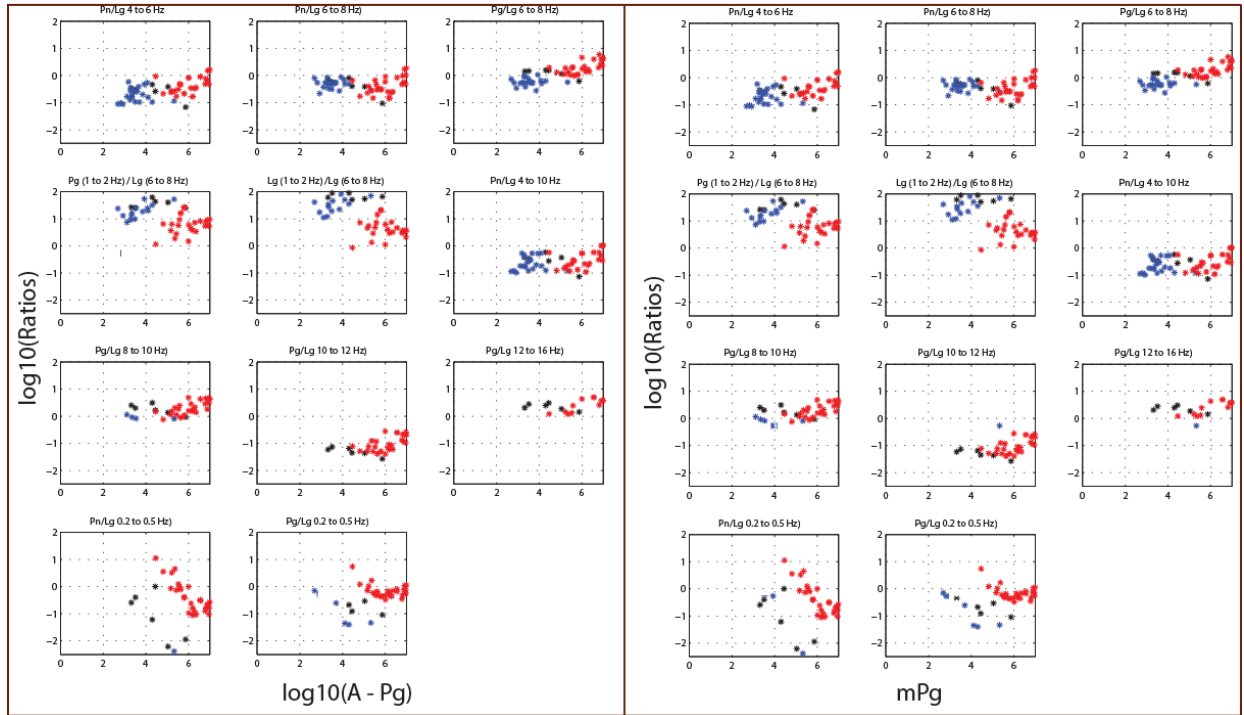


Figure 48. A comparison of the base-ten logarithm of the P/Lg ratios for events recorded at ELK, as a function of $\log_{10}(A_{Pg})$ and m_{Pg} . The differences are barely visible. Black dots are crustal earthquakes (depth > 5 km), blue dots are Mogul earthquakes and red dots are nuclear explosions.

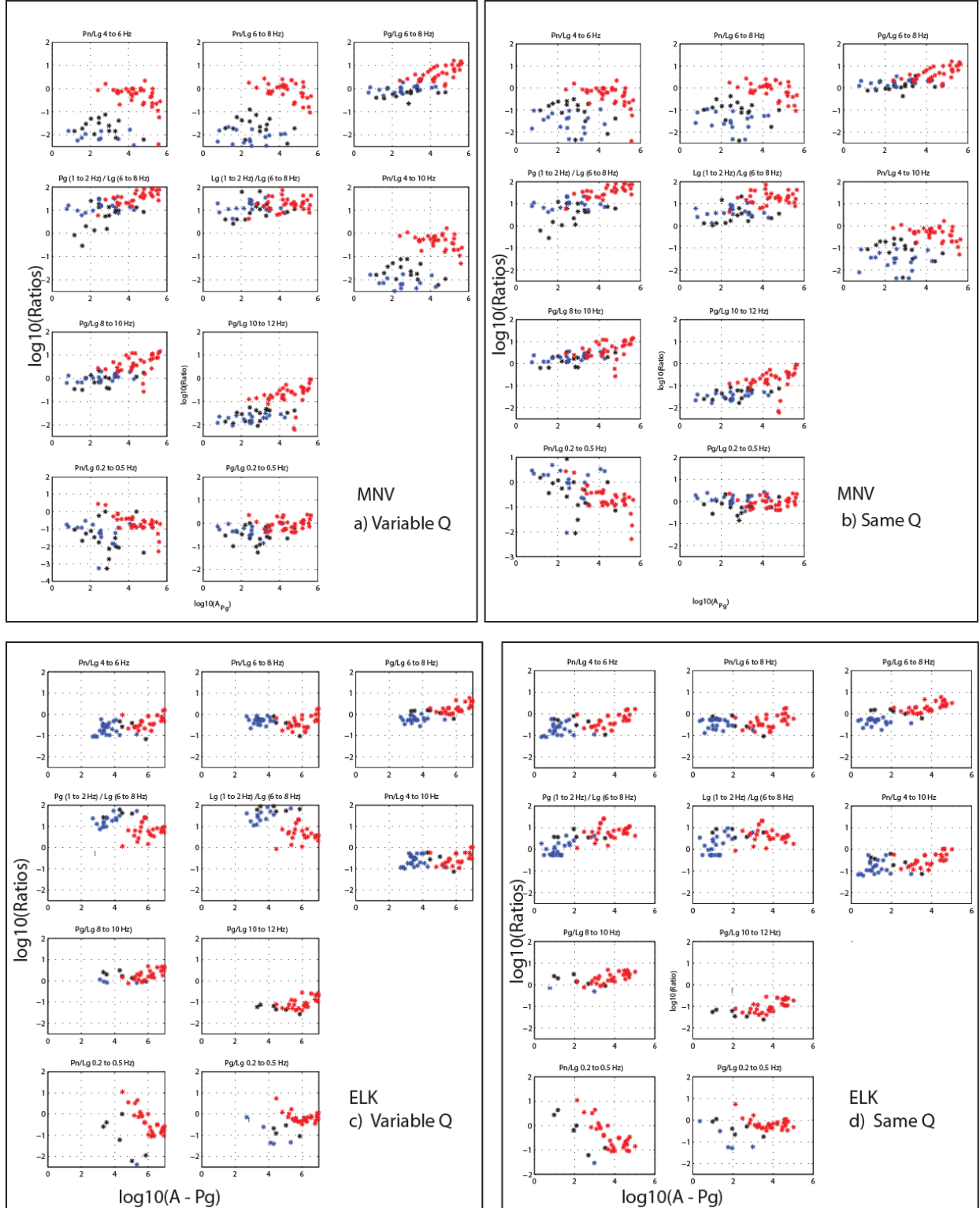


Figure 49. Comparison of the base-ten logarithm of the spectral ratios estimated in the case when the attenuation coefficient Q was variable (inset a) for the propagation region and the same Q was applied (inset b). Note better separation for the case when Q varies on each set of propagation paths.

Table 9. List of earthquakes, and commercial and nuclear explosions used in this study

MM	DD	YYYY	JJ	HH	MM	SS	LAT	LON	DEPTH	M _L
MOGUL 2008 EARTHQUAKES										
4	28	2008	119	12	12	31.23	39.5314	-119.9312	1.4940	3.0000
5	31	2008	152	9	9	56.83	39.5438	-119.9226	3.6750	3.0400
4	27	2008	118	18	31	10.6	39.5268	-119.9277	1.8380	3.0400
4	21	2008	112	19	14	10.44	39.517	-119.915	2.8190	3.0800
4	26	2008	117	14	35	29.19	39.5154	-119.9135	2.9620	3.0900
11	13	2008	318	7	42	8.49	39.5451	-119.9344	3.0890	3.1000
6	17	2008	169	14	1	49.19	39.5262	-119.9268	3.7550	3.1100
4	29	2008	120	16	14	59.86	39.529	-119.924	1.0310	3.1100
3	24	2008	84	19	16	14.22	39.5278	-119.9285	2.6460	3.12
4	26	2008	117	14	47	37.3	39.5113	-119.9115	2.5530	3.1200
3	27	2008	87	3	42	14.29	39.5286	-119.9291	2.7170	3.1500
4	29	2008	120	5	51	5.52	39.5127	-119.9122	3.4600	3.1600
6	10	2008	162	0	18	34.91	39.54	-119.9115	1.2630	3.1700
6	8	2008	160	10	13	58.62	39.5448	-119.9158	1.7470	3.1700
4	29	2008	120	6	1	53.58	39.5143	-119.9107	3.2000	3.2000
4	15	2008	106	21	26	35.28	39.5328	-119.9255	2.6210	3.2000
4	25	2008	116	1	0	33.46	39.5248	-119.9204	2.5670	3.2700
7	29	2008	211	10	34	42.11	39.5493	-119.9446	3.6600	3.3000
4	25	2008	116	17	30	10.08	39.5255	-119.9204	2.5250	3.3000
4	27	2008	118	17	49	49.82	39.5192	-119.9145	3.2050	3.3200
3	8	2008	68	10	7	0.33	39.5231	-119.927	1.9980	3.3500
4	26	2008	117	6	43	50.8	39.521	-119.9157	2.1180	3.3800
4	15	2008	106	14	59	37.35	39.5327	-119.9262	2.8550	3.3900
4	15	2008	106	21	32	31.8	39.5318	-119.925	2.5410	3.4200
5	15	2008	136	13	44	48.43	39.5407	-119.9159	2.3590	3.4200
4	26	2008	117	9	11	59.83	39.5265	-119.9171	1.9860	3.4400
4	26	2008	117	15	20	40.5	39.5435	-119.9354	2.1840	3.4700
4	26	2008	117	7	29	20.12	39.5286	-119.9195	2.8820	3.5100
4	15	2008	106	21	33	57.64	39.5333	-119.9262	2.5010	3.5800
6	8	2008	160	17	53	40.64	39.5462	-119.9145	1.8930	3.6000
4	26	2008	117	1	13	20.92	39.5276	-119.9217	2.4310	3.7100
5	8	2008	129	5	55	1.6	39.5405	-119.9166	2.7190	3.7600
6	8	2008	160	17	55	19.36	39.543	-119.9148	1.8800	3.8700
4	24	2008	115	22	47	4.2	39.5299	-119.9167	4.3500	3.9600
4	24	2008	115	22	55	49	39.5299	-119.926	3.2330	4.1400
4	28	2008	119	11	33	18.21	39.5273	-119.9213	2.1290	4.2600
4	26	2008	117	6	40	10.6	39.5247	-119.918	2.6030	4.6700

Table 9. List of earthquakes, and commercial and nuclear explosions used in this study (continued)

NTS NUCLEAR EXPLOSIONS

MM	DD	YYYY	JJ	HH	MM	SS	LAT	LON	DEPTH	mb
9	23	1992	267	15	4	0	37.021	-115.989	0.34	-
9	18	1992	262	17	0	0.08	37.207	-116.211	0.385	-
6	23	1992	175	15	0	0.07	37.124	-116.032	0.29	-
6	19	1992	171	16	45	0	37.005	-116.011	0.244	-
3	26	1992	86	16	30	0	37.272	-116.361	0.622	4.2
11	26	1991	330	18	35	0.07	37.096	-116.07	0.457	-
10	18	1991	291	19	12	0	37.063	-116.046	0.457	-
9	19	1991	262	16	30	0.07	37.236	-116.167	0.264	-
9	14	1991	257	19	0	0.08	37.226	-116.429	0.658	-
8	15	1991	227	16	0	0	37.087	-116.003	0.503	-
4	4	1991	94	19	0	0	37.296	-116.313	0	4.2
3	8	1991	67	21	2	45.08	37.104	-116.075	0.475	-
11	14	1990	318	19	17	0.07	37.227	-116.372	0.594	-
7	25	1990	206	15	0	0.06	37.207	-116.215	0.389	-
6	21	1990	172	18	15	0	36.993	-116.005	0.35	-
6	13	1990	164	16	0	0	37.262	-116.42	0	4.5
3	10	1990	69	16	0	0.08	37.112	-116.056	0.469	-
12	8	1989	342	15	0	0.09	37.231	-116.41	0.601	4.2
11	15	1989	319	20	20	0.61	37.1543	-115.9792	2.54	3.65
10	31	1989	304	15	30	0.09	37.263	-116.492	0.564	-
9	14	1989	257	15	0	0.1	37.236	-116.164	0.261	-
6	27	1989	178	15	30	0.02	37.275	-116.354	0.64	-
6	22	1989	173	21	15	0.08	37.283	-116.413	0.544	-
6	22	1989	173	21	15	0.76	37.304	-116.4268	0.03	5.3
6	22	1989	173	21	15	0.8	37.283	-116.412	0	4.8
5	26	1989	146	18	7	0.02	37.086	-116.056	0.398	-
5	26	1989	146	18	7	0.16	37.0763	-115.9487	6.24	3.86
5	15	1989	135	13	10	0.09	37.108	-116.122	0.404	-
5	15	1989	135	13	9	59.93	37.094	-116.0252	3.42	4.6
3	9	1989	68	14	5	0.09	37.143	-116.068	0.5	-
2	24	1989	55	16	15	0.08	37.128	-116.123	0.37	-
2	24	1989	55	16	14	59.26	37.1208	-115.9727	2.49	4.5
2	24	1989	55	16	15	0	37.128	-116.122	0	-
2	10	1989	41	20	6	0.06	37.077	-116.001	0.503	-
2	10	1989	41	20	5	59.04	37.0803	-115.8468	3.42	5.2
2	10	1989	41	20	6	0	37.077	-116.001	0	-
12	10	1988	345	20	30	0.06	37.199	-116.21	0.4	-
12	10	1988	345	20	29	59.81	37.2133	-116.1367	2.42	5
10	13	1988	287	14	0	0.08	37.089	-116.05	0.64	4.4
8	30	1988	243	18	0	0.09	37.086	-116.069	0.489	-
8	30	1988	243	17	59	59.86	37.0922	-115.9958	2.41	5.1
8	30	1988	243	18	0	0	37.086	-116.069	0	-
8	17	1988	230	17	0	0.09	37.297	-116.307	0.616	-
8	17	1988	230	16	59	59.63	37.3197	-116.2295	0.04	5.5

Table 9. List of earthquakes, and commercial and nuclear explosions used in this study (continued)

8	17	1988	230	17	0	0	37.297	-116.307	0	4.2
7	7	1988	189	15	5	30.07	37.252	-116.378	0.622	-
7	7	1988	189	15	5	28.86	37.263	-116.2292	0.03	5.6
7	7	1988	189	15	5	30	37.252	-116.377	0	4.3
6	22	1988	174	14	0	0.08	37.166	-116.073	0.207	-
6	2	1988	154	13	0	0.09	37.26	-116.442	0.62	4.2
5	21	1988	142	22	30	0.14	37.032	-115.988	0.351	-
5	13	1988	134	15	35	0.11	37.124	-116.073	0.463	-
4	7	1988	98	17	15	0.08	37.013	-116.045	0.245	-
2	15	1988	46	18	10	0.09	37.314	-116.472	0.542	-
12	2	1987	336	16	30	0.08	37.235	-116.164	0.271	-

EARTHQUAKES NEAR RENO, NV

MM	DD	YYYY	JJJ	HH	MM	SS	LAT	LON	DEPTH	ML
1	2	1991	2	23	16	35.55	39.2203	-119.7433	5.82	4.8 (Mb BRK)
1	3	1991	3	2	8	51.92	39.2247	-119.7456	7.14	4.1 (ML BRK)
4	6	1992	97	4	1	28.45	39.6844	-119.8214	10.56	4.1
7	20	1992	202	20	9	31.7	39.32	-119.1678	4.99	4.3 (ML NEIC, BRK)
9	19	1992	263	3	17	38.87	39.7272	-120.2053	4.56	3.8 (ML USGS, NEIC)
10	20	1992	294	13	2	0.73	39.9953	-120.7956	8.88	3.7 (ML, USGS, NEIC)
2	5	1993	36	17	10	25.1	39.2228	-119.5644	3.09	3.6 (USGS, NEIC)
11	18	1994	322	20	50	58.12	39.1731	-119.69	12.93	4.4 (ML, BRK)
6	18	1995	169	22	23	23	39.8592	-120.7603	3.53	3.88
11	15	1995	319	20	33	59.21	39.6514	-120.0111	11.52	4.71
11	16	1995	320	14	59	24.68	39.6564	-120.0214	11.37	3.57
12	2	1996	337	23	33	13.03	40.0381	-119.6264	13.11	4.23
1	15	1998	15	15	12	14.01	39.4525	-120.1778	13.67	3.84
2	17	1998	48	22	8	39.14	39.9031	-120.4633	9.98	4.22
7	4	1998	185	11	18	17.67	40.1439	-119.6647	11.16	4.25
10	21	1998	294	8	31	0.93	39.7686	-120.6753	16.03	4.31
10	30	1998	303	9	53	30.46	39.3039	-119.9878	10.53	5.22
6	15	1999	166	7	50	14.34	39.7619	-120.5728	16.37	4.68
6	15	1999	166	7	51	47.6	39.7631	-120.5719	13.28	4.46
11	24	1999	328	7	45	23.07	39.9581	-120.4847	9.47	3.92
12	27	1999	361	9	44	4.48	39.9633	-120.4781	12.96	0
7	20	2010	201	21	48	30.26	40.0621	-119.6365	13.138	4.2
1	17	2011	17	7	10	12.337	39.874	-120.4775	8.7038	3.86
3	24	2011	83	21	20	39.738	40.0604	-120.0474	10.9669	3.76
12	6	2013	340	20	20	19	39.348	-119.9992	12	3.0 (ML ANF)
6	3	2004	155	8	54	45	39.3146	-119.9506	8.3	4.5
6	26	2005	177	18	45	57.79	39.31	-120.09	0.09	-

Table 9. List of earthquakes, and commercial and nuclear explosions used in this study (continued)

5	29	2006	149	10	38	44.35	39.37	-120.46	9.04	3.8
8	27	2013	239	0	51	43.67	39.68	-119.68	13.77	3.6 (ML IDC)
6	5	2013	156	12	59	36	39.1155	-119.7155	8	2.9
9	16	2005	259	15	9	45.28	39.08	-119.64	7.2	-
10	3	2012	277	19	51	9	39.7236	-119.4361	16	3.8
6	23	2012	175	3	51	58	39.3212	-119.9844	8	3.7
4	9	2012	100	23	52	3	39.3372	-120.019	4	2.7
10	30	2011	303	13	25	19.8	39.61	-120.48	14.36	4.1
10	27	2011	300	6	37	9.34	39.61	-120.47	13.89	5
10	1	2011	274	7	7	2	38.8903	-118.774	8	4.5
8	17	2011	229	21	4	39	38.4453	-118.7206	6.6	2.57
5	28	2011	148	16	21	17	38.419	-118.7357	2	3.3
5	27	2011	147	19	45	48	38.4379	-118.6947	6	4.2
5	12	2011	132	16	23	50	38.4176	-118.7369	4	4.1
5	9	2011	129	9	46	25	38.4247	-118.7347	2	3.9
4	28	2011	118	0	49	58	38.4178	-118.7166	6	3.7
4	27	2011	117	19	19	21	38.4141	-118.718	2	4.3
4	27	2011	117	13	23	37	38.4094	-118.7257	2	3.5
12	26	2008	361	12	19	40.02	39.96	-120.87	0.03	3.1 (Mw BRK)
10	18	2009	291	15	47	29.92	39.85	-120.79	7.42	3.1 (Mw BRK)
1	17	2011	17	7	10	15	39.8776	-120.4824	6	3.5 (ML ANF)
11	21	2010	325	20	9	55.53	39.88	-120.49	9.59	4.1
4	19	2004	110	6	20	14.47	40.37	-120.63	0.04	3.7 (Mw BRK)
3	24	2011	83	21	20	40.01	40.04	-120.06	5.97	3.8
8	10	2010	222	2	12	31.2	39.88	-120.48	9.18	3.5 Mw BRK
10	18	2010	291	3	44	42.74	39.35	-120.03	6.03	3.2

COMMERCIAL EXPLOSIONS

MM	DD	YYYY	JJJ	HH	MM	SS	LAT	LON	DEPTH	M _L	M _w
7	7	2006	188	21	2	34.71	39.563	-119.6939	0	1.4	
		2006	096	20	35	07	39.461	-119.72	0	1.5	
11	14	2007	318	17	3	46.66	39.4949	-119.61	0		
1	15	2007	15	22	19	47	39.46	-119.59	0	1.7	
		2007	162	21	53	29	39.46	-119.61	0	1.7	
8	22	2008	235	20	48	47.12	39.4699	-119.6183	0		
7	30	2007	211	22	1	40.34	39.4699	-119.6183	0		
3	23	2006	82	21	29	48.876	38.9768	-119.1163	2.2	1.4	
6	21	2003	172	0	24	14.185	39.4521	-119.5432	0	1.55	
6	29	2005	180	19	11	29.167	39.5127	-119.6979	0.7652	2.9	
10	20	2006	293	21	2	45.121	39.5477	-119.7043	0	1.0	

Table 9. List of earthquakes, and commercial and nuclear explosions used in this study (continued)

8	28	2001	240	1	58	2.173	39.3714	-120.1136	0	1.5	
4	18	2002	108	17	54	15.481	39.5549	-119.194	0	1.51	
1	8	2003	8	0	31	30.074	39.4633	-119.5955	0.1961	1.4	
3	24	2003	83	23	19	23.771	39.5087	-119.6463	0	1.4	
3	31	2003	90	23	6	11.769	39.5044	-119.65	0	1.33	
6	21	2003	172	0	24	14.185	39.4521	-119.5432	0	2.5	
7	30	2007	211	22	1	39.838	39.4579	-119.6078	0		
11	14	2007	318	17	3	46.55	39.5131	-119.6603	0		
4	2	2008	93	23	4	1.186	39.5332	-119.6362	0	1.8	
7	22	2008	204	22	25	12.606	39.2291	-119.7358	0	1.2	
6	11	2009	162	19	14	49.302	39.5095	-119.6479	0	1.2	
7	13	2009	194	18	1	46.439	39.4638	-119.6143	0	2.0	
		2009	108	18	32	40	39.51	-119.64	0	1.2	
8	20	2010	232	0	5	35.958	39.5522	-119.6432	0		
9	2	2010	245	20	35	5.767	39.4751	-119.5769	0		
7	22	2011	203	22	34	36.477	39.5207	-119.6197	0	1.7	
9	6	2011	249	16	56	56.536	39.4673	-119.6122	0		
9	17	2011	260	22	7	27.087	39.513	-119.6479	0		

Table 10. Regression parameters of m_{Pg} and M_L (UNR).

The table shows parameters in the equation $M_L - \log_{10}(A_{Pg}) = a \log_{10}(\Delta) + b$, the station correction as the median of the difference $M_L - m_{Pg}$, where $m_{Pg} = \log_{10}(A_{Pg}) + a \log_{10}(\Delta) + b$ and the value of the correlation coefficient of M_L and m_{Pg} .

Station	Station location	Event distance range (km)	Event magnitude range (corrected m_{Pg})	a	b	C	Correlation coefficient
YER	38.9852N,119.2406W	50-86	1-5	0.11	1.14	0.5	0.92
WVA	39.9444N, 119.825W	44-123	1-5	-0.02	1.29	-0.03	0.93
WIL	38.81N,119.909W	49-103	1-5	0.002	1.25	0.05	0.99
MNV	38.4322N,118.1531W	155-263	1.5-5.6	0.101	0.55	0.69	0.99
WAK	38.5044N,119.4372W	60-230	1-	0.103	1.26	-0.46	0.95
ELK	40.7448N,115.2388W	390-457	3-5.9	0.043	2.3	-0.23	0.99
CMB	38.0345N,120.3865W	147-413	1-5.7	0.116	1.55	-0.63	0.97

4.3.2. Application of the M_s - m_b Discriminant to a Set of Very Shallow Earthquakes in Western Nevada

INTRODUCTION

An unusually shallow earthquake sequence (1-4 km deep) occurred in 2008 in Mogul, west of Reno, Nevada. Double-difference event relocations confirmed that all the $M_L \geq 3$ events of the Mogul sequence were shallower than five km, with a main shock at 2.8 km below the surface, which satisfied criteria for *GT1* qualification (von Seggern *et al.*, 2014, submitted to Seismological Research Letters). High-amplitude near-field ground motions and rapid attenuation with distance were observed for the Mogul main shock and principal fore- and aftershocks (Anderson *et al.*, 2009). Regional body waves and intermediate-period surface waves were observed for the Mogul sequence, and for earthquakes within 100 km of Mogul, west Reno, Nevada. This study aims to estimate the effectiveness of the M_s - m_b discriminant (Stevens and Day, 1985) in separation of this very shallow sequence from deeper earthquakes and nuclear explosions.

The M_s - m_b discriminant compares ratios of the amplitudes of long period surface waves (17 - 23 s), recorded at more than 20° epicentral distance, to short-period body waves for teleseismic events (Selby *et al.*, 2012). Because, for similar body-wave magnitude the earthquakes are more efficient in surface-wave generation than explosions, this discriminant has been proven effective for larger magnitude earthquakes ($m_b > 4$). For smaller events, short-period ($f > 0.5$ Hz) seismic discriminants were more effective (Subtask 4.2.1), however, the physical basis for these discriminants was less well understood, and they were highly dependent on the station-event configuration, due to regional variations of amplitude attenuation. To extend the discriminant M_s - m_b to regional data, Bonner *et al.*, (2006) built the M_s (VMAX) measurement technique, used in this study, to estimate a variable-period T ($8 \text{ s} < T < 25 \text{ s}$) Rayleigh-wave magnitude. As mentioned by Bonner *et al.* (2006), the results of this technique compared favorably (within 0.1 unit) to the historical formula of Rezapour and Pearce (1998).

When a new earthquake sequence is available, one challenge for the M_s - m_b discriminant is finding enough information to estimate a set of magnitudes which make possible the use of an existing discrimination line. Several M_s - m_b screening lines have been developed using magnitudes estimated by the International Seismological Centre (ISC), the International Data Center (IDC) and the National Earthquake Information Center (NEIC) (Stevens and McLaughlin, 1997; Selby *et al.*, 2012). In this study, the M_s of the Mogul earthquakes and of events within 100 km is compared to m_b for two types of screening lines: 1) the revised provisional m_b - M_s IDC screening line (Selby *et al.*, 2012) and 2) the screening line estimated by Bonner *et al.*, (2006) using M_s (VMAX) and $m_b(P_n)$ in a study of earthquakes and nuclear explosions that occurred on or near the Nevada Test Site (NTS).

DATA

Four larger Mogul earthquakes and seven earthquakes which occurred within 100 km of Mogul ($m_b > 3.0$) were analyzed (Table 11) at stations as far as 1400 km. The vertical component of broadband waveforms was provided by the Incorporated Research Institutions for Seismology (IRIS). Every signal was also visually examined by an analyst. Examples of waveforms from three stations for the Mogul earthquake and two crustal earthquakes are shown in Figure 50. The waveforms were corrected for the instrument response and converted to displacement in nanometers (*nm*). The waveforms from IRIS were corrected to displacement using the frequency-amplitude-response file.

METHOD

First, in order to investigate whether the Mogul sequence satisfies the earthquake criteria established by the International Data Center (IDC) a new formula published by Selby *et al.* (2012) was used. This formula is for a revised m_b - M_s screening line, based on ISC/IDC-estimated magnitudes:

$$M_s - m_b = 0.64 \quad (18)$$

According to Selby *et al.*, (2012), this formula “was agreed upon by the Waveform Expert Group at Working Group B of the CTBT Preparatory Commission in February 2010 and has been tested in operations at the IDC since 3 June 2010.” To obtain this formula, the M_s magnitude was calculated using the procedure of Marshall and Basham (1972). Like Selby *et al.* (2012), the m_b ($m_b \geq 3.5$) magnitudes used in this study were IDC-estimated maximum-likelihood magnitudes (Lilwall, 1986; Zaslavsky-Paltiel & Steinberg 2008) and where no other m_b was available, the ISC network-average m_b was used. M_s and maximum-likelihood m_b values (provided by the IDC) were extracted from the International Seismological Centre (ISC) catalogue (Tables 11 and 12).

Second, $M_s(VMAX)$ and m_b were estimated at local and regional distances and compared to previous studies. For earthquakes and nuclear explosions in Nevada, Bonner *et al.*, (2006) developed the classification equation:

$$d = M_s(VMAX) - 1.2 m_b(P_n) \quad (19)$$

where the decision value d should be $d > -2.6$ for the event to be in the earthquake population.

The $m_b(P_n)$ used by Bonner *et al.*, (2006) to derive this classification line was developed by Denny *et al.* (1987), specifically for the western US, and was calibrated to the NEIC magnitude using an extensive database of earthquakes and nuclear explosions at or near the NTS. The amplitude measurements were made on simulated short-period Worldwide Standard Seismographic Network response seismograms. Denny *et al.* (1987) defined the m_b scale for P_n arrivals as:

$$m_b(P_n) = \log(A) + 2.4 \log(\Delta) + 3.95 + C, \quad (20)$$

where A is the peak-to-peak amplitude in nanometers, Δ is the distance in kilometers, and C is a station constant empirically determined to be -0.02 for MNV and -0.13 for ELK (Denny *et al.*, 1989). Subsequently, Tibuleac *et al.* (2002) showed the constant at NV31 (-0.018) was approximately equal to

the MNV constant. Thus, the digital seismograms used to measure $m_b(Pn)$ were filtered to simulate a WWSS SP seismogram by deconvolving the broadband instrument response and convolving with the WWSS SP response.

In this study, where NEIC m_b estimates were available, they were preferred. Otherwise, the maximum amplitude of the P_n phase was picked (zero-to-peak) within 5 sec of the phase onset. In this case, the waveforms were filtered from 0.6 to 5 Hz, with an eight-pole, zero-phase Butterworth filter. $m_b(Pn)$ was estimated as the mean of values measured only at available calibrated stations. The procedure is further discussed in the Results section.

$M_s(VMAX)$ was measured using a time-domain method for measuring surface waves using zero-phase Butterworth filters developed by Russell (2006). This method measured surface-wave magnitudes at regional and teleseismic distances, with periods from 8s to 25s, and was developed into the $M_s(VMAX)$ technique by Bonner *et al.* (2006). $M_s(VMAX)$ was estimated in this study using Equation 1 in Bonner *et al.* (2008). "At the reference period $T=20$ seconds, the equation is equivalent to von Seggern's (1977) formula scaled to Vaněk *et al.* (1962) at 50 degrees. For periods $8 \leq T \leq 25$, the equation is corrected to $T=20$ seconds, accounting for source effects, attenuation, and dispersion" (Bonner *et al.*, 2006). We chose to use the advantage of the $M_s(VMAX)$ technique to allow measurements of surface wave magnitudes at local and regional distances where traditional 20s magnitudes cannot be used. Another advantage was that, through the application of narrowband Butterworth-filtering this technique according to Bonner *et al.* (2006): "handles Airy phase phenomena that, prior to this technique, had to be accounted for using Marshall and Basham's (1972) empirical path corrections."

Following Bonner *et al.* (2006), a set of programs by Herrmann and Ammon, (2002) was used to perform Multiple Filter Analysis (Dziewonski *et al.*, 1969), in order to extract dispersion curves. At each station, the dispersion curves have been used to apply Phase Match Filtering (PMF) (Herrin and Goforth, 1977). The $M_s(VMAX)$ algorithms (kindly provided to the authors by Jessie Bonner, 2013) were applied on the phase-match filtered waveforms. $M_s(VMAX)$ was estimated for each event from variable period measurements at multiple stations. Because the all the earthquakes were located within 100 km, the Rayleigh waves were identified by an analyst between the time lags corresponding to group velocities of 4 km/s and 2 km/s. Based on previous experience estimating dispersion curves in Nevada, an analyst chose the dispersion curve used in the PMF filter.

Figure 51 shows examples of filter panels with records of the Mogul main shock, a 2008 Mogul aftershock and two earthquakes occurred on 2005/09/16, 15:09:42 and on 2011/10/27, 06:33:02, recorded at station WVOR. The advantage of using $M_s(VMAX)$ is that the formula accounts for differences "in the excitation, attenuation, and propagation of variable-period surface waves." (Bonner *et al.*, 2006)

RESULTS

1. *M_s - m_b discrimination using ISC magnitude values.* Similar to Selby *et al.* (2012) m_b and M_s were chosen from the ISC bulletin for each of the earthquakes in Table 1. Table 12 summarizes the magnitudes used in Figure 52. All the earthquakes would have been classified as earthquakes, as they are above the screening line.

2. M_s - m_b discrimination using $M_s(VMAX)$. The results of the $M_s(VMAX)$ analysis of the events are summarized in Table 12 and shown in Figure 53. An illustration of the $M_s(VMAX)$ method application to the three earthquakes in Figure 50 is shown in Figure 53. Again, all the earthquakes were above the screening line. The $M_s(VMAX)$ standard deviation was similar for all the earthquakes, not exceeding 0.1 m.u, except for the smallest Mogul earthquake which occurred on 2008:115:22:47 ($m_b = 3$) and which had a standard deviation of 0.22 m.u.

A possible explanation for these results is that very shallow earthquakes may cause stronger surface waves than deeper-focus earthquakes (Tsai, 1969), thus, they may be more easily classified in comparison with explosions than deeper earthquakes.

Different magnitude formulas were used to estimate m_b and M_s by the IDC, ISC and NEIC. Correspondences between these formulas were the object of multiple studies. IDC m_b and M_s were, on average, 0.4 and 0.1 units, respectively, less than those reported by the NEIC. The IDC used the M_s formula of Rezapour and Pearce (1998), and the surface-wave measurement procedure outlined in Stevens and McLaughlin (2001). A comparison with the network average $M_s(VMAX)$ values for explosions at the NTS as reported by Bonner *et al.* (2006), shows $M_s(VMAX)$ about 0.22 m.u. greater than M_s estimated using the Marshal and Basham (1972) formula.

CONCLUSIONS

Based on differences between M_s and m_b , four very shallow Mogul earthquakes (depth < 3 km) and seven crustal earthquakes within 100 km, with m_b (NEIC) > 3 m.u. and $M_s(VMAX)$ > 3.1 m.u. were screened as earthquakes, when using screening lines for teleseismic and regional events. Because magnitude estimations from international agencies were not available for all earthquakes, magnitude measures developed for regional events in Nevada were chosen: $m_b(Pn)$ and $M_s(VMAX)$. Except for one event that occurred east of Carson City on September 16, 2005, which has few measurements and is relatively close to the line, all the earthquakes classified well above the discrimination line estimated by Bonner *et al.*, 2006.

ACKNOWLEDGEMENTS

We thank Dr Jessie Bonner, who kindly provided the $M_s(VMAX)$ magnitude estimation codes. We thank Dr David von Seggern for comments and suggestions. Magnitude estimates were provided by NEIC and ISC. The waveforms used in this study were provided by the Incorporated Research Institutions for Seismology (IRIS) and by the Nevada Seismological Laboratory. The IRIS Data Management Center was used for access to waveforms. IRIS Data Services are funded through the Seismological Facilities for the Advancement of Geoscience and EarthScope (SAGE) Proposal of the National Science Foundation under Cooperative Agreement EAR-1261681.

Table 11. Earthquakes used in this study. Highlighted rows are Mogul earthquakes.

<i>Date</i>	<i>Time</i>	<i>Lat (deg)</i>	<i>Lon (deg)</i>	<i>ISC Depth (km)</i>	<i>M_L</i>	<i>m_b</i>	<i>M_w</i>	<i>M_s</i>
2008/04/24	22:47:05	39.50	-119.83	10	3.6 (IDC) 4.1 (REN)	2.7 (IDC) 3.4 (mb1) 3.2 (mb1mx)	3.7 (BRK)	2.9 (IDC) 2.9 (Ms1) 2.9 (ms1mx)
2008/04/24	22:55:49	39.65	-119.87	10	4.0 (IDC) 4.2 (REN)	3.3 (IDC) 4.0 (mb1) 3.6 (mb1mx)	4.3 (BRK)	3.5 (IDC) 3.5 (Ms1) 3.4 (ms1mx)
2008/04/28	11:33:20	39.55	-119.78	10	4.2 (REN) 3.5 (IDC)	2.9 (IDC) 3.6 (mb1) 3.5 (mb1mx)	4.1 (BRK)	3.2 (IDC) 3.2 (Ms1) 3.0 (m1mx)
2008/04/26	06:40:11	39.45	-119.88	10	4.7 (REN) 4.0 (IDC)	4.3 (IDC) 4.5 (mb1) 4.4 (mb1mx)	5 (BRK) 4.9 (SLM)	4.4 (IDC) 4.3 (Ms1) 4.3 (ms1mx)
2012/06/23	03:51:57	39.31	-119.98	6.8	4.2 (REN)	4.2 (NEIC) 3.6 (ISC,mb1m) 3.9 (mb1) 3.7(mb1mx)	4 (NEIC)	3.2 (ISC) 3.1 (Ms1) 2.9 (ms1mx)
2005/06/26	18:45:56	39.34	-120.05	11.1	3.9 (IDC)	4.6 (NEIC) 4.2 (IDC,mb1) 4.2 (mb1mx) 4.6 (NEIC)	4.8 (BRK)	4.0 (IDC) 3.9 (msl1mx)
2005/09/16	15:09:42	39.10	-119.6	10.0	4.0 (IDC) 4.2 (REN)	3.9 (IDC) 4.1 (mb1) 3.9(mb1mx)	4.2 (BRK)	3.4 (IDC) Ms1 (3.3) ms1mx (3.1)
2000/12/02	15:34:15	39.37	-120.45	14.3	4.9 (REN)	3.9 (ISC) 4.3 (NEIC) 4.0 (IDC)	4.4 (BRK)	3.8 (IDC) 3.7 (ISC)
2001/08/10	20:19:27	39.90	-120.58	10	5.3 (REN) 4.6 (IDC)	4.6 (mb1mx) 4.6 (ISC, mb1) 4.4 (mb, ISC) 4.8 (NEIC)	5.1 (BRK) 5.2 (HRVD)	4.7 (ISC) 4.9 (NEIC) 4.5 (IDC, Ms1) 4.4 (msl1mx)
2011/10/27	06:37:05	39.61	-120.47	16	4.1 (IDC)	4.7 (NEIC) 4.3 (IDC)	4.9 (GCMT) 4.7 (BRK)	3.9 (IDC) 3.9 (Ms1) 3.8 (ms1mx)

Table 11. Earthquakes used in this study. Highlighted rows are Mogul earthquakes. (continued)

						4.4 (mb1) 4.3 (mb1mx)		
2013/08/27	00:51:43	39.66	-119.68	13.9	3.6 (IDC)	3.8 (IDC) 3.9 (mb1) 3.8 (mb1mx)	NA	3.2 (IDC) 3.1 (Ms1) 3.0 (ms1mx)

ISC/IDC magnitude scale nomenclature: mb – short periods body wave magnitude (stations between 20 and 160 degree distances); mb1 – IDC short period body wave magnitude (includes stations below 20 degree distances); mb1mx –IDC maximum likelihood short period body wave magnitude ; ms1mx –IDC maximum likelihood surface wave magnitude; REN stands for the Nevada Seismological Laboratory (NSL) estimate, using the ISC notations; BRK for the University of California at Berkeley estimate and HRVD for Harvard University.

Table 12. The magnitude values used in Figures 52 and 53.

Origin Time	m_b (NEIC)	m_{b1mx}	m_b (ISC)	M_s (ISC)	m_{s1mx} (IDC)	M_s (VMAX)	σ
2000/12/02 153415	4.3	3.9*	3.9	3.7	-	3.8	0.1
2001/08/10 201927	4.8	4.6	4.6	4.7	4.4	4.6	0.1
2005/06/26 184556	4.6	4.2	4.3	4.0	3.9	4.0	0.1
2005/09/16 150942	4.8**	3.9	4.2	3.5	3.1	3.4	0.1
2011/10/27 063302	4.7	3.8	4.6	4.0	3.8	4.0	0.1
2012/06/23 035157	4.2	3.6	-	-	2.9	3.2	0.1
2013/08/27 005143	3.7***	3.8	-	-	3.0	3.2	0.1
2008/04/24 224705	3 ****	3.2	-	-	2.5	3.1	0.2
2008/04/24 225549	3.7	3.6	-	3.4	3.4	3.6	0.1
2008/04/26 064011	4.8	4.4	4.6	4.5	4.3	4.4	0.1
2008/04/28 064011	3.8**	3.5	-	-99	3.0	3.2	0.1

* Magnitude unavailable, replaced with the value of m_b (ISC);

** Magnitude unavailable, replaced with a value estimated with Equation 20 at station ELK;

*** Magnitude unavailable, replaced with the mean $m_b(P_n)$ estimated using Equation 20 at stations ELK and NV31;

**** Magnitude unavailable, replaced with $3.7 - 0.7 = 3$. The value 0.7 is the ten base logarithm of the ratio between the amplitude of the 2008/04/24 22:55 and 2008/04/24 22:47 at station L10A, chosen randomly. The amplitude of the same time lag arrival within the first 5 seconds was measured.

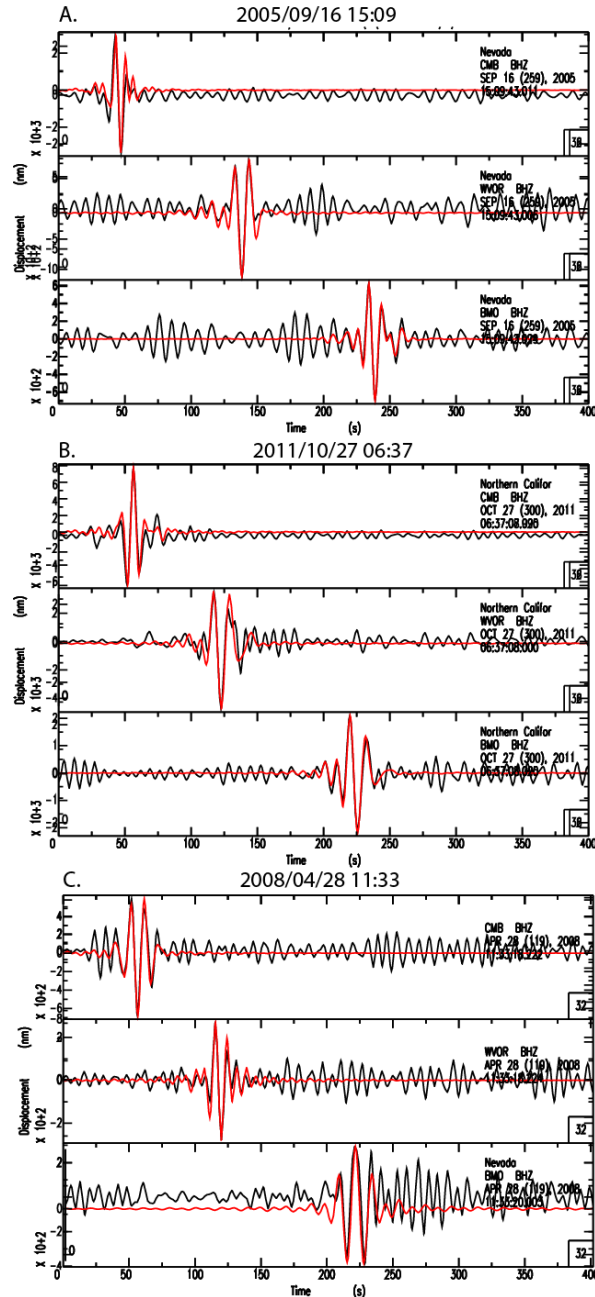


Figure 50. A: Displacement (nm) waveforms of the 2005/09/16, 15:09:42 earthquake, ML 4.2 (black) filtered between 7 s and 25 s, with a Butterworth, 6 pole, zero phase filter recorded at three stations: CMB (epicentral distance 130 km, azimuth 213 deg), WVOR (epicentral distance 386 km, azimuth 11.58 deg) and BMO (epicentral distance 674 km, azimuth 15 deg). Superposed are the (red) waveforms obtained after applying PMF on the raw data, which have been used for $M_s(VMAX)$ estimation. **B.** Same as Inset A for an earthquake that occurred on 2011/11/27 06:33:02, of magnitude ML 4.1 (IDC); **C.** Same as Inset A for an earthquake on 2008/10/27, 11:33:20, ML 4.2.

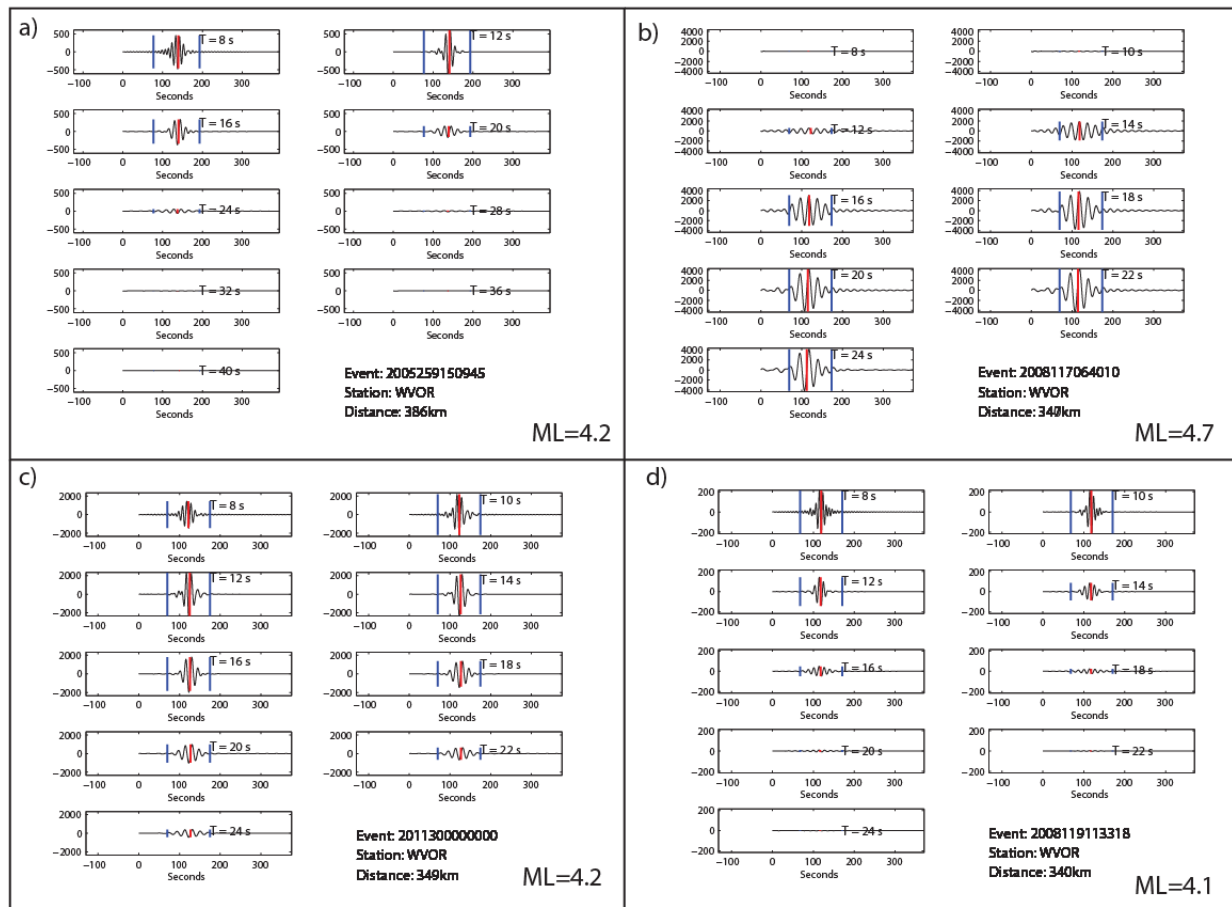


Figure 51. Examples of Butterworth-filtered seismograms for four earthquakes recorded at WVOR (Table 1). The y axis shows displacement in nm. The x axis is time in seconds from the event origin. Each filter panel has two vertical lines that represent the time lags corresponding to group velocity 2.0 and 4.0 km/sec. The location of the maximum amplitude at each center period is also marked by a thin vertical line.

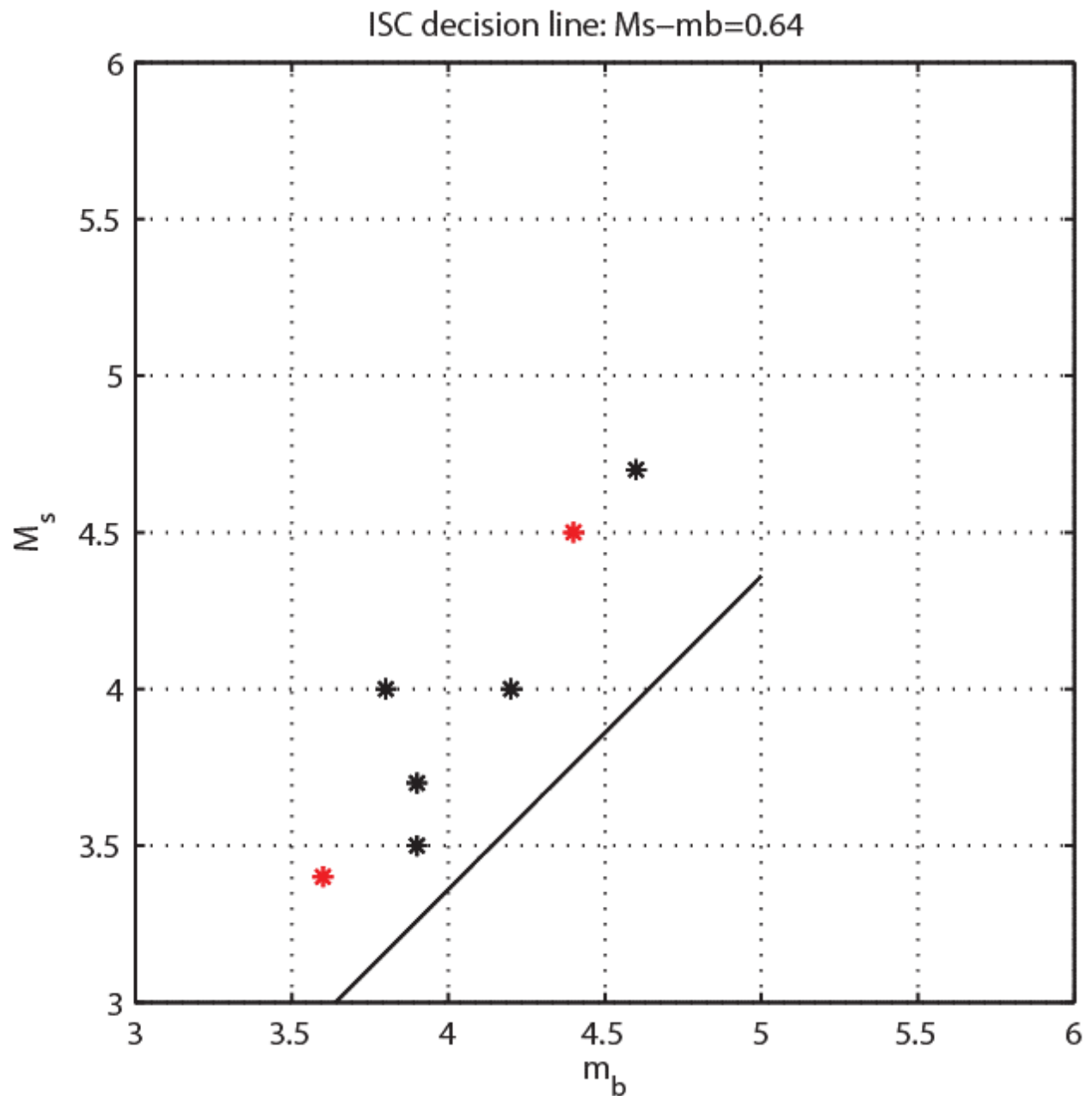


Figure 52. Discrimination results for maximum-likelihood m_b (IDC) and ISC-estimated M_s using the decision line estimated by Selby et al., (2012). Red dots are the Mogul earthquakes and black dots are deeper, crustal earthquakes occurred within 100 km of the Mogul sequence. Note that all the earthquakes are correctly classified, however, not all the Mogul earthquakes are on this plot, because magnitude estimates were not available (see also Table 11).

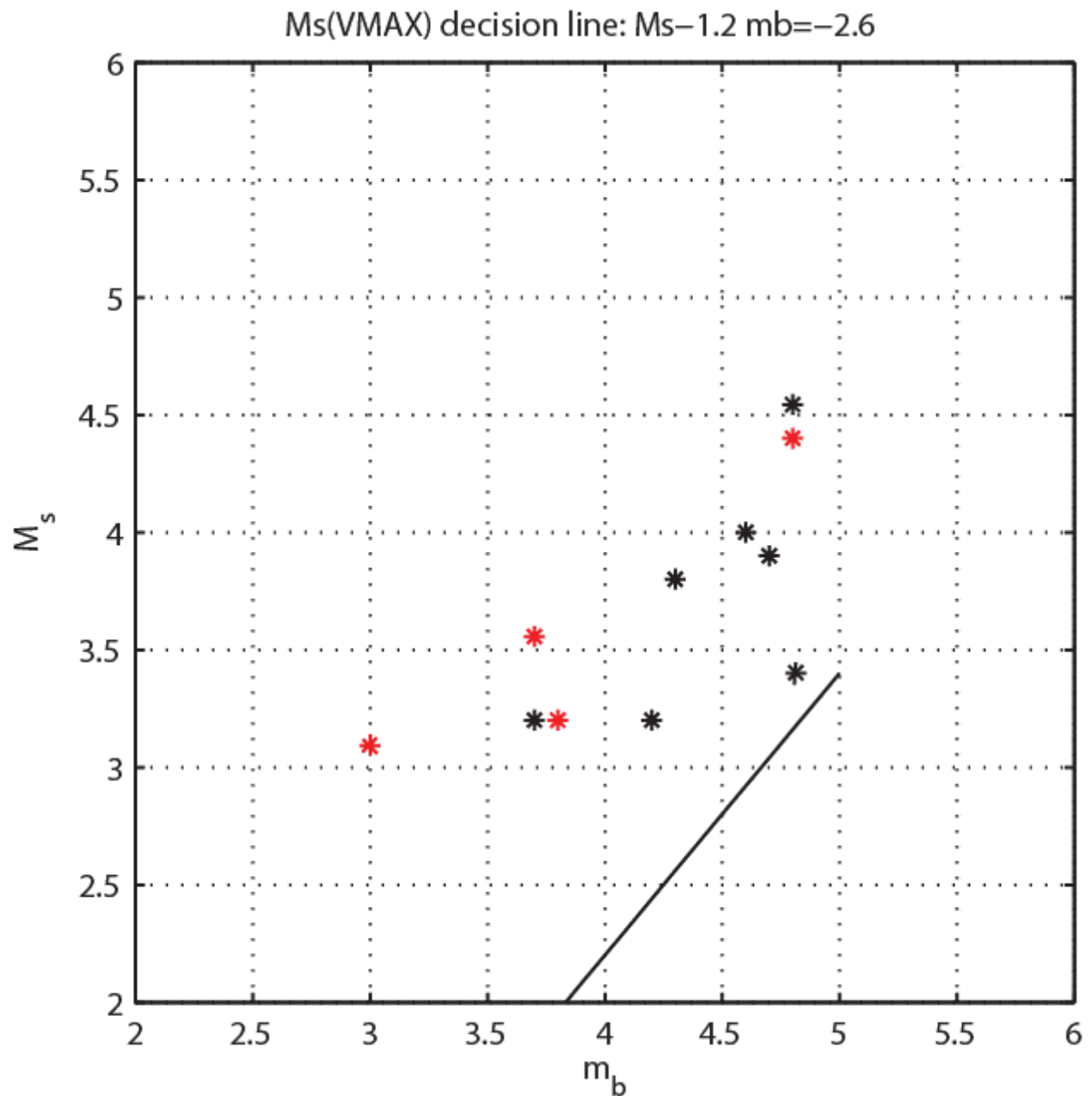


Figure 53. Discrimination results for m_b and M_s (VMAX) using the decision line estimated by Bonner et al., (2006). Red dots are the Mogul earthquakes and black dots are deeper, crustal earthquakes that occurred within 100 km of the Mogul sequence. All the earthquakes are correctly classified. One 10 km deep earthquake (ISC) that occurred on 2005/09/16 (Table 12) was closest to the decision line.

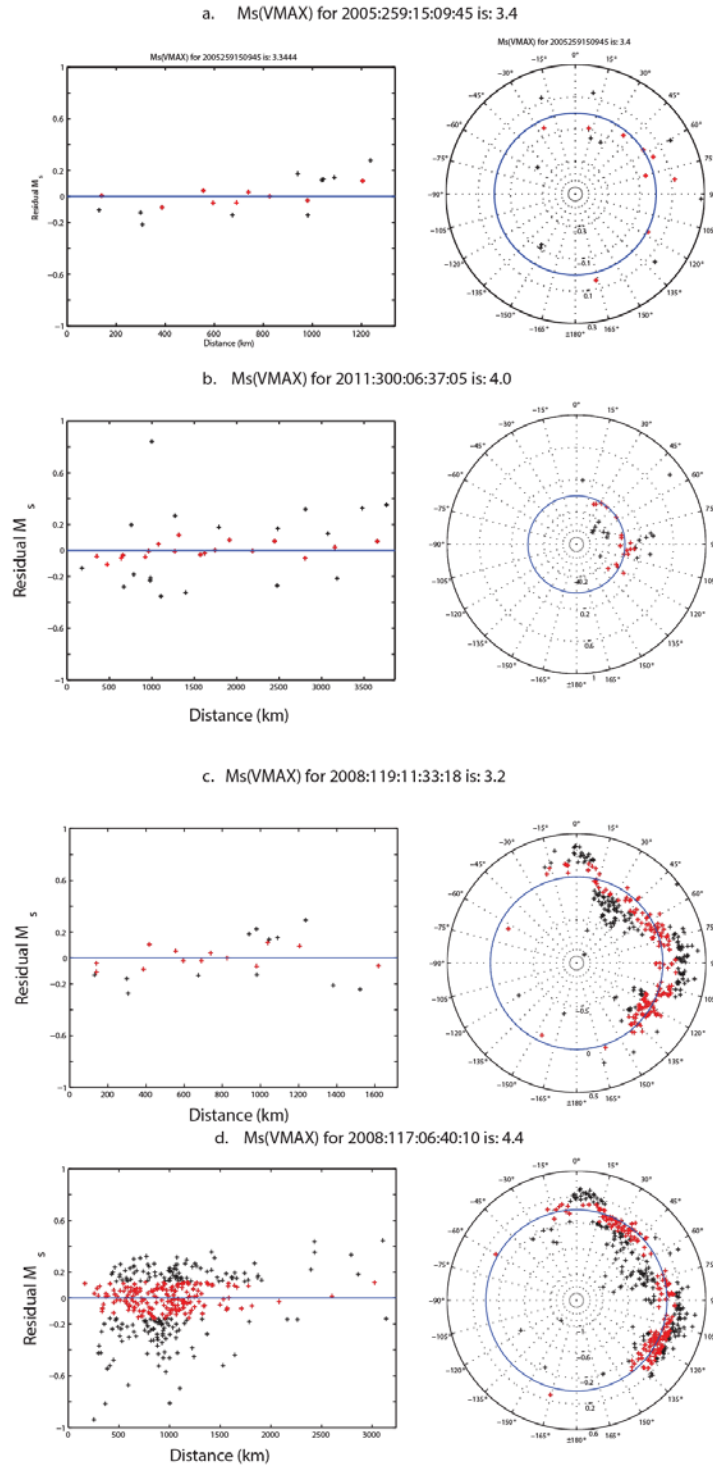


Figure 54. Examples of $M_s(\text{VMAX})$ estimation for the earthquakes in Figure 50 and for the Mogul Main shock. The $M_s(\text{VMAX})$ residuals are shown as either black or red dots. The red dots are residuals of the magnitude values used for $M_s(\text{VMAX})$ estimation. These magnitude values were chosen to be larger than the 25 percentile and lower than the 75 percentile of all estimates for each event. The left plots show the $M_s(\text{VMAX})$ residuals from the mean as a function of distance. The right plots show the same residuals as a function of azimuth. The azimuthal residual patterns in plots c and d are possibly due to source effects.

REFERENCES

- Abercrombie, R. and J. Mori (1994), Local Observations Of The Onset Of A Large Earthquake - 28 June 1992 Landers, California, *Bulletin of the Seismological Society of America*, 84(3), pp. 725-734.
- Abercrombie, R.E. (2012), Comparison of direct and coda wave stress drop measurements for the Wells, Nevada, earthquake sequence, *J. Geophys. Res.*, Vol. 118, pp. 1-13, doi:10.1029/2012JB009638.
- Aki and Richards (2002). *Quantitative Seismology, Theory and Methods*, University Science Books.
- Allman and Shearer (2009), Global variations of stress drop for moderate to large earthquakes, *J. Geophys. Res.*, 114, B01310, doi:10.1029/2008JB005821.
- Anderson, J. G. (1986), Implication of attenuation for studies of the earthquake source in *Earthquake Source Mechanics*, Maurice Ewing Series 6, S. Das, J. Boatwright, and C. H. Scholz (Editors), American Geophysical Union, Washington, D.C., pp. 311-318.
- Anderson, J. G. (1991), A preliminary descriptive model for the distance dependence of the spectral decay parameter in southern California, *Bulletin of the Seismological Society of America*, December 1991, Vol. 81, no. 6, pp. 2186-2193.
- Anderson, J. G. and S. E. Hough (1984), A model for the shape of the Fourier amplitude spectrum of acceleration at high frequencies, *Bull. Seism. Soc. Am.*, 74, pp. 1969-1993.
- Anderson J. G. and J. R. Humphreys (1991), A least-squares method for objective determination of earthquake source parameters, *Seism. Res. Lett.*, 62, pp. 201-209.
- Anderson, J. G., I. Tibuleac, A. Anoshehpour, G. Biasi, K. Smith, and D. von Seggern (2009), Exceptional ground motions recorded during the 26 April 2008 MW 5.0 earthquake in Mogul, Nevada, *BSSA* 99, 3475-3486.
- Baltay, A., G. Prieto, and G. C. Beroza (2010), Radiated seismic energy from coda measurements and no scaling in apparent stress with seismic moment, *J. Geophys. Res.*, 115, B08314, doi:10.1029/2009JB006736.
- Baumgardt, D. R. and G. B. Young (1990), Regional seismic waveform discriminants and case-based event identification using regional arrays, *Bull. Seism. Soc. Am.*, Vol. 80, pp. 1874-1892.
- Baumgardt, D. R. and Z. A. Der (1994), Investigation of the transportability of the P/S ratio discriminant to different tectonic regions, *Scientific Report No. 1*, PL-TR-94-2299, ENSCO, Inc., Springfield, VA., ADA292944.
- Bell, J. W., F. Amelung, and C. D. Henry (2012), InSAR analysis of the 2008 Reno-Mogul earthquake swarm: Evidence for westward migration of Walker Lane style dextral faulting, *Geophys. Res. Lett.*, 39, doi:10.1029/2012GL052795.
- Bennett, T. J. and J. R. Murphy (1986), Analysis of seismic discrimination capabilities using regional data from western United States events, *Bull. Seism. Soc. Am.*, 76, pp. 1069-1086.
- Biasi, G. P. and J. G. Anderson (2007), Measurement of the parameter kappa, and reevaluation of kappa for small to moderate earthquakes at seismic stations in the vicinity of Yucca Mountain, Nevada, *Final Technical Report TR-07-007*, Nevada System of Higher Education, University of Nevada, Las Vegas, doi 10.2172/920643.
- Biasi, G. P., D. von Seggern, J. Anderson, and I. M. Tibuleac (2012), Investigation of an unusually shallow earthquake sequence in Mogul, NV from a discrimination perspective, in *Proceedings 34th Monitoring Research Review, Ground-Based Nuclear explosion Monitoring Technologies*, pp. 345-354.
- Blewitt, G., J. Bell, W. C. Hammond, C. Kreemer, H. Plag, and C. Depolo (2008), GPS and InSAR Monitoring of the Mogul Swarm: Evidence for Mainly Aseismic Fault Creep, with Implications for Seismic Hazard, *AGU Fall Meeting Abstracts*, American Geophysical Union.
- Bondár, I., X. Yang, R. G. North, and C. Romney (2001), Location Calibration Data for CTBT Monitoring at the Prototype International Data Center, *Monitoring the Comprehensive Nuclear-Test-Ban Treaty: Source Location*, Pageoph Topical Volumes, pp. 19-34.

- Bondar, I., S. C. Myers, E. R. Engdahl, and E.A. Bergman (2004), Epicenter accuracy based on seismic network criteria, *Geophys. J. Int.*, 156, pp. 483-496.
- Bondar, I. and K. L. McLaughlin (2009), A new ground truth data set for seismic studies, *Seism. Res. Letts.*, 80, pp. 465-472.
- Bonner, J. L., D. Russell, D. Harkrider, D. Reiter, and R. Herrmann (2006), Development of a Time-Domain, Variable-Period Surface Wave Magnitude Measurement Procedure for Application at Regional and Teleseismic Distances, Part II: Application and Ms-mb Performance, *Bull. Seism. Soc. Am.*, 96, pp. 678-696.
- Bonner, J., R. B. Herrmann, D. Harkrider, and M. Pasyanos (2008), The surface wave magnitude for the 9 October 2006 North Norean nuclear explosion, *Bull. Seism. Soc. Am.*, 98, pp. 2498-2506.
- Brune, J. N. (1970), Tectonic stress and the spectra of seismic shear waves from earthquakes, *J. Geophys. Res.*, 75, pp. 4997-5009.
- Chael, E.P. (1988), Spectral discrimination of NTS explosions and earthquakes in the southwestern United States using high-frequency regional data, *Geophys. Res. Lett.*, 15, pp. 625-628.
- Chan, W. W., R. Baumstark, and R. K. Cessaro (1990), Spectral discrimination between explosions and earthquakes in central Eurasia, Air Force Geophysics Laboratory, GL- TR-90-0217.
- Cramer, C. H. and D. M. Boore (1978), The Effect of Nevada Test Site Geology on Absolute Travel-Time Residuals at Mastushiro, Japan and College, Alaska., *Bulletin of the Seismological Society of America*, Vol. 68, No. 3, pp. 859-862.
- Denny, M. D., S. R. Taylor, and E. S. Vergino (1987), Investigation of mb and Ms formulas for the western United States and their impact on the Ms=mb discriminant, *Bull. Seismol. Soc. Am.*, 77, pp. 987-995.
- Denny, M. D., S. R. Taylor, and E. S. Vergino (1989), Erratum: Investigation of mb and Ms formulas for the western United States and their impact on the Ms/mb discriminant, *Bull. Seism. Soc. Am.*, 79, p. 230.
- Dysart, P. S. and J. J. Pulli (1990), Regional seismic event classification at the NORESS Array: Seismological measurements and the use of trained neural networks, *Bull. Seism. Soc. Am.*, 80, pp. 1910-1933.
- Dziewonski, A., S. Bloch, and M. Landisman (1969), A technique for the analysis of transient seismic signals, *Bull. Seism. Soc. Am.*, 59, pp. 427-444.
- Evernden, J. (1969), Precision of epicenters obtained by small numbers of world-wide stations, *Bull. Seism. Soc. Am.*, 59, pp. 1365-1398.
- Evernden J. F. (1967), Seismic intensities, "size" of earthquakes and related parameters, *Bulletin of the Seismological Society of America*, Vol. 57, No. 4, pp. 591-639.
- Evernden, J. R., C. B. Arehambeau, and E. Cranswick (1986), An evaluation of seismic decoupling and underground nuclear test monitoring using high frequency seismic data, *Rev. Geophys.*, 24, pp. 143-215.
- Fan, G. W. and T. Lay (1998a), Statistical analysis of irregular waveguide influences on regional seismic discriminants in China, *Bull. Seism. Soc. Am.*, 88, pp. 74-88.
- Fan, G. W. and T. Lay (1998b), Regionalized versus single-station wave-guide effects on seismic discriminants in western China, *Bull. Seism. Soc. Am.*, 88, pp. 1260-1274.
- Fan, G. W. and T. Lay (1998c), Statistical analysis of irregular waveguide influences on regional seismic discriminants in China: additional results for Pn / Sn , Pn / Lg and Pg / Sn, *Bull. Seism. Soc. Am.*, 88, pp. 1504-1510.
- Fletcher, J., L. Haar, T. Hanks, L. Baker, F. L. Vernon III, J. Berger, and J. N. Brune, (1987), The digital array at Anza, *J. Geophys. Res.*, 92, pp. 369-382.
- Frankel, A., J. Fletcher, F. Vernon, L. Harr, J. Berger, T. Hanks, and J. N. Brune (1986), Rupture characteristics and tomographic source imaging of $M_L \approx 3$ earthquakes near Anza, southern California, *Journal of Geophysical Research*, v. 91, pp. 12633-12650.
- Fukuyama, E. and K. Irikura (1986), Rupture process of the 1983 Japan Sea (Akita-Oki) earthquake using a waveform inversion technique, *Bull. Seism. Soc. Am.*, 76, pp. 1623-1640.

- Gabriel, A. -A., J. -P. Ampuero, L. A. Dalguer, and P. M. Mai (2012), The transition of dynamic rupture styles in elastic media under velocity-weakening friction, *J. Geophys. Res.*, 117, B09311, doi:10.1029/2012JB009468.
- Goldstein, P. (1995), Slopes of P to S wave spectral ratios: a broadband regional seismic discriminant and a physical model, LLNL UCRL-JC-121223.
- Gupta, I. N., W. W. Chan, and R. A. Wagner (1992), A comparison of regional phases from underground nuclear explosions at east Kazakh and Nevada test sites, *Bull. Seismol. Soc. Am.*, 82, pp. 352–382.
- Hanks, T. C. and H. Kanamori (1979), A moment magnitude scale, *J. Geophys. Res.*, 84, pp. 2348-2350.
- Hartse, H., S. R. Taylor, W. S. Phillips, and G. E. Randall (1997), A preliminary study of regional seismic discrimination in Central Asia with an emphasis on Western China, *Bull. Seism. Soc. Am.*, 87, pp. 551-568.
- Hartse, H. E., R. A. Flores, and P. A. Johnson (1998), Correcting regional seismic discriminants for path effects in Western China, *Bull. Seism. Soc. Amer.*, 88, pp. 596-608.
- Hartzell, S. H. (1978), Earthquake aftershocks as Green's functions, *Geophys. Res. Lett.*, 5, pp. 1-4.
- Hartzell, S. H., C. Mendoza, and Y. Zeng (2013), Rupture model of the 2011 Mineral, Virginia, earthquake from teleseismic and regional waveforms, *Geophysical Research Letters*, Vol. 40, pp. 5665-5670, doi:10.1002/2013GL057880.
- Herrin, E. and T. Goforth (1977), Phase-matched filters: Application to the study of Rayleigh waves, *Bull. Seism. Soc. Am.*, 67, pp. 1259-1275.
- Herrmann, R. and C. J. Ammon (2002), Surface wave, receiver functions and crustal structure, *Computer Programs in Seismology*, Version 3.15, St. Louis University, St. Louis, Missouri.
- Hutchings, L. (1994), Kinematic earthquake models and synthesized ground motion using empirical Green's functions, *Bull. Seism. Soc. Am.*, 84, pp. 1028-1050.
- Kanamori, H. and Don L. Anderson (1975), Theoretical basis of some empirical relations in seismology, *Bull. Seism. Soc. Am.*, 65, No. 5, pp. 1073-1095.
- Kanamori, H. (1979), A semi-empirical approach to prediction of long-period ground motions from great earthquakes, *Bull. Seism. Soc. Am.*, 69, pp. 1645-1670.
- Kim, W. Y., V. Aharonian, A. L. Lerner-Lam, and P. G. Richards (1997), Discrimination of earthquakes and explosions in southern Russia using regional high-frequency three-component data from the IRIS/JSP Caucasus Network, *Bull. Seism. Soc. Am.*, 87, pp. 569-588.
- Lagarias, J. C., J. A. Reeds, M. H. Wright, and P. E. Wright (1998), Convergence Properties of the Nelder-Mead Simplex Method in Low Dimensions, *SIAM Journal of Optimization*, Vol. 9, Number 1, pp. 112-147.
- Lee, S. -J., B. -S. Huang, M. Ando, H. -C. Chiu, and J. -H. Wang (2011), Evidence of large scale repeating slip during the 2011 Tohoku-Oki earthquake, *Geophys. Res. Lett.*, 38(19), L19306, doi:10.1029/2011GL049580.
- Lilwall, R. C. (1986), Some Simulation Studies on Seismic Magnitude Estimators, AWRE Report 0 22/86, Her Majesty's Stationery Office, London.
- Lowrie, W., (2007), *Fundamentals of Geophysics*, Cambridge University Press, Cambridge, MA.
- Ludwig, W. J., J. E. Nafe, and C. L. Drake (1970), Seismic refraction, in the sea, A. E. Maxwell (editor), vol. 4, Willey-Interscience, New York.
- Malagnini, L., P. Bodin, K. Mayeda, and A. Akinci (2006), Unbiased moment-rate spectra and absolute site effects in the Kachachh Basin, India, from the analysis of the aftershocks of the 2001 Mw 7.6 Bhuj earthquake, *Bull. Seismol. Soc. Am.*, 96, pp. 456-466, doi: 10.1785/0120050089.
- Marshall, P. D. and P. W. Basham (1972), Discrimination between earthquakes and underground explosions employing an improved Ms scale, *Geophys. J. R. Astr. Soc.*, 29, pp. 431-458.
- Mayeda, K. and W. R. Walter (1996), Moment, energy, stress drop, and source spectra of western U.S. earthquakes, *J. Geophys. Res.*, 101, pp. 11195-11208.
- Mayeda, K., A. Hofstetter, J. L. O'Boyle, and W. R. Walter (2003), Stable and transportable regional magnitudes based on coda-derived moment-rate spectra, *Bull. Seismol. Soc. Am.*, 93, pp. 224-239.

- Mayeda, K. and L. Malagnini (2010), Source radiation invariant property of local and near-regional shear-wave coda: Application to source scaling for the Mw 5.9 Wells, Nevada sequence, *Geophys. Res. Lett.*, 37, L07306, doi:10.1029/2009GL042148.
- Menke, W. and D. P. Schaff (2004), Absolute earthquake location with differential data, *Bull. Seismol. Soc. Am.*, 94, pp. 2254-2264.
- Morasca, P., K. Mayeda, L. Malagnini, and W. R. Walter (2005), Coda derived source spectra, moment magnitudes, and energy-moment scaling in the Western Alps, *Geophys. J. Int.*, 160, pp. 263-275.
- Mori, J., and A. Frankel (1990), Source parameters for small events associated with the 1986 north Palm Springs, California, earthquake determined using empirical Green's functions, *Bull. Seismol. Soc. Am.*, 80, pp. 278-295.
- Pancha, A., J. G. Anderson, and J. N. Louie (2007), Characterization of near-surface geology at strong-motion stations in the vicinity of Reno, Nevada, *Bulletin of the Seismological Society of America*, 97, pp. 2096-2117.
- Pasyanos, M. E. and W.R. Walter (2009), Improvements to regional explosion identification using attenuation models of the lithosphere, *Geophys. Res. Lett.*, L14304, doi:10.1029/2009GL038505.
- Phillips, W. S., G. E. Randall, and S. R. Taylor (1998), Regional Phase Path Effects in Central China, *Geophys. Res. Lett.*, 25, pp. 2729-2732.
- Phillips, W. S. (1999), Empirical Path Corrections for Regional-phase Amplitudes, *Bull. Seismol. Soc. Am.*, 89, pp. 384-393.
- Phillips, W. S. and R. J. Stead (2008), Attenuation of Lg in the western US using the USArray, *Geophys. Res. Lett.*, 35, L07307, doi:10.1029/2007GL032926.
- Phillips, W. S., R. J. Stead, G. E. Randall, H. E. Hartse, and K. M. Mayeda, (2008), Source effects from broad area network calibration of regional distance coda waves, in *Scattering of Short Period Waves in the Heterogeneous Earth*, H. Sato and M. C. Fehler, Editors.
- Prejean, S. and William L. Ellsworth (2001), Observations of Earthquake Source Parameters at 2 km Depth in the Long Valley Caldera, Eastern California, *Bulletin of the Seismological Society of America*, 91, 2, pp. 165-177.
- Rezapour, M. and R. G. Pearce (1998), Bias in surface-wave magnitude M_s due to inadequate distance correction, *Bull. Seism. Soc. Am.*, 88, pp. 43-61.
- Rodgers A. J., W. R. Walter, C. A. Schultz, S. C. Myers, and T. Lay (1999), A Comparison of Methodologies for Representing Path Effects on Regional P/S Discriminants, *Bull. Seismol. Soc. Am.*, 89, pp. 394-408.
- Russell, D. R. (2006), Development of a Time-Domain, Variable-Period Surface Wave Magnitude Measurement Procedure for Application at Regional and Teleseismic Distances, Part I: Theory, *Bull. Seism. Soc. Am.*, 96, pp. 665-677.
- Sadeghi, H., H. Miyake, and A. Riahi (2012), Strong ground motion simulation of the 2003 Bam, Iran, earthquake using the empirical Green's function method, *J. Seismol.*, DOI 10.1007/s10950-012-012-9317-4.
- Schultz, C. A., S. C. Myers, J. Hipp, and C. J. Young (1998), Nonstationary Bayesian kriging: A predictive technique to generate spatial corrections for seismic detection, location and identification, *Bull. Seismol. Soc. Am.*, 88, pp. 1275-1288.
- Selby, N., P. Marshall, and D. Bowers (2012), mb: M_s Event Screening Revisited, *Bulletin of the Seismological Society of America*, Vol. 102, No. 1, pp. 88-97, doi:10.1785/0120100349.
- Shearer, P. M., G. A. Prieto, and E. Hauksson (2006), Comprehensive analysis of earthquake source spectra in southern California, *J. Geophys. Res.*, 111, B06303, doi:10.1029/2005JB003979.
- Smith, K., D. H. von Seggern, D. dePolo, J. G. Anderson, G. P. Biasi, and R. Anooshehpour (2008), Seismicity of the 2008 Mogul-Somerset West Reno, Nevada Earthquake Sequence, *Eos Trans. AGU*, 89(53), Fall Meet. Suppl., Abstract S53C-02.
- Stevens, J. L. and S. M. Day (1985), The physical basis for mb- M_s and variable frequency magnitude methods for earthquake/explosion discrimination, *J. Geophys. Res.*, 90, pp. 3009-3020.

- Stevens, J. L. and K. L. McLaughlin (1997), Improved methods for regionalized surface wave analysis, Maxwell Technologies Final Report, submitted to Phillips Laboratory, MFD-TR-97-15887.
- Stevens, J. L. and K. L. McLaughlin (2001), Optimization of surface wave identification and measurement, *Pure and Appl. Geophys.*, 158, pp. 1547-1582.
- Street, R. L., R. B. Herrmann, and O.W. Nuttli (1975), Spectral characteristics of the Lg wave generated by central United States earthquakes, *Geophys. J. R. Astr. Soc.*, 41, pp. 51-63.
- Sun, X. and S. Hartzell (2014), Finite fault slip model of the 2011 Mw 5.6 Prague, Oklahoma earthquake from regional waveforms, *Geophys. Res. Lett.*, 40, pp. 4207-4213, doi:10.1002/2014GL060410.
- Taylor, S. R., N. W. Sherman, and M. D. Denny (1988), Spectral discrimination between NTS explosions and western United States earthquakes at regional distances, *Bull. Seism. Soc. Am.*, 78, pp. 1563-1579.
- Taylor, S. R. and G. E. Randall (1989), The effects of spall on regional seismograms, *Geophys. Res. Lett.*, 16, pp. 211-214.
- Taylor, S. R. and M. D. Denny (1991), An analysis of spectral differences between Nevada Test Site and Shagan River nuclear explosions, *J. Geophys. Res.*, 96, pp. 6237-6245.
- Taylor, S. (1996), Analysis of high-frequency Pg/Lg ratios from NTS explosions and Western U.S. earthquakes, *Bull. Seism. Soc. Am.*, 86, pp. 1042-1053.
- Taylor, S., A. Velasco, H. Hartse, W. S. Philips, W. R. Walter, and A. Rodgers (2002), Amplitude corrections for regional discrimination, *Pure. App. Geophys.*, 159, pp. 623-650.
- Tibuleac, I. M., J. L. Bonner, E. T. Herrin, and D. G. Harkrider (2002), Calibration of the Ms:mb discriminant at NVAR, 24th Seismic Research Review – Nuclear Explosion Monitoring: Innovation and Integration, Ponte Vedra Beach, FL.
- Tibuleac, I. M., D. H. von Seggern, J. G. Anderson, and J. N. Louie (2011), Computing Green's Functions from Ambient Noise Recorded by Narrow-Band Seismometers, Accelerometers, and Analog Seismometers, doi: 10.1785/gssrl.82.5.661 *Seismological Research Letters*, Vol. 82, no. 5, pp. 661-675.
- Tsai, N. C. (1969), Influence of local geology on earthquake ground motion, California Institute of Technology, Pasadena, <http://resolver.caltech.edu/CaltechEERL:1969.EERL.1969.002>.
- Uchide, T., H. Yao, and P.M. Shearer (2013), Spatio-temporal distribution of fault slip and high-frequency radiation of the 2010 El Mayor-Cucapah, Mexico earthquake, *J. Geophys. Res. Solid Earth*, 118, pp. 1546-1555, doi:10.1002/jgrb.50144.
- Vaněk, J., A. Zatopek, V. Karnik, N. V. Kondorskaya, Yu. V. Riznichenko, E. F. Savarensky, S. L. Solovyov, and N. V. Shebalin (1962), Standardization of magnitude scales, *Bull. (Izvest.) Acad. Sci. USSR, Geophys., Series 2*, p. 108
- von Seggern, D. (1977), Amplitude-distance relation for 20-second Rayleigh waves, *Bull. Seism. Soc. Amer.*, Vol. 67, pp. 405-411.
- von Seggern, D. H., J. G. Anderson, I. M. Tibuleac, and G. P. Biasi (2014), Double-difference location and GT classification of the 2008 Mogul, Nevada, very shallow earthquake sequence (submitted for publication to *Seismological Research Letters*).
- Waldhauser, F. and W. L. Ellsworth (2000), A double-difference earthquake location algorithm: Method and application to the northern Hayward fault, California, *Bull. Seismol. Soc. Am.*, 90, pp. 1353-1368.
- Walter, W. R., K. Mayeda, and H. J. Patton (1995), Phase and spectral ratio discrimination between NTS earthquakes and explosions Part 1: Empirical observations, in press, *Bull. Seism. Soc. Am.*, 85, pp. 1050-1067.
- Walter, W. R. and S. R. Taylor (2001), A revised magnitude and distance amplitude correction (MDAC2) procedure for regional seismic discriminants: theory and testing at NTS, LLNL UCRL - ID - 146882, <http://www.llnl.gov/tid/lof/documents/pdf/240563.pdf>.
- Walter W. R., K. D. Smith, J. L. O'boyle, T. F. Hauk, F. Ryall, S. D. Ruppert, S. C. Myers, R. Abbot, D. A. Dodge (2004), An assembled western United States dataset for regional seismic analysis. Lawrence Livermore National Laboratory Technical Report, UCRL-TR-206630.

- Xie, J. K., Z. Y. Liu, R. B. Herrmann, and E. Cranswick (1991), Source Processes Of 3 Aftershocks Of The 1983 Goodnow, New-York, Earthquake - High-Resolution Images Of Small, Symmetrical Ruptures, *Bulletin of the Seismological Society of America*, 81(3), pp. 818-843.
- Xie, J. and H. J. Patton (1999), Regional phase excitation and propagation in the Lop Nor region of central Asia and implications for P/Lg discriminants, *J. Geophys. Res.*, 104, pp. 941-954.
- Yoo, S-H and K. Mayeda (2013), Validation of Non-Self-Similar Source Scaling Using Ground Motions from the 2008 Wells Earthquake Sequence, *Bulletin of the Seismological Society of America*, Vol. 103, No. 4, pp. 2508-2519, doi: 10.1785/0120120327.
- Zaslavsky-Paltiel, I and D. M. Steinberg (2008), Comparison of Methods for Estimating Station Magnitude Corrections for Improved Seismologic Monitoring of the Comprehensive Nuclear-Test-Ban Treaty, *Bulletin of the Seismological Society of America*, 98(1), pp. 1-17, doi: 10.1785/0120070019.
- Zeiler, C. and A. A. Velasco (2009), Developing Local to Near-Regional Explosion and Earthquake Discriminants, *Bulletin of the Seismological Society of America*, 99(1), pp. 24-35, doi: 10.1785/0120080045.
- Zhang, T., S. Y. Schwartz, and T. Lay (1994), Multivariate analysis of waveguide effects on short period regional wave propagation in Eurasia and its application in seismic discrimination, *J. Geophys. Res.*, 99, pp. 21929-21945.

List of Symbols, Abbreviations, and Acronyms

AFRL	Air Force Research Laboratory
AFSPC	Air Force Space Command
AFWA	Air Force Weather Agency

DISTRIBUTION LIST

DTIC/OCF	
8725 John J. Kingman Rd, Suite 0944	
Ft Belvoir, VA 22060-6218	1 cy
AFRL/RVIL	
Kirtland AFB, NM 87117-5776	2 cys
Official Record Copy	
AFRL/RVBYE/Robert Raistrick	1 cy

This page is intentionally left blank.